ASA Final Report
NWC/GEO-HRW
STEREO AMV Integration

26 November 2025

Team:

AEMET/NWC SAF (Sponsor):
Javier García Pereda

University of Maryland (Home Institute) and Hampton University:
Mariel Friberg, Principal Investigator

Carr Astronautics:
Jim Carr, Lead Scientist
Xuming Lei, Software Lead
Houria Madani, Senior Scientist
Solomon Jackson, AWS System Administrator

1 Purpose 3
2 Background 4
3 Methods 5
3.1 Overview of Workflow 5
3.2 Integration of Stereo Functionality into NWC/GEO-HRW vMTG 7
3.2.1 Remapping of ABI Images into FCI Geometry 9
3.2.2 LUT Driven ABI Pixel Times 10
3.2.3 Stereo Parallax and Height Assignment 12
3.3 Validation of Stereo-Derived AMV Heights and Pressures (NASA-Sponsored Component) 14
3.3.1 Full Validation Across All Applicable Conditions 14
3.3.2 Determination of Operational Limits 14
3.3.3 Comparison with Existing Height Assignment Techniques 15
3.3.4 Quality-Control Consistency Analysis 15
3.4 Coordination and Data Support 15
3.5 Software Development Approach 15
4 Results 16
4.1 Comparison of Stereo and Non-Stereo Winds: EarthCARE 16
4.2 Comparison of Stereo and Non-Stereo Winds: ERA5 24
5 Conclusions 26
5.1 EarthCARE 26
5.2 ERA5 26
5.3 Summary 26
6 Implementation within SAF Products 27
6.1 Software and Documentation 27
6.2 Additional Software package 28
7 References 29
8 Appendices 31
Appendix A – Stereo Winds Retrieval Mathematical Algorithm Description (ATBD Chapter) 31
Appendix B – EarthCARE Curtain Plots 39
Appendix C – ERA5 Observations versus Analysis 68
C.1 Results for Low Level Winds (height < 2km) 70
C.2 Results for Mid Level Winds (height 2-6km) 74
C.3 Results for High Level Winds (height > 6km) 78

1 PURPOSE

The purpose of this Associated Scientist Activity (ASA) was to integrate and evaluate all required code extensions for the stereo height assignment method within the NWC/GEO-HRW vMTG framework [RD.1]. This work focused on supporting day-1 vMTG capabilities and preparing the method for inclusion in a subsequent NWC/GEO-HRW release. The stereo height assignment approach was implemented for Atmospheric Motion Vectors (AMVs) located within the region jointly observed by MTG-I1 and GOES-East in **Figure 1,** with clearly defined conditions under which the method can be optimally applied. The code was developed with documentation to facilitate future extensions to additional geostationary satellite pairs. Importantly, stereo height assignments can support future studies to improve existing non-stereo height assignment methods.

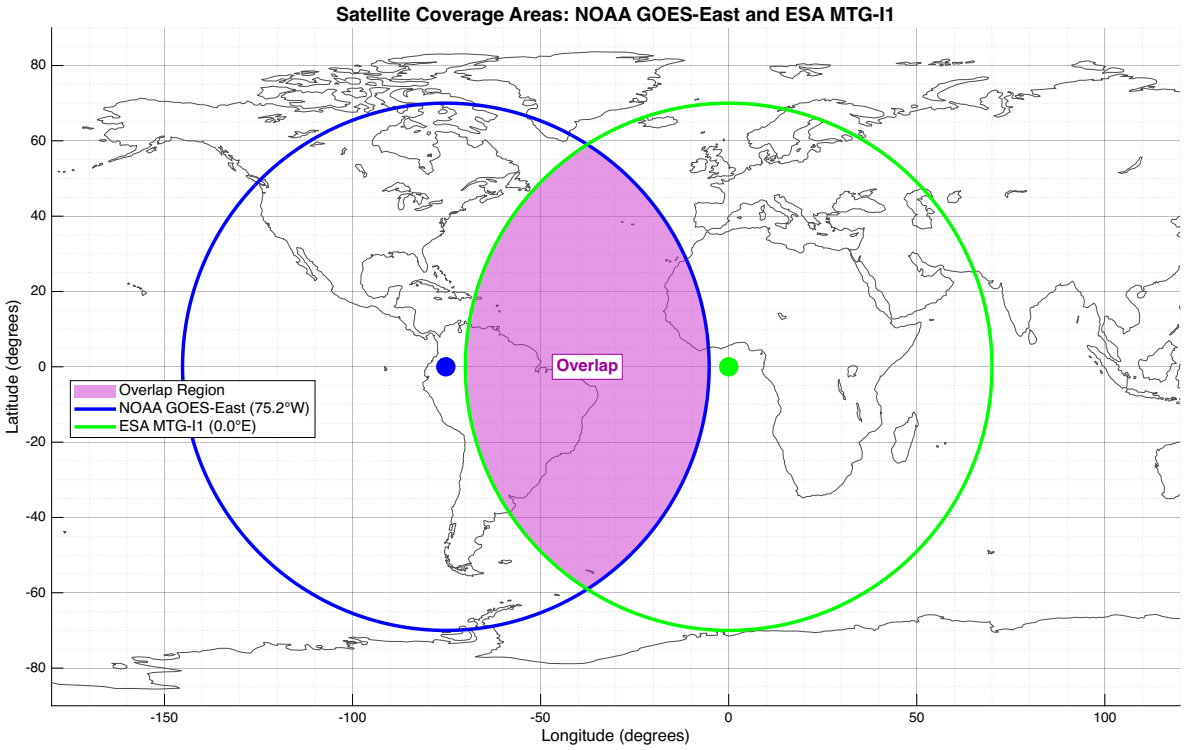


Figure 1. *Satellite Domain overlap*

All algorithmic additions were thoroughly tested and validated to ensure that the AMV height and pressure values derived from the stereo height assignment method are accurate under all circumstances in which the method is applicable. These values were systematically compared with the existing NWC/GEO-HRW height-assignment outputs to identify the situations in which each approach performs best.

The stereo height assignment method has gained traction within the AMV community due to its geometric foundations and reduced dependence on ancillary datasets relative to traditional height-assignment techniques. Improvements in spatial resolution from modern geostationary satellites have further enhanced its performance and facilitated its operational uptake, such as in NOAA's AMV processing for GOES-R where stereo capabilities are

under development. Similar benefits were anticipated and demonstrated for inclusion in the NWC/GEO-HRW system. With the initial implementation completed for the MTG-I1 and GOES-East satellite pair, the method can now be readily adapted for additional geostationary combinations in future NWC/GEO releases and is available for studies to improve height assignments in general.

2 BACKGROUND

One of the core mandates of the NWC SAF is to provide the highest-quality satellite-derived products to support nowcasting applications. Within this framework, the NWC/GEO-HRW product generates AMVs and Trajectories by tracking the displacement of cloud or moisture tracers across consecutive images from geostationary satellites. A longstanding challenge in global AMV production is the accurate *height assignment* of these tracers, that is, determining their vertical location within the atmosphere in pressure coordinates. Errors in height assignment remain one of the dominant sources of uncertainty in AMV datasets worldwide [RD.2].

Historically, NWC/GEO-HRW has relied on two primary height-assignment approaches [RD.3]:

1. **Brightness Temperature Interpolation**, used in the earliest versions of the algorithm; and
2. **The Cross-Correlation Contribution (CCC) method**, the default since 2011 and further refined in 2016 using cloud-microphysical parameters to adjust pressure levels.

These techniques are well documented in the Algorithm Theoretical Basis Document (ATBD) for the NWC/GEO wind product processor [RD.3]. While effective, both approaches require substantial processing and depend heavily on inputs from several NWC/GEO cloud products (e.g., CT, CTTH, CMIC), as well as numerous NWP forecast fields. These dependencies increase computational complexity and can propagate uncertainties from upstream products into the AMV height assignment.

In contrast, the stereo height assignment method, illustrated conceptually in **Figure 2** and based solely on the geometric parallax of a tracer observed from two geostationary satellites, offers a streamlined and computationally simpler alternative. First discussed as early as the Second International Winds Workshop in 1993 [RD.4], the approach exploits the difference in apparent tracer location when viewed from different satellite angles, which is directly related to the tracer's height above Earth's surface. Despite its conceptual simplicity, early applications of the stereo method were limited by several constraints: simultaneous observations were required from two satellites with sufficiently large viewing-angle separation, and any asynchrony between the two scenes needed correction. In addition, Image Navigation and Registration (INR), which is the process of navigating pixels to Earth locations, was not sufficiently accurate in early generations of weather satellites. These limitations prevented widespread adoption in operational AMV algorithms.

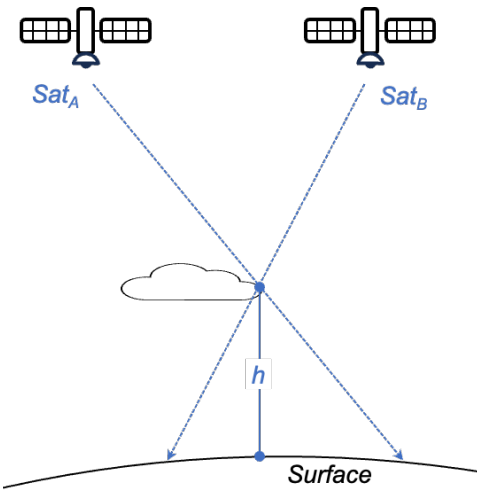


Figure 2. *Displacement (difference in the apparent position) over the Earth surface of a tracer/AMV observed with different angles by two different satellites.*

The emergence of the latest generation of geostationary satellites (including Himawari-8/9, GOES-R, GEO-KOMPSAT-2A, and MTG-I) has addressed many of these earlier challenges. These platforms offer improved spatial resolution, high-accuracy geometric registration, and the ability to time-tag pixels precisely. As highlighted by Carr et al. at the Sixteenth International Winds Workshop [RD.5], these improvements are driving renewed interest in operational stereo-based AMV height determination. NASA–NOAA collaborations since 2018 have demonstrated that the geometric accuracy of modern satellites enables robust stereo solutions for AMV height retrievals [RD.6]. Importantly, time-tagging capabilities now allow the use of *non-simultaneous* image pairs, further extending the method's applicability [RD.7, RD.8, RD.9]. NOAA is already developing a pre-operational stereo height-assignment product using GOES-R and Himawari-8/9.

Within this evolving context, the NWC SAF is preparing to expand the NWC/GEO-HRW algorithm to incorporate stereo-based height assignment for AMVs observed jointly by MTG-I1 and GOES-East. This capability is planned to be included in the next release of NWC/GEO-HRW (v2027). To support this effort, this report describes the development and integration of the required code extensions, the evaluation of conditions under which the stereo method performs best, and the comparison of stereo-derived heights with those produced by existing NWC/GEO-HRW methods. The overarching aim was to ensure that the resulting stereo solution is robust, fully validated, and could be readily adaptable to additional geostationary satellite pairings in future algorithm versions.

3 METHODS

3.1 OVERVIEW OF WORKFLOW

The methodological workflow for this study involved integrating the GEO–GEO stereo height-assignment capability into the NWC/GEO-HRW vMTG day-1 algorithm, validating the resulting stereo-derived AMV heights and pressures, and assessing their operational limits and performance relative to existing height-assignment techniques. All development

was conducted in close coordination with the NWC SAF Project Team and aligned with complementary NASA-supported validation activities. The implementation supports multiple-image stereo configurations, including two-, four-, and six-image combinations of MTG-I1/FCI FDHSI and GOES-East/ABI Full Disk imagery.

The GEO–GEO stereo-wind methodology relies on using two to three temporally separated repetitions from the reference satellite, Sat_A, and one to three repetitions from the secondary satellite, Sat_B, with the constraint that all repetitions within each satellite originate from the same scene type and channel/band pairing. In this study, MTG-I1 (FCI) serves as Sat_A and provides the native fixed grid and reference template, while GOES-East (ABI) serves as Sat_B and is fully remapped to the MTG-I1 grid. This reprojection step yields a region on the western edge of the MTG-I1 disk where corresponding GOES-East pixels exist within the GOES-East horizon. **Figure 3** illustrates the temporal pairing strategy used for the stereo retrievals, showing the use of MTG-I1 images at times t, t–Δt, and t–2Δt in combination with one or more temporally aligned GOES-East images. **Table 1** summarizes the specific MTG-I1/FCI and GOES-East/ABI channel and band correspondences used in the stereo processing. The overall approach follows the framework described in Carr et al. (2020), adapted here for the MTG-I1 and GOES-East pairing.

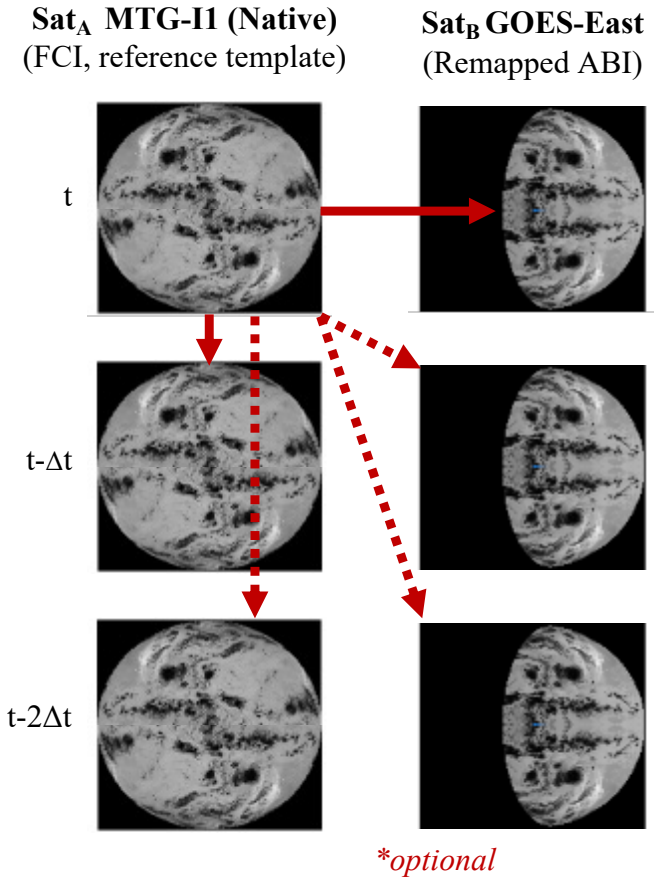


Figure 3. *Satellite A and B pairings.*

Table 1. *MTG-I1 to GOES-East Pairings*

MTG-I1 FCI λ_0 Resolution	VIS 0.6 0.64 µm 1 km (0.5 HR)	WV 6.3 6.3 µm 2 km	WV 7.3 7.35 µm 2 km	IR 10.5 10.5 µm 2 km (1 km HR)
GOES-East ABI λ_0 Resolution	Band 2 0.64 µm 0.5 km	Band 8 6.2 µm 2 km	Band 10 7.35 µm 2 km	Band 13 10.5 µm 2 km

3.2 Integration of Stereo Functionality into NWC/GEO-HRW vMTG

Figure 4 illustrates how the stereo height-assignment capability is integrated into the NWC/GEO-HRW processing chain. After the MTG-I1 reference scenes and the remapped GOES-East scenes are ingested, the HRW system initiates the stereo-wind module, which performs image registration to remap all scenes to the MTG-I1 fixed grid and extracts the corresponding tracers. These tracers are matched across the Sat_A and Sat_B image sequences, and AMV times are assigned based on the temporal pairing configuration shown earlier. The stereo module then computes the 3-D wind solution—deriving stereo heights, pressures, and displacement vectors—followed by internal quality control screening applied within the HRW framework. Once stereo processing is complete, the algorithm returns to the main HRW workflow, where AMVs are compiled across all processed channels, trajectory information is calculated, and both basic and detailed output files are written. The diagram highlights the modular insertion of the stereo method within the existing HRW architecture, ensuring compatibility with the operational HRW processing steps downstream.

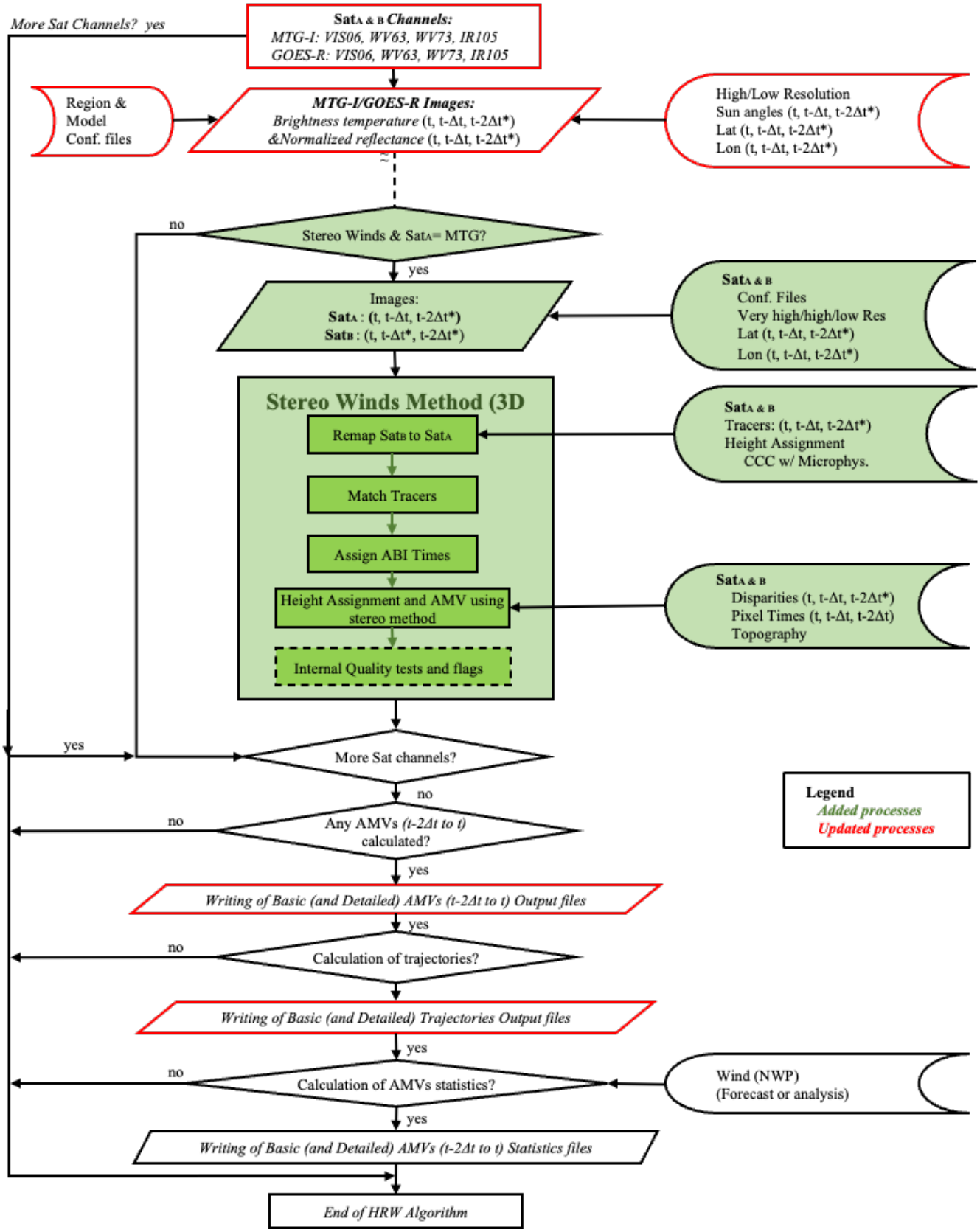


Figure 4. *Stereo implementation into NWC/GEO-HRW.*

3.2.1 Remapping of ABI Images into FCI Geometry

To enable stereo height retrievals, the GOES-East imagery used as the secondary satellite input are reprojected into the native MTG-I1 viewing geometry using Look-Up Tables (LUTs) (**Figure 5**). LUTs are calculated once and saved in netCDF files. Remapping LUTs are applied to the ABI images to remap them into the FCI fixed grid (**Figure 6**). The process looks up a floating-point row and column address at each FCI pixel location and interpolates the value for that location from a neighborhood of the site addressed in the ABI image. Bilinear interpolation is used. This was implemented within the HRW vMTG day-1 C codebase to ensure that the resulting MTG-aligned GOES-East imagery could be used seamlessly for tracer extraction and parallax-based stereo height estimation as if native FCI imagery.

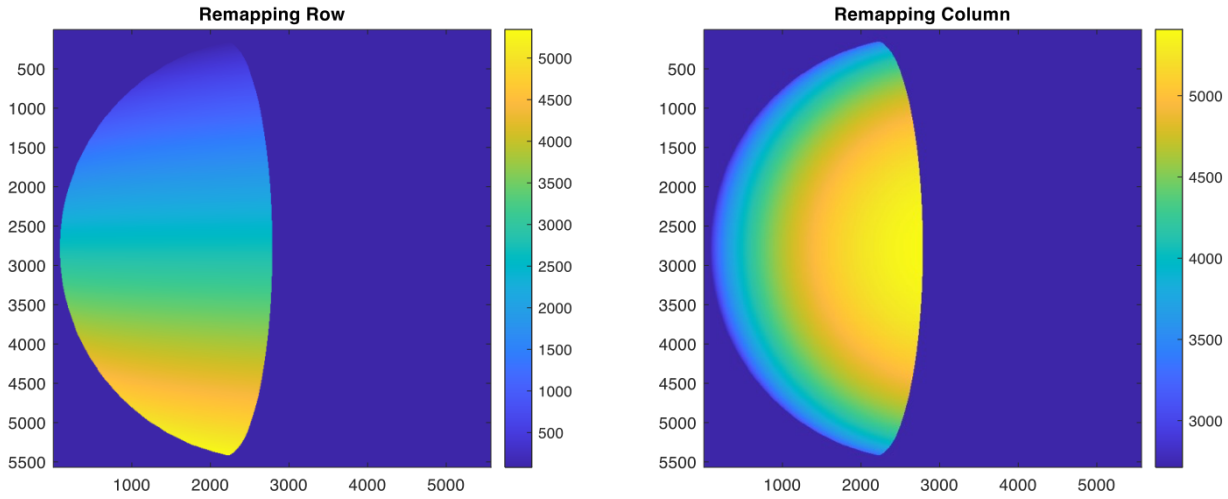


Figure 5. *GOES ABI row and column Look-Up Tables used to remap to MTG-I1 FCI.*

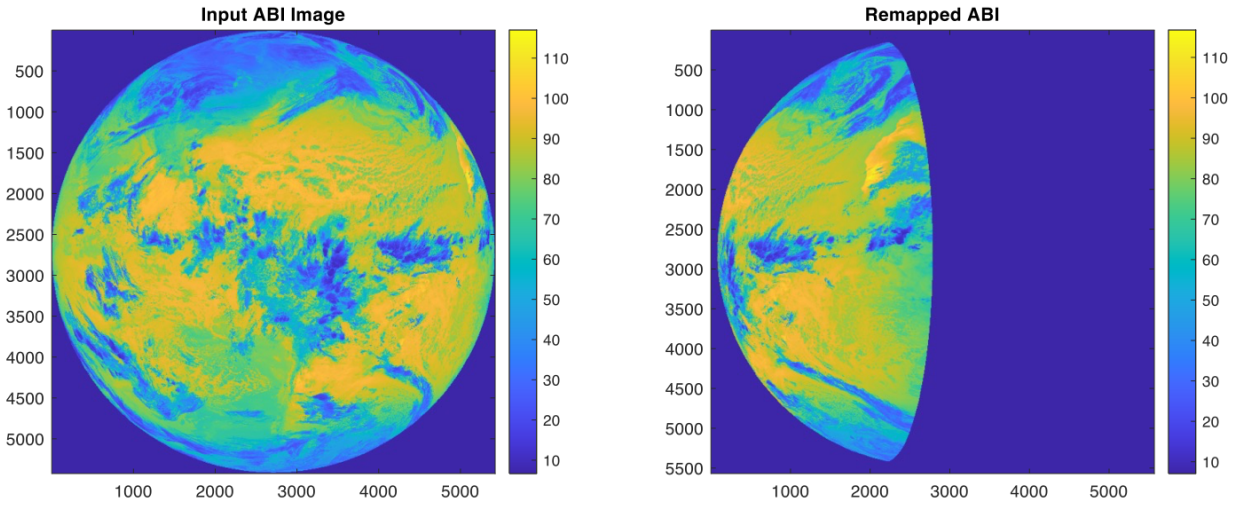


Figure 6. *Remapping Look-Up Tables applied to GOES ABI imagery.*

Satellite position vectors are needed to interpret the parallax. Both satellites are maintained close to their nominal longitudes, which makes using exact position vectors less important. Although dynamic position information could, in principle, improve geometric consistency—especially for satellites experiencing small but non-negligible longitudinal drift—the current NWC SAF/VSA framework and the ABI product files are not well adapted for this approach. Instead, satellite positions are specified as configuration variables. This capability could be revisited in future versions if user requirements or upstream mission specifications evolve to necessitate fully dynamic orbit handling.

3.2.2 LUT Driven ABI Pixel Times

The handling of FCI pixel acquisition times was revised to use channel-specific data obtained from the FCI satellite images, replacing the earlier approximation in HRW that applied a single Δt value (e.g., the IR 3.8 µm timing) across all channels. This per-channel implementation accounts for the small but meaningful timing differences inherent to FCI's scanning strategy.

After updating the MTG-I1 pixel timing within the HRW system, some adjustments were needed to align the LUT-based ABI pixel times to the FCI slot times, resulting in proper time alignment of ABI and FCI pixels. This LUT-based strategy for ABI provides a more accurate and operationally robust representation of ABI pixel acquisition times for stereo processing. The time model for ABI pixels is shown in **Figure 7** below.

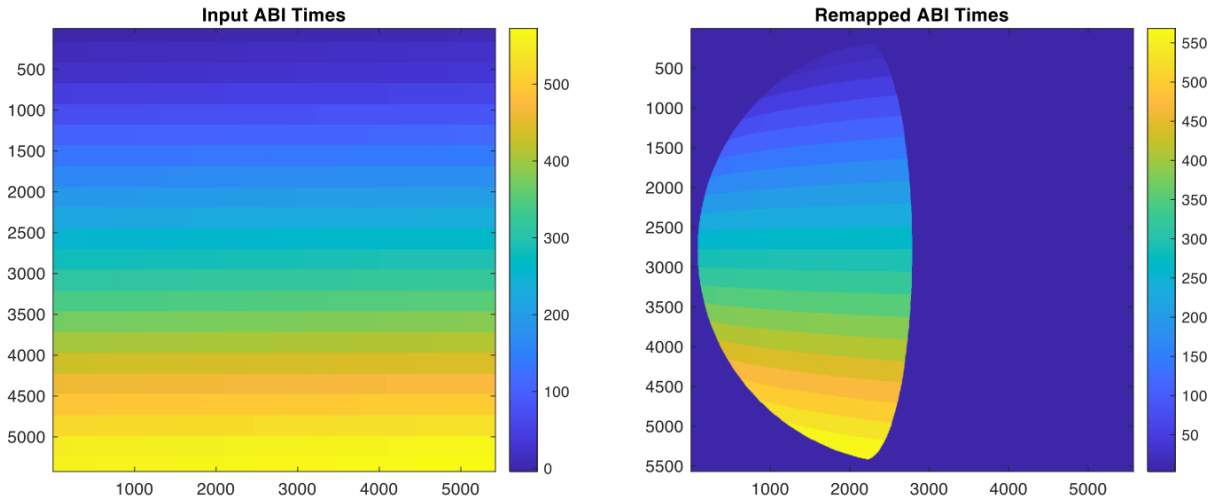


Figure 7. *Input and Remapped Time Look-Up Tables for GOES ABI in unit seconds.*

With ABI, times are given relative to the first B02 pixel in a scene. The first B02 pixel sampling time is encoded in the NetCDF file name as the start time after "s". We call this the 'product time'. The schema for the product time is yyyydddhhmmsss, where ddd is the day of year and sss is the seconds plus tenths of a second. More conventionally, we would write yyyy/ddd hh:mm:ss.s.

The first pixels of the LUT are fictitious as ABI overscans the Earth only enough to capture the disk with all channels and the ground processing fills the rest to make a rectangular

product. The ground processing also fills the near limb and space pixels with fill values to mask them out in the product. **Figure 8** shows where the sampling begins for the first swath, which is the origin for the time offset to add to the product time. The time LUT values increase uniformly in accordance with the scan rate from left to right.

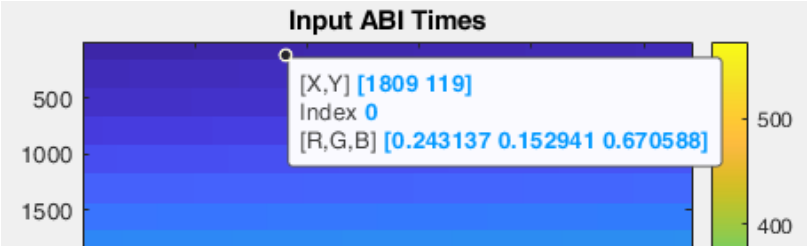


Figure 8. *Start of time in the Time Look-Up Table.*

The GOES-R website (www.goes-r.gov) shows a Mode 6 timeline, shown in **Figure 9** with the Full Disk (FD) product start and end times noted. The FD swaths are salmon colored in the timeline diagram. The start-to-end duration of the FD is about 9:30. The times for each product swath are figured from the timeline shown. The drawing of the swath transitions and small adjustments to the sampling times of other bands relative to that of B02 is described in https://www.mdpi.com/2072-4292/12/22/3779.

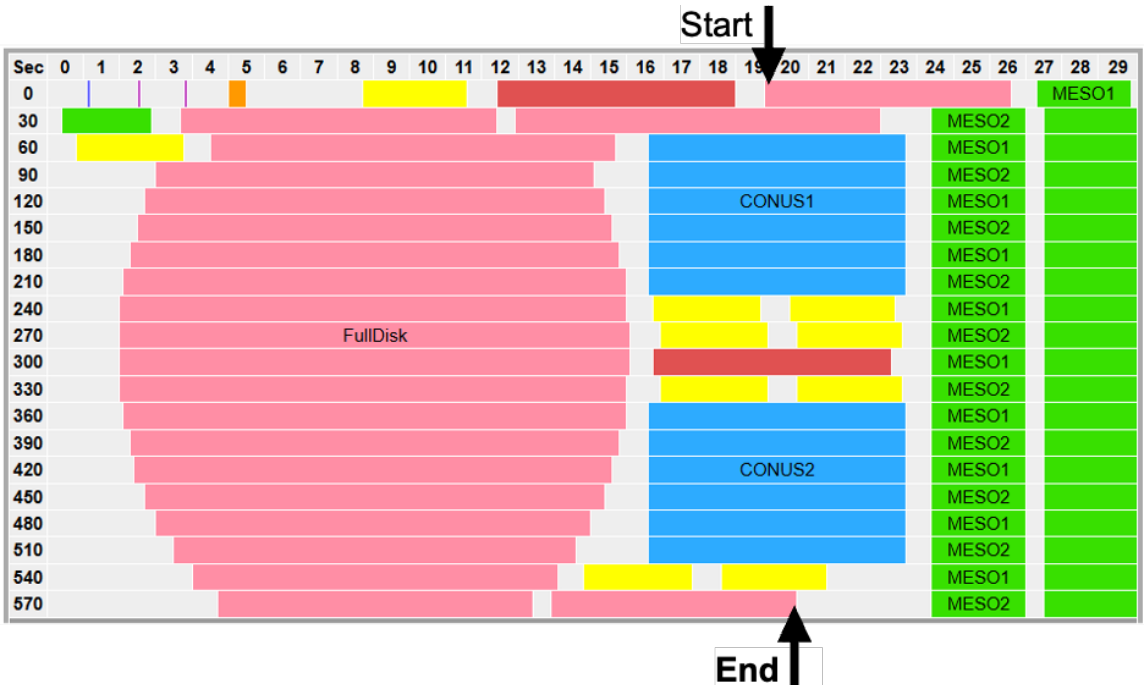


Figure 9. *GOES ABI Mode 6 Timeline*

The time LUT can be used directly to time-tag ABI pixels in the native ABI geometry. For HRW, the LUT has been remapped using similar functions to those used to remap the imagery. We see this in the right panel of **Figure 7**.

3.2.3 Stereo Parallax and Height Assignment

Initial guesses for wind vectors and their heights were made from the NWP to enable more efficient searching for matches. Other than seeding the search, the NWP does not enter into the stereo wind retrieval. LUTs are provided to translate a km of altitude into a parallax (**Figure 10**). After matching, parallax measurements were then converted into geometric heights using the satellite ephemerides and full viewing-geometry information for both platforms, after which equivalent pressure levels were obtained through standard HRW thermodynamic conversion routines. The resulting quantities, "AMV stereo height" and "AMV stereo pressure," were integrated directly into the HRW output structure alongside existing single-view height assignments. All newly developed modules were validated for numerical consistency, error-handling robustness, and full compatibility with the operational HRW processing chain.

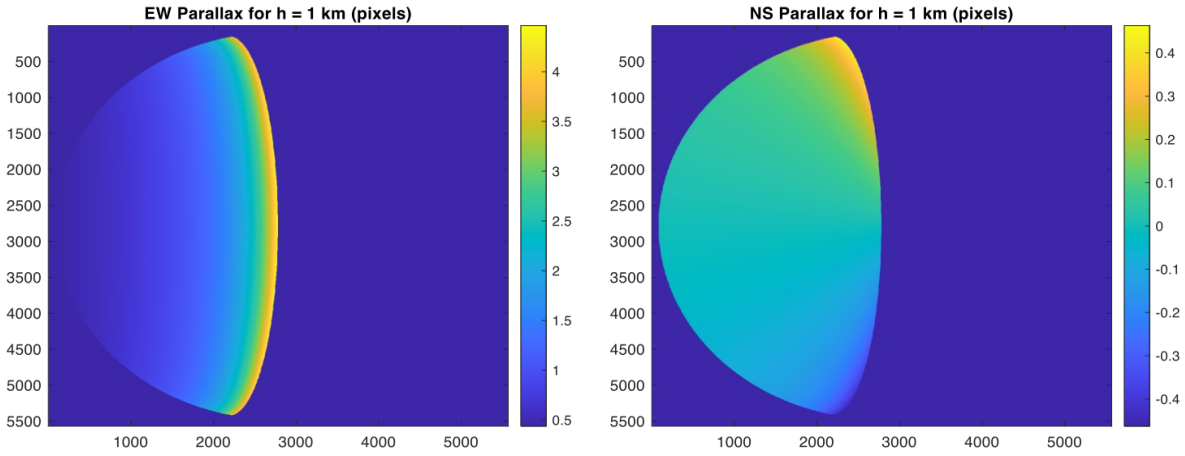


Figure 10. East-West and North-South Parallax Look-Up Tables.

3.2.3.1 Stereo-Wind retrievals

The stereo-wind retrieval itself is formulated as an optimization problem that uses the apparent positions of a tracer observed at multiple times by Sat_A and Sat_B. Using a reference scene from Sat_A at time, *t*, and additional scenes from both Sat_A and Sat_B at t and adjacent *t* as shown in **Figure 3**, the algorithm solves for tracer height and horizontal motion by minimizing weighted residuals between modeled and observed parallax-induced displacements. Two models are supported: a three-parameter (order-3) version solving only for height and wind, and a five-parameter (order-5) version that adds adjustments for potential image-navigation errors. The problem is solved iteratively using linearized updates, with convergence assessed via position and velocity tolerances.

Overdetermination, using more scenes (i.e., $t+\Delta t$, $t+2\Delta t$) than the minimum required, improves robustness but must be balanced against the assumption that tracers translate without evolving. The five-parameter model is generally preferred because it absorbs systematic navigation biases and yields noise-like residuals, which are essential for quality control.

Appendix A provides a full mathematical description.

3.2.3.2 Final Control Check and Output data filtering

The final stage of the stereo workflow applies a consolidated control check and output-filtering procedure to ensure that the retrieved winds, heights, and parallax values are geometrically consistent and scientifically robust. Unlike the traditional CCC method used in the single-view HRW chain, which emphasizes the most visually striking feature within a scene, the stereo implementation defines the height of patterns at the centers of the tracked cloud features explicitly. This enables direct comparison of disparities between the two satellites in terms of paired latitude–longitude displacements. These disparities feed into the stereo height solution, which now incorporates geoid-referenced height information for computing pressure more accurately (**Figure 11**).

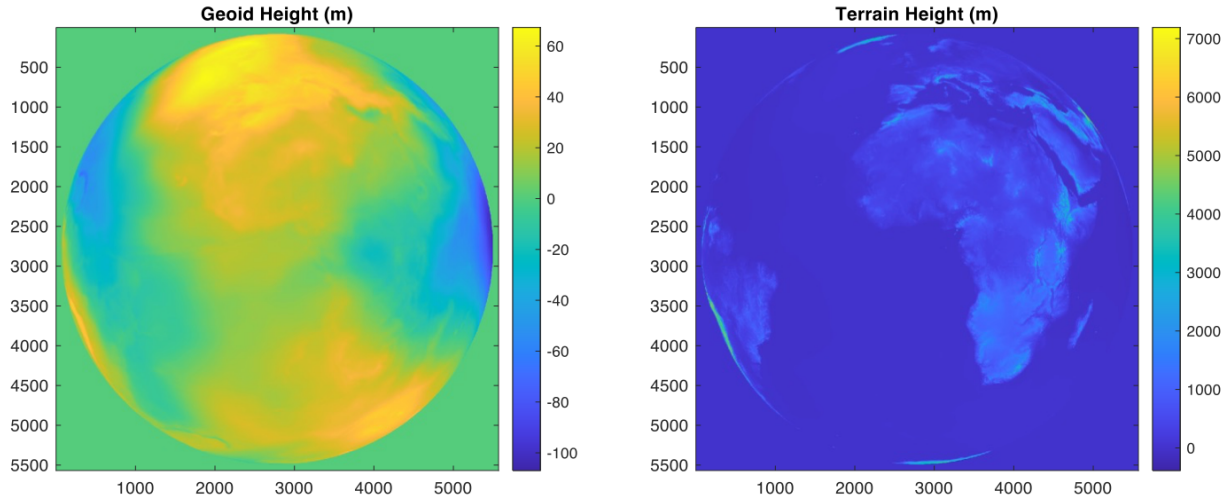


Figure 11. *Geoid and Terrain Height Look-Up Tables*

To capture the quality of the stereo fit, the system produces residual metrics derived from the difference between measured and modeled disparities. The residual sum of squares are retained in the output. The covariance matrices, either 3×3 or 5×5 depending on whether an order-3 (height, u, v) or order-5 (dx, dy, height, u, v) solution is used, are stored separately. Error bars are represented as the square roots of the diagonal elements of these covariance matrices and are written to the output files to provide pixel-level uncertainty estimates. Retrievals are also tested against terrain height to identify below ground or below water unphysical cases.

Additional refinements exist in NWC/GEO-HRW algorithm to improve computational efficiency and retrieval fidelity. The tracking-window dimensions are dynamically determined based on the estimated displacement and the true inter-image time difference Δt, replacing the former static ~70×70 window with adaptive sizes typically near 42×42 pixels. This adjustment significantly reduces computation time and stabilizes the stereo solution across varied motion regimes. Moreover, applying an internal filter of RMS residuals < 0.25 × resolution within the HRW chain, prior to the standard Quality Control sequence, was found to yield slightly improved performance compared to applying the same criterion as a post-processing filter.

Finally, new parallax diagnostics, including row and column parallax matrices, are being added to the HRW suite. These fields provide an explicit, gridded representation of the along-row and along-column stereo parallax contributions and offer additional transparency into the underlying geometric constraints that drive the stereo height solution.

3.3 Validation of Stereo-Derived AMV Heights and Pressures (NASA-Sponsored Component)

3.3.1 Full Validation Across All Applicable Conditions

A comprehensive validation effort was undertaken to assess the accuracy, robustness, and physical consistency of the stereo-derived AMV heights and pressures across all conditions in which the method can be applied. This evaluation spanned a wide range of cloud types, atmospheric regimes, and diurnal periods to ensure that the stereo solution remained stable under diverse environmental settings. Attention was given to the treatment of parallax uncertainties and the application of time-asynchrony corrections across the MTG-I1 and GOES-East image sequences, both of which are essential for maintaining coherent stereo geometry. Across all tests, the resulting height and pressure fields were examined for physical plausibility, internal consistency, and expected behavior as a function of scene characteristics.

3.3.2 Determination of Operational Limits

The validation also quantified the operational limits of the stereo method to determine the conditions under which the technique performs most reliably. Sensitivity analyses were conducted to characterize the influence of the satellite separation angle, the dependence on satellite zenith angle, and the geometric circumstances that either enhance or diminish the effective height sensitivity. These factors collectively define the regions in which stereo winds can be expected to provide the most benefit. The stereo-capable domain (ALLSTEREO) was defined as the MTG-I1 and GOES-East overlapping area, extended outward by approximately fifty pixels beyond the GOES-East remapping boundary to avoid edge effects.

Our development and testing environment was on AWS where we used 32 cores, 128GB of memory, and 6TB of storage. The performance assessment included computational considerations relevant to day-1 operations, considering the defined working system. For example, the NWP mapping with AllMappingNWP ran four times per day, adding approximately eight minutes of total daily cost, while the associated slot pre-processing (MTG-I SDI format input files preparation and GEO-CMA/CT/CTTH/CMIC processing) typically required around six minutes per slot. HRW runtimes for the NONSTEREO configuration remained near 15 minutes and 51 seconds, whereas the stereo configuration—using three to six images and either the order-3 or order-5 solution—required between 13 and 17 minutes per slot, with comparable or improved NRMSVD statistics. For validation purposes, the order-5 solution was preferred because it provides a richer representation of the tracer motion. Tests also showed that clear-air AMVs degrade the statistical performance (e.g., WV clear-air NRMSVD ≈ 0.54), and thus setting CLEARAIRWINDS=0 is advisable during validation exercises focused on cloud-based tracers.

These results collectively define the geometric, physical, and computational limits of applicability and provide guidance for future operational use of the stereo method.

3.3.3 Comparison with Existing Height Assignment Techniques

The stereo-derived AMV heights and pressures were compared directly with those produced by the existing CCC height-assignment method within NWC/GEO-HRW. Conditions were identified in which the stereo solution clearly outperforms CCC and conditions where CCC appeared to be more reliable. The resulting analysis also explored the implications for downstream AMV quality metrics and for tropospheric wind-vector characterization, providing insight into how stereo information can complement and potentially enhance the standard HRW height-assignment strategy.

3.3.4 Quality-Control Consistency Analysis

To ensure smooth integration into the operational HRW pipeline, all stereo-derived AMVs were processed using the same quality-control framework applied to standard AMVs. This assessment examined the degree of alignment between stereo-enabled and standard Quality Control (QC) outcomes and identified any thresholds or filter settings that might require adjustment. The influence of stereo-derived heights on AMV scoring, consistency checks, and the overall filtering behavior was also analyzed. The resulting recommendations provide guidance on QC tuning to support day-1 operational use of stereo heights within NWC/GEO-HRW.

3.4 Coordination and Data Support

The NWC SAF Project Team supplied the necessary satellite observations, NWP fields, and auxiliary datasets for algorithm development, while NASA provided scientific oversight and resources for= the validation component under the direction of Dr. Dong L. Wu (NASA/GSFC). HRW results were also cross-checked with a parallel implementation in NASA research code. Although these activities proceeded on separate tracks, both remained closely coordinated to ensure scientific consistency and to support the broader objective of introducing stereo height-assignment capability into NWC/GEO-HRW. Importantly, the integration of stereo functionality into the HRW codebase was carried out independently of the NASA-funded work, ensuring that the method would be delivered to NWC SAF irrespective of external support while still benefiting from aligned scientific collaboration.

3.5 Software Development Approach

The stereo-related software components were developed primarily in C to maintain consistency with the existing NWC/GEO-HRW architecture and to facilitate seamless integration into the operational codebase. All source files were delivered without restriction on modification or redistribution and are intended for incorporation into future HRW releases. Emphasis was placed on modular design and robust inline documentation to support long-term maintainability and provide a foundation for extending stereo capability to additional geostationary satellite pairs beyond the MTG-I1/GOES-East configuration addressed in this work.

4 RESULTS

The stereo height-assignment implementation was evaluated across seven representative dates spanning January–March 2025, selected to capture a range of cloud regimes and synoptic environments. The validation relied on the ERA5 forecast model, whose reanalysis-quality background fields provide a consistent, high-resolution reference for assessing AMV height and wind accuracy. The 2025 test dates included: January 3, 17, and 31; February 14 and 28; and March 14 and 28. These cases collectively sample mid-winter through early spring conditions in the MTG-I1 and GOES-East joint domain and encompass variability in cloud depth, wind shear, and viewing geometry that is essential for a robust evaluation of the stereo method.

4.1 COMPARISON OF STEREO AND NON-STEREO WINDS: EARTHCARE

Here we directly compare stereo and non-stereo winds with a particular interest in the height assignments because the main interest in the stereo implementation is to use it to validate and improve height assignments in HRW. To illustrate, we pick a date and slot (28 March 2025 15:30Z) where there is also an EarthCARE satellite pass that is nearly simultaneous with the HRW winds. The scope of the coverage with stereo is seen in **Figure 12.** Stereo retrievals only exist in the overlapping coverage of FCI and ABI on the GOES-East satellite. They are nominally stationed at 0° and -75.2° longitudes respectively. Also shown are the stereo sites where the Earth Central Angle (ECA) is less than 60° for both satellites. This can be considered the prime area for stereo, although many of the retrievals beyond 60° ECA are perfectly good. We define ECA as the arc-distance on the surface of a spherical Earth between the subsatellite point and the site.

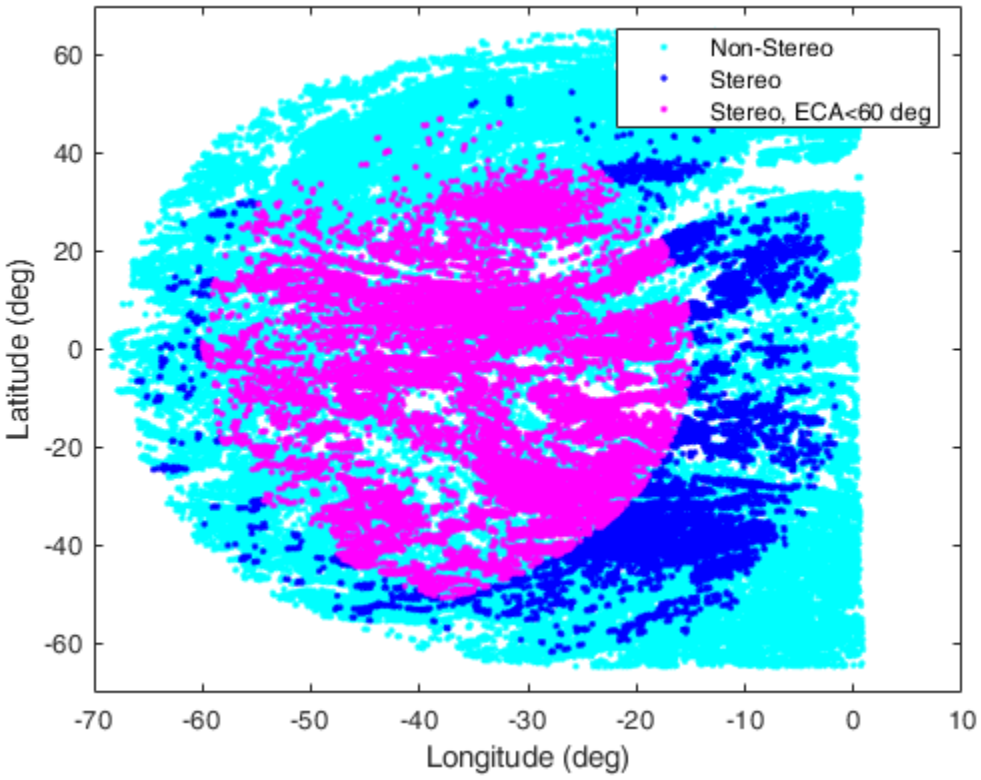


Figure 12. *Scope of Coverage for Stereo and Non-Stereo Winds. Not shown are non-stereo winds on the eastern side. Magenta points are the prime sites for stereo winds.*

We consider the height assignments in both cases, limiting the scope to ECA<60° for both satellites. Nominal quality filters are applied in both cases. Several remarks can be made. First, the density of non-stereo winds is much higher than the stereo winds. This may be because more successful matches (*i.e.*, those with adequate correlation coefficients) are needed for stereo retrievals. Second, the two height assignments tend to put the tracked cloud features in common layers but there seems to be a phenomenon of the non-stereo heights continuously declining at layer edges. Third, many non-stereo winds are put at a height that should be at or above the tropopause and above the stereo retrievals. These points are best seen in the planar views of a 3D rendering (**Figure 13** and **Figure 14**).

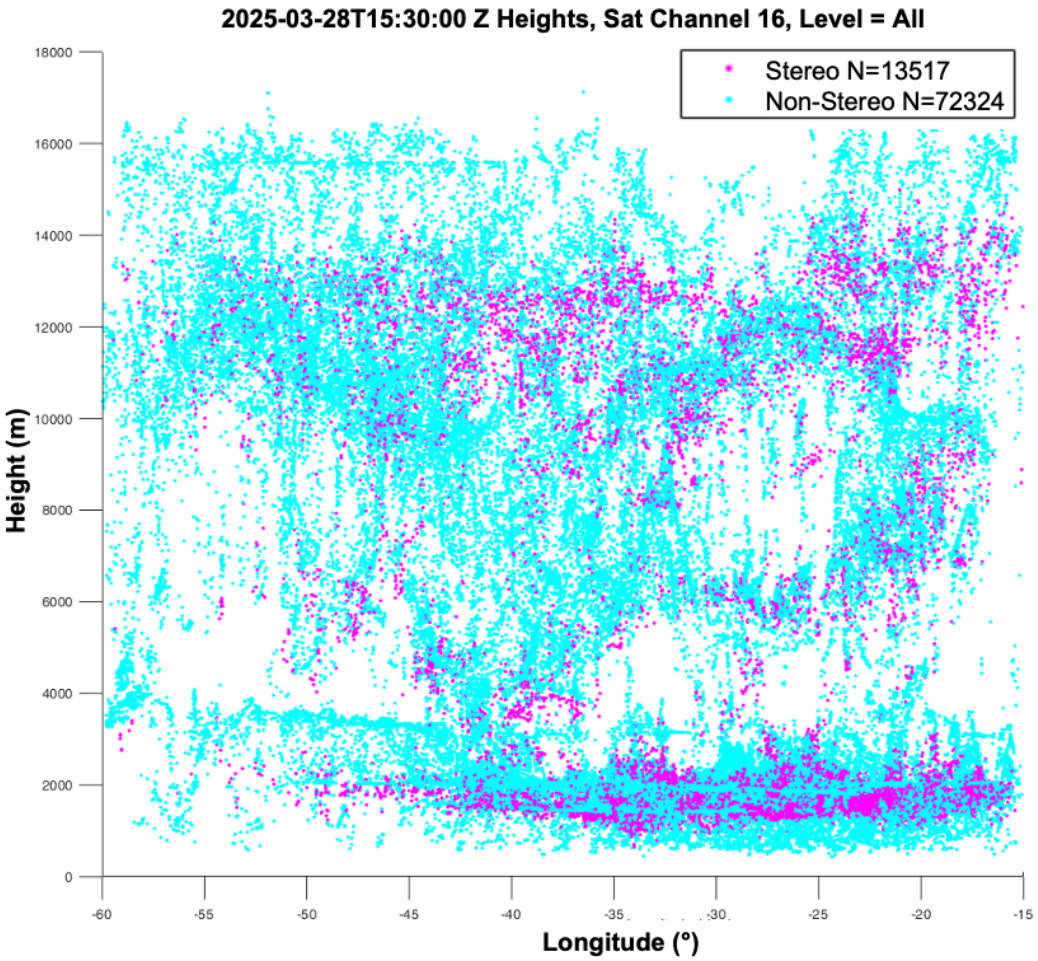


Figure 13. *Stereo and Non-Stereo Heights by Longitude*

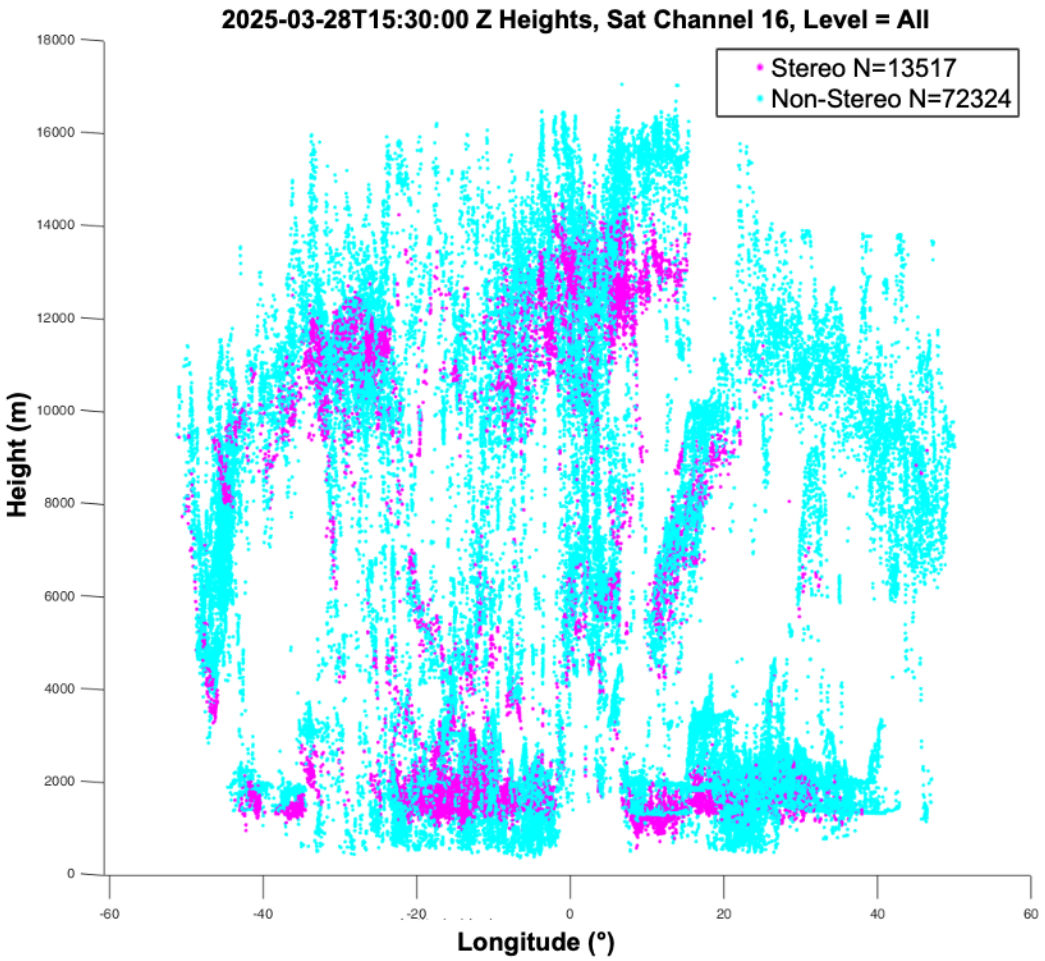


Figure 14. *Stereo and Non-Stereo Heights by Latitude*

The 3D structures are easier to see if we confine ourselves to latitudes to the tropics (**Figure 15**). There are significant differences at all levels.

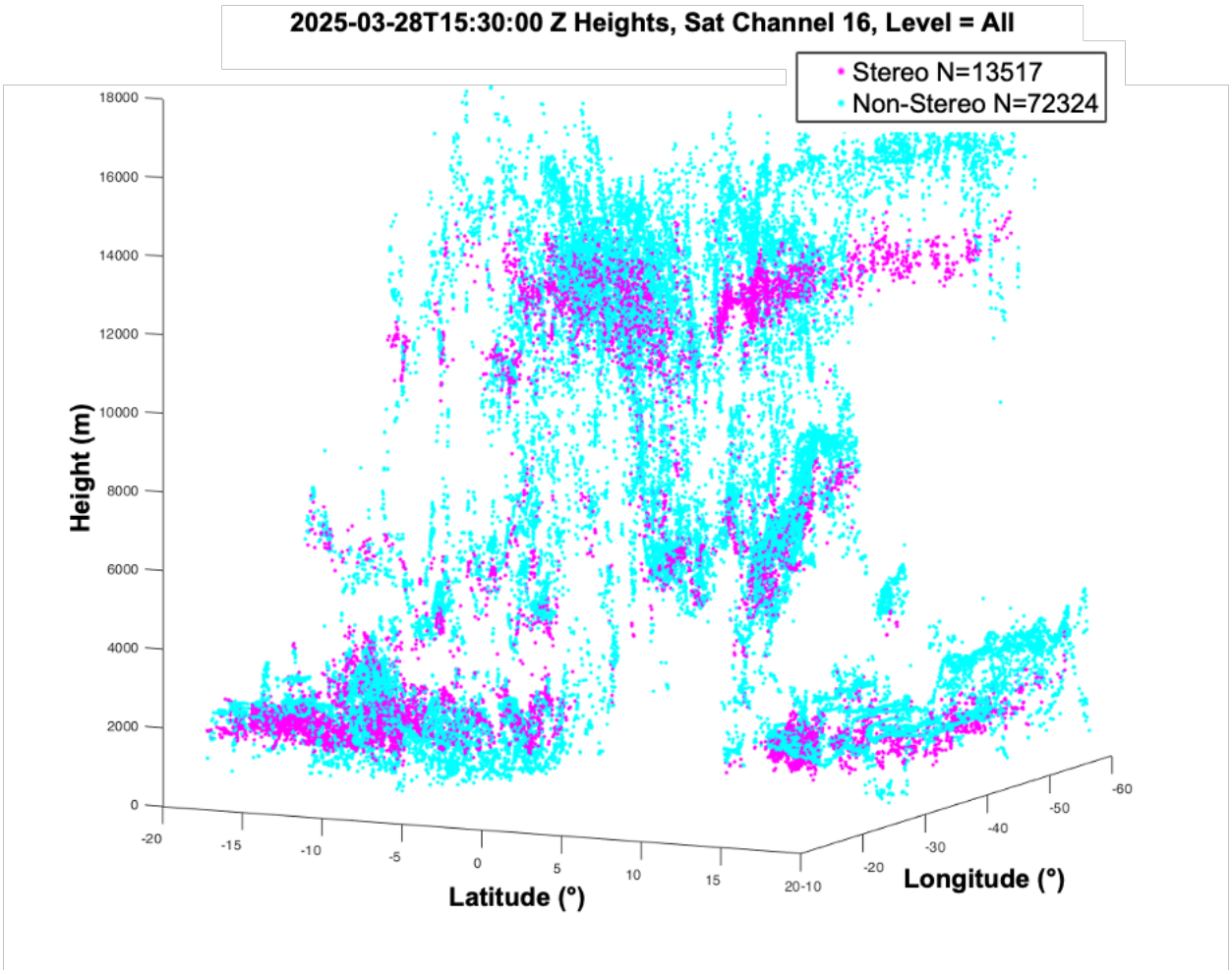


Figure 15. *Stereo and Non-Stereo Heights in the Tropics*

A quantitative comparison is possible when collocating the winds from the respective cases. We do this by finding the nearest non-stereo wind within 4 km of each stereo wind. To gain further insight into the differences, we slice vertically into low (< 2 km), medium (2 km – 6 km), and high (> 6 km) levels to make histograms. **Figure 16** and **Figure 17** show the results for the IR and VIS winds. The height assignment comparisons show the largest differences at higher levels, but low-level differences are an important fraction of the 2000 m low-level ceiling. Height comparisons are similar between IR and VIS. Wind vector differences are not very large, particularly considering that the high-level winds are generally quite strong.

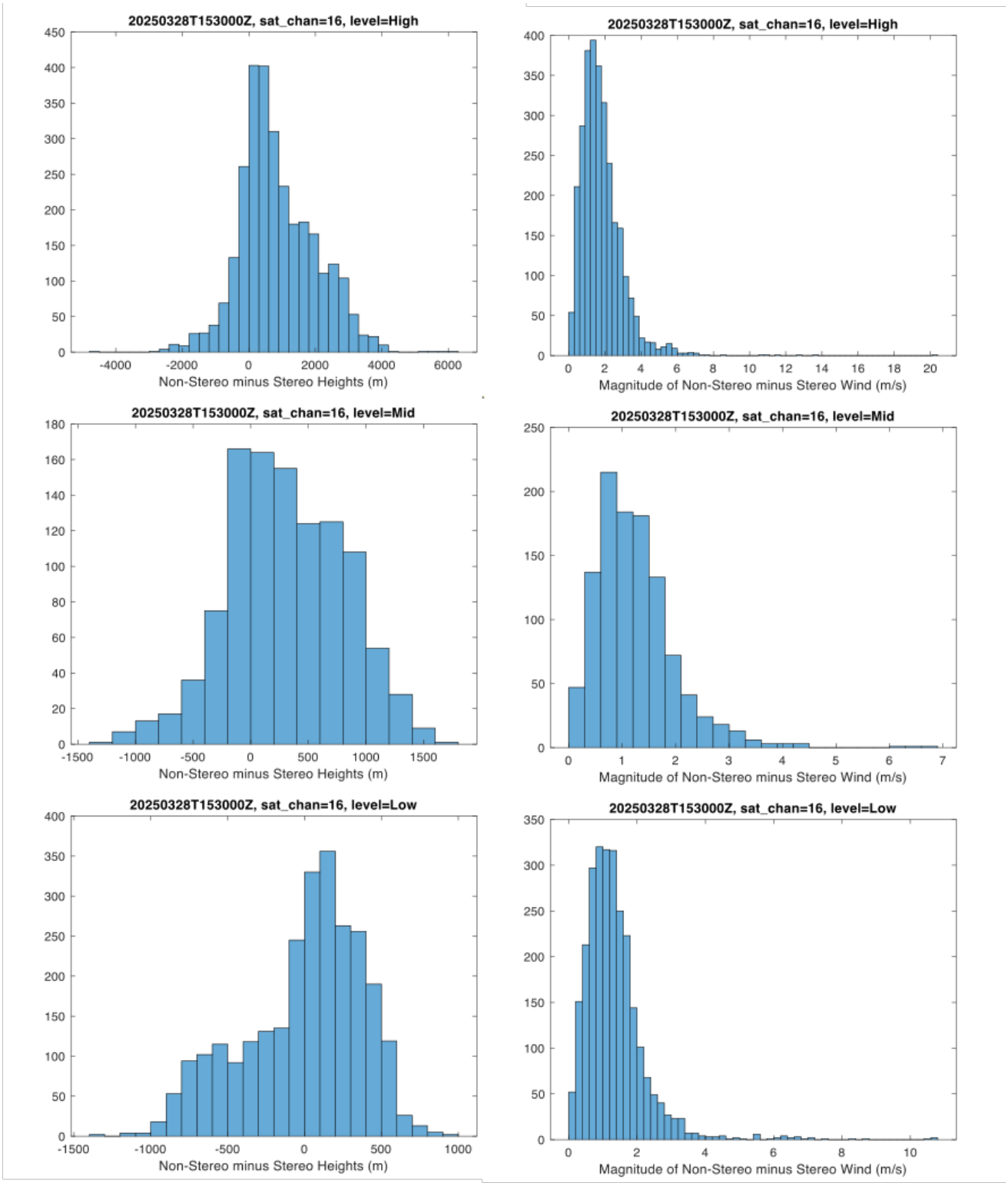


Figure 16. *IR Winds Comparisons*

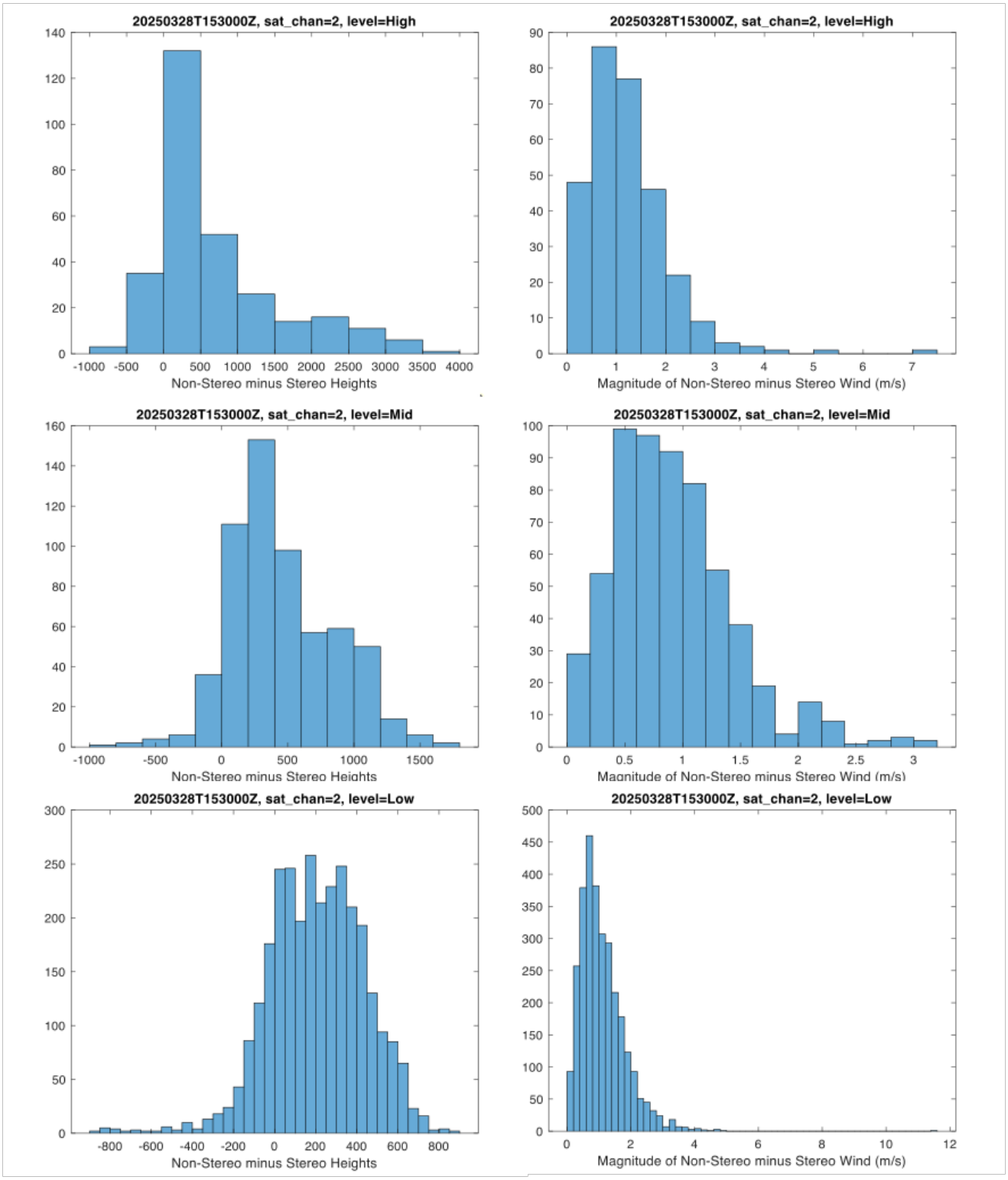


Figure 17. *VIS Winds Comparisons*

The comparison does not say which result is more correct. There are clearly some large differences. Here, LiDAR can be helpful; however, it slices the scene only on a narrow path

and is not continuously present within our test area. It is also difficult to say where the LiDAR finds the top of a tracked feature and how to compare that to the tracer height. We work with the LiDAR Mie attenuated backscatter coefficients rather than a Level-2 cloud top product so that we have a more nuanced picture of the LiDAR measurements. The attenuated backscatter could be integrated down from the satellite to obtain an optical depth but that requires a LiDAR "ratio" that depends on whether the scatterer is liquid-phase or ice. Our examination of the LiDAR data is then necessarily qualitative. The clearest situation is that of a thick stratiform cloud layer. These would typically be low, near the boundary layer. In such cases, the backscattering coefficient abruptly jumps at a rather well-defined cloud top. Except for holes between clouds, the LiDAR and tracer feature heights should be similar and there should be uniformity across the areal extent of the feature. Higher clouds are more problematic, where we will encounter semitransparency (*e.g.*, cirrus clouds), deep convection, and overshooting tops. In the first case, we may not be clear on what the tracer represents, and larger backscattering contributions may come from underneath. In the other cases, there may be considerable inhomogeneity across the extent of the feature that the LiDAR would trace across. On balance, LiDAR observations should be most useful at low levels.

Figure 18 shows one granule of data from EarthCARE as it transits our test area. The LiDAR curtain is shown in **Figure 19**. In this case, we can see at low levels that the stereo winds have more uniform heights.

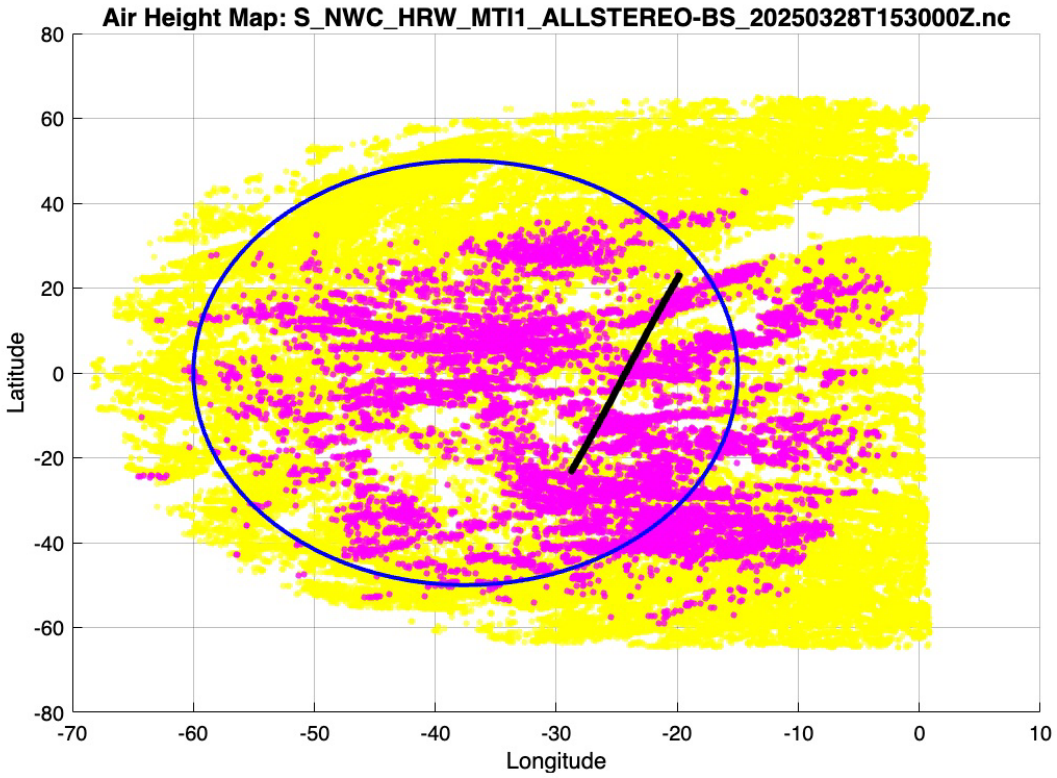


Figure 18. *EarthCARE track through Test Area.*

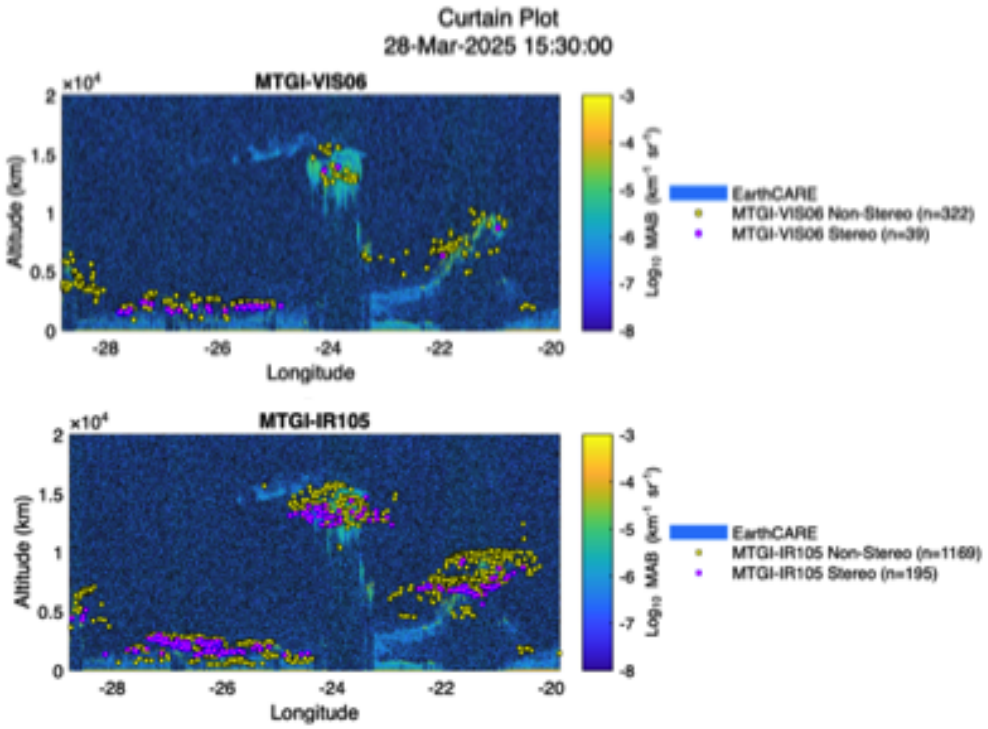


Figure 19. *LiDAR Curtains and Stereo and Non-Stereo Heights.*

We can ask why stereo heights should be trusted even when LiDAR cannot clearly validate height assignments in all regimes. A satellite wind measurement represents the translation of a feature. Even if that feature has a non-stratiform structure, both the temporal and spatial (parallax) translations are measured in the same way so, if the observations conform well with the stereo retrieval model, then the retrieved height should well represent the pattern from which the wind has been derived. We might most properly refer to our retrieved height as the pattern height. It could potentially represent a layer of atmosphere moving essentially with the same velocity (low wind shear), in which case, multiple height assignments could be correct.

Appendix B provides a more complete set of comparisons with EarthCARE.

4.2 Comparison of Stereo and Non-Stereo Winds: ERA5

Comparing stereo and non-stereo winds with ERA5 reanalysis winds is a useful exercise. The winds being compared with reanalysis should not have already been screened for quality with respect to the Numerical Weather Prediction (NWP) used as a first guess. Here, we show a comparison for 28 March 2025 16:00Z (instead of 15:30Z to avoid interpolation of ERA5 in time). ERA5 models the atmosphere hourly, including winds, on 37 pressure levels with a geopotential height at each 0.25-degree grid node. To compare with HRW winds, we pick the closest node and interpolate to the level of the HRW wind. For non-stereo winds, interpolation is by assigned pressure and for stereo winds, it is by geopotential height. The observed wind is then compared with the ERA5 reanalysis wind interpolated to its level. **Figure 20** shows the result. In this case, there is virtually no difference between the two sets of winds.

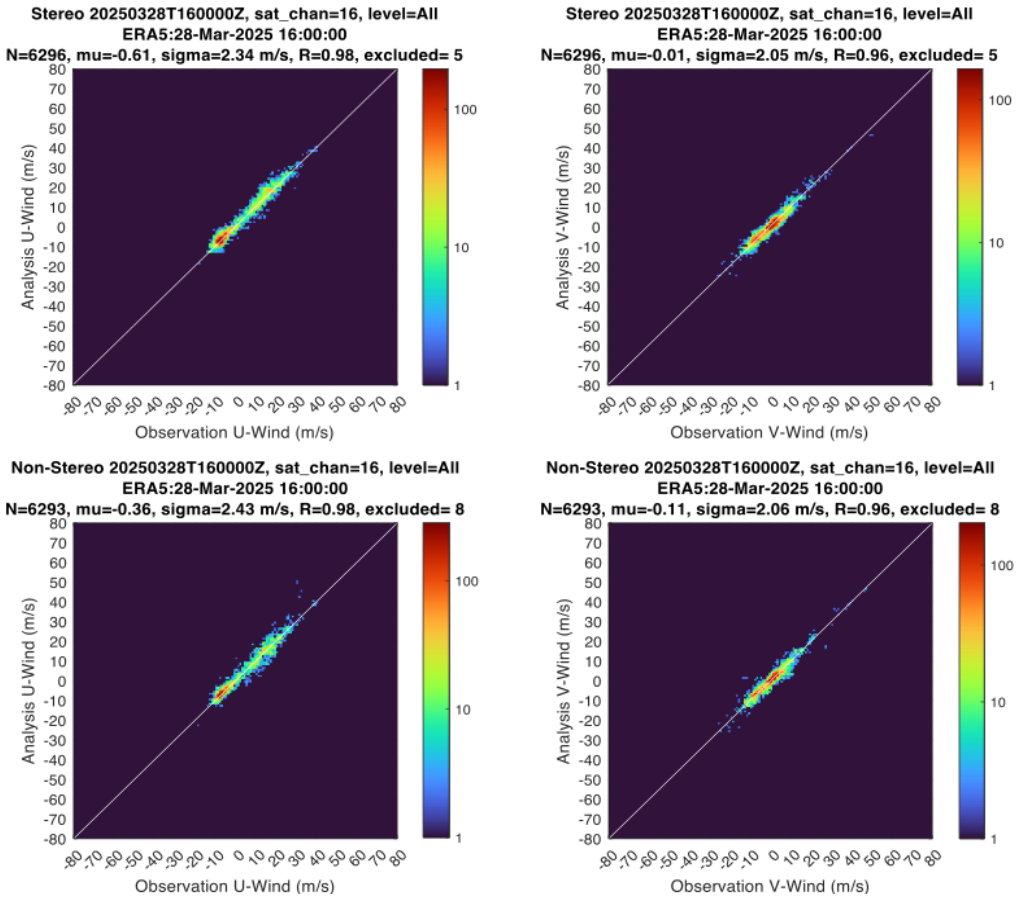


Figure 20. *Comparisons between Observation and Analysis Winds.*

Tabel 1 splits the statistics by level. Appendix C provides a complete set of ERA5 comparison results. We did not assess the WV winds.

Table 1. Summary Statistics for Observation and Analysis Winds by Level.

	Stereo IR			Non-Stereo IR		
Level	<2 km	2 – 6 km	>6 km	<2 km	2 – 6 km	>6 km
N	2120	836	2575	2121	832	2576
Mean(Du) m/s	-0.64	-0.53	-0.61	-0.55	-0.21	-0.23
Sigma(Du) m/s	1.85	1.66	2.94	1.38	1.55	3.36
Mean(Dv) m/s	-0.34	0.25	0.22	-0.22	0.08	-0.03
Sigma(Dv) m/s	1.71	1.78	2.43	1.15	1.67	2.73

5 CONCLUSIONS

5.1 EARTHCARE

The EarthCARE Mie Attenuated Backscatter (MAB) curtain plots did not clearly elucidate which of stereo or non-stereo height assignments better represent the tracked feature. In general, lower-level clouds produce more sharp transitions vertically. Both stereo and non-stereo heights appear to conform well with the visually identifiable cloud tops in these cases, but there are many places where it is ambiguous. For higher clouds, there is more ambiguity in the MAB vertical profiles in so far as identifying the cloud top or tracked feature. Semi-transparency of cirrus cloud is one factor and possibly more variability exists in the cloud top morphology at higher levels relative to lower stratiform clouds. Clear differences are certainly seen between stereo and non-stereo heights for high clouds.

5.2 ERA5

Across the low levels (< 2 km), stereo and non-stereo AMVs exhibit similar mean biases, while non-stereo winds show consistently lower standard deviations, indicating slightly better precision in this layer. In the mid-troposphere (2–6 km), mean biases remain effectively the same for both methods, and although non-stereo winds retain a modest advantage in precision (typically 0.3–0.7 m/s), the differences are small and not operationally significant.

The most pronounced distinctions emerge at high levels (> 6 km). Here, the mean biases of stereo and non-stereo winds remain similar, but the standard deviations generally favor the stereo method, reflecting improved precision in the upper-tropospheric flow where parallax signal is strongest. Overall, the primary benefit of the stereo technique is realized in these high-level winds, where geometric height sensitivity is greatest and the method provides the clearest performance enhancement.

While these results are interesting, we must ask if conformance with reanalysis should be the standard against which to judge the correctness of observed winds or are we engaging in a sort of circular reasoning. Models such as ERA5 assimilate operational winds that are assigned heights using temperature (*e.g.*, CCC) so their modeling of the atmosphere might be expected to conform to whatever errors or biases exist in the operational height assignments. Unfortunately, our LiDAR results did not allow us to resolve this conundrum.

5.3 SUMMARY

In summary, the HRW stereo-winds capability is fully mature and ready for scientific use, with the clearest advantages emerging in the upper troposphere where stereo and non-stereo height assignments diverge most strongly. The ERA5 statistics further highlight the potential benefit of stereo height information at high levels, suggesting improved representation of cloud-top winds relative to background fields. At the same time, additional work is needed to fully interpret these results, particularly to separate true performance gains from sampling differences, and to extend the analysis through targeted comparisons with collocated lidar profiles. Finally, water–vapor channel winds were not

examined in detail in this study, and a dedicated evaluation of water–vapor stereo behavior would be important to complete the overall performance assessment.

6 IMPLEMENTATION WITHIN SAF PRODUCTS

6.1 SOFTWARE AND DOCUMENTATION

All new stereo-winds code developments were implemented, documented, and version-controlled within the NWC/GEO v2025 software package framework using Git. The completed software package was delivered to the NWC SAF Project Team with fully commented source code and a modular structure that enables straightforward extension to additional geostationary satellite pairings. This report provides a detailed technical description of the stereo-winds method, its implementation within HRW, and the associated operational considerations.

The stereo-winds integration required updates across multiple directories and modules:

- COTS/cots.ksh
- COTS/cots_lapack.ksh
- COTS/packages/lapack-3.10.3.tar.gz
- import/Aux_data/HRW
- config/safnwc_HRW*cfg
- include/NWCLIB
- include/HRW
- src/NWCLIB
- src/HRW

The stereo-winds configuration parameters are defined as follows for order-5 using 3 images per satellite
(i.e., *config/safnwc_HRW_WITHSTEREO_SIXCHANNELS_6IMA5ORD.cfm).*

```
##########################################################################
# HRW Stereo Winds Parameters
##########################################################################
# Flag to decide if stereo winds will be computed (0/1)
STEREOWINDS                     1

# Define directory of the second satellite
STEREOWINDSDIR GOES16_GOESR_M6_REP

# Flag to decide stereo winds order (3 or 5)
STEREOWINDS_ORDER               3

# The number of images used for the stereo processing (3 to 6)
STEREOWINDS_NUM_LOOKS           5

# The weightings for least-square fit states for retrieval algorithm.
STEREOWINDS_SIGS                0.2

# The maximum number of iteration for retrieval algorithm
STEREOWINDS_MAX_LOOPS           5
```

```
# The position tolerance for retrieval algorithm
STEREOWINDS_R_TOL               1E-04
# The velocity tolerance for retrieval algorithm
STEREOWINDS_V_TOL               1E-05
# Flag to decide if covariance is calculated for retrieval algorithm
STEREOWINDS_DO_COVL             1
# Limb limit for retrieval algorithm
STEREOWINDS_COS_LIM             0.087155742747658

# Nominal values for MTG
STEREOWINDS_MTG_RAD             4.2164537E+04
STEREOWINDS_MTG_LAT             0.0
STEREOWINDS_MTG_LON             0.0
# Nominal values for GOESR
STEREOWINDS_GOESR_RAD           4.216416E+04
STEREOWINDS_GOESR_LAT           0.0
STEREOWINDS_GOESR_LON           -75.2

# RMS residuals threshold
RMS_RESIDUALS_THRESHOLD         0.25
```

Outputs of the stereo winds are produced in both NetCDF and BUFR formats, consistent with existing NWC/GEO-HRW product conventions. An example of the additional stereo outputs are as follows.

- stereo_height_error
- stereo_latitudinal_displacement
- stereo_latitudinal_displacement_error
- stereo_latitudinal_wind_error
- stereo_longitudinal_displacement
- stereo_longitudinal_displacement_error
- stereo_longitudinal_wind_error
- stereo_root_mean_squared_residuals

Stereo wind retrievals are executed through the GEO-HRW-v70 workflow using the same structure:

```
GEO-HRW-v70 [@ nominal timestamp] safnwc_ALLSTEREO.cfg safnwc_HRW*.cfm
```

6.2 Additional Software Package

A BLAS/LAPACK package (lapack-3.10.3.tar.gz) was created and integrated into the NWCSAF_GEO-v2025/COTS/packages directory. The cots.ksh installation script was updated to enable proper deployment of the new library, and BLAS/LAPACK components were installed into both the lib and include directories under NWCSAF_GEO-v2025/COTS. Future updates to the bundle NWC-CDOP4-GEO-AEMET-SW-CODE-COTS_v2025.0_15DEC24.tgz should include the LAPACK package and revised cots.ksh.

System requirement: the new BLAS/LAPACK package requires GNU glibc ≥ 2.29, corresponding to Ubuntu ≥ 19.04 or RHEL/CentOS ≥ 9.

7 REFERENCES

Ref	Title	Code & Version / Journal & DOI
[RD.1]	The Nowcasting SAF Glossary	NWC/CDOP3/SAF/AEMET/MGT/GLO https://www.nwcsaf.org/aemetRest/downloadAttachment/7150
[RD.2]	Identifying the uncertainty in determining satellite-derived atmospheric motion vector height attribution. Velden, C. S., and K. M. Bedka, 2009	J. Appl. Meteor. Climatol., 48, 450–463 https://doi.org/10.1175/2008JAMC1957.1
[RD.3]	Algorithm Theoretical Basis Document for the Wind product processor of the NWC/GEO	NWC/CDOP2/GEO/AEMET/SCI/ATBD/Wind v1.1.1 https://www.nwcsaf.org/Downloads/GEO/2025/Documents/Scientific_Docs/NWC-CDOP2-MTG-AEMET-SCI-ATBD-Wind_v1.1.1.pdf
[RD.4]	Cloud Motion and Height Measurements from Multiple Satellites Including Cloud Heights and Motions in Polar Regions, James F. W. Purdom & Patrick N. Dills.	Second International Winds Workshop, Tokyo/Japan, 1993 http://cimss.ssec.wisc.edu/iwwg/2nd%20Wind%20Workshop/p245-248_Purdom-Cloud%20Motion.pdf
[RD.5]	Advances in Stereo Winds, J.Carr, J.Daniels, D.Wu, W.Bresky, H.Madani, M.Friberg, T.Summers	Sixteenth International Winds Workshop, Montréal/Canada, 2023 https://www.ssec.wisc.edu/meetings/iwwg/2023-meeting/presentations/advances-in-stereo-winds/
[RD.6]	GEO–GEO Stereo-Tracking of Atmospheric Motion Vectors (AMVs) from the Geostationary Ring, Carr, J.L.; Wu, D.L.; Daniels, J.; Friberg, M.D.; Bresky, W.; Madani, H.	Remote Sensing 2020, 12, 3779. https://doi.org/10.3390/rs12223779
[RD.7]	Evaluation of NASA/NESDIS Stereo Winds in the Navy Global Forecast System. Stone RE, Pauley PM, Tyndall DP, Reeves JM	Monthly Weather Review. 2025 Oct; 153(10):1959-85 https://journals.ametsoc.org/view/journals/mwre/153/10/MWR-D-24-0101.1.xml
[RD.8]	Multi-LEO satellite stereo winds. Carr JL, Wu DL, Friberg MD, Summers TC.	Remote Sensing. 2023 Apr 19;15(8):2154. https://doi.org/10.3390/rs15082154
[RD.9]	Stereo plume height and motion retrievals for the record-setting Hunga Tonga-Hunga Ha'apai eruption of 15 January 2022. Carr JL, Horváth Á, Wu DL, Friberg MD.	Geophysical Research Letters. 2022 May 16;49(9):e2022GL098131. https://doi.org/10.1029/2022GL098131
[RD.10]	MISR-GOES 3D Winds: Implications for Future LEO-GEO and LEO-LEO Winds. Carr JL. Wu D, A. Kelly M, Gong J.	Remote Sensing. 2018 Nov 27;10(12):1885. https://doi.org/10.3390/rs10121885
[RD.11]	Joint 3D-wind retrievals with stereoscopic views from MODIS and GOES. Carr JL, Wu DL, Wolfe RE, Madani H, Lin G, Tan B.	Remote Sensing. 2019 Sep 9;11(18):2100. https://doi.org/10.3390/rs11182100
[RD.12]	Geometric estimation of volcanic eruption column height from GOES-R near-limb imagery–Part 1: Methodology. Horváth Á, Carr JL, Girina OA, Wu DL, Bril AA, Mazurov AA, Melnikov DV, Hoshyaripour GA, Buehler SA.	Atmospheric Chemistry and Physics. 2021 Aug 16;21(16):12189-206. https://doi.org/10.5194/acp-21-12189-2021

Ref	Title	Code & Version / Journal & DOI
[RD.13]	Geometric estimation of volcanic eruption column height from GOES-R near-limb imagery–Part 2: Case studies. Horváth Á, Girina OA, Carr JL, Wu DL, Bril AA, Mazurov AA, Melnikov DV, Hoshyaripour GA, Buehler SA.	Atmospheric Chemistry and Physics Discussions. 2021 Mar 23;2021:1-37. https://doi.org/10.5194/acp-21-12207-2021
[RD.14]	Measurement report: Plume heights of the April 2021 La Soufrière eruptions from GOES-17 side views and GOES-16–MODIS stereo views. Horváth Á, Carr JL, Wu DL, Bruckert J, Hoshyaripour GA, Buehler SA.	Atmospheric Chemistry and Physics Discussions. 2022 May 10;2022:1-24. https://doi.org/10.5194/acp-22-12311-2022
[RD.15]	Influence of Fire-Induced Heat and Moisture Release on Pyro-Convective Cloud Dynamics During the Australian New Year's Event: A Study Using Convection-Resolving Simulations and Satellite Data. Muth LJ, Bierbauer S, Hoose C, Vogel B, Vogel H, Hoshyaripour GA.	EGUsphere. 2025 Feb 11;2025:1-22. https://doi.org/10.5194/acp-25-16027-2025
[RD.16]	Diurnal Observations of Wildfires Boundary Layer Dynamics and Aerosol Plume Convection using Stereo-Imaging Techniques. Friberg M, Wu D, Carr J, Limbacher J, Zou Y, O'Neill S.	EGU General Assembly Conference Abstracts 2021 Apr (pp. EGU21-16351). https://doi.org/10.5194/egusphere-egu21-16351
[RD.17]	Evolution of an atmospheric Kármán vortex street from high-resolution satellite winds: Guadalupe Island case study. Horváth Á, Bresky W, Daniels J, Vogelzang J, Stoffelen A, Carr JL, Wu DL, Seethala C, Günther T, Buehler SA.	Journal of Geophysical Research: Atmospheres. 2020 Feb 27;125(4):e2019JD032121. https://doi.org/10.1029/2019JD032121
[RD.18]	A GEO-GEO Stereo Observation of Diurnal Cloud Variations over the Eastern Pacific. Wu DL, Carr JL, Friberg MD, Summers TC, Lee JN, Horváth Á.	Remote Sensing. 2024 Mar 24;16(7):1133. https://doi.org/10.3390/rs16071133
[RD.19]	Advanced Kalman filtering, least-squares and modeling: a practical handbook. Gibbs BP.	John Wiley & Sons; 2011 Mar 29. https://onlinelibrary.wiley.com/doi/book/10.1002/9780470890042

8 APPENDICES

APPENDIX A – STEREO WINDS RETRIEVAL MATHEMATICAL ALGORITHM DESCRIPTION (ATBD CHAPTER)

The stereo winds method has been developed for several different cases, including pairs of geostationary satellites [RD.6], a geostationary and a polar orbiting satellite [RD.10, 11], and multiple polar orbiting satellites [RD.8]. The description of the stereo-winds implementation for HRW presented here draws on work originally supported by NASA and later NOAA using the GOES-R ABI [RD.6]. Research implementations of stereo winds exist at NASA and NOAA, with the latter being prepared for a transition to an operational product supporting pairs of GOES and Himawari satellites. Future operational extensions at NOAA may include ABI-VIIRS stereo winds. The NASA research code has been used for several studies, including volcanoes [RD.9, 12 13, 14], wildfires [RD.15, 16], von Karman vortices [RD.17], and the diurnal cycle of the boundary layer [RD.18].

The stereo-wind retrieval is an optimization problem using the apparent locations of a tracer on the ellipsoid as seen by FCI and ABI at various times. One of the scenes is designated to be the "reference" scene from which the tracking template is taken. We designate it as the "A0" scene. Other repetitions from the same satellite are designated "A1", "A2", etc. The other satellite is designated as the "B" satellite. For HRW, the reference scene "A0" will be from FCI, and the "B" scenes are from ABI (in a parallel NASA implementation, the roles of FCI and ABI are swapped). The apparent location of the tracer on the ellipsoid and a time tag for its acquisition in each scene will have been found already by pattern matching.

The mathematics of the retrieval algorithm is explained with reference to **Figure 1**. It shows the view of a tracer from satellite n ($n = 0$ is A0, $n \neq 0$ are A1, B0, B1, etc.) with position vector $\vec{R}_n$. The apparent location $\vec{r}_0$ of the tracer on the ellipsoid as seen in A0 is marked. The three-dimensional location of the tracer relative to this point on the ellipsoid is $\vec{\delta}$, which can be decomposed into a horizontal distance the wind ($\vec{V}$) has carried it in the time $t_n - t_0$ and a vertical height $h\hat{w}$. The unit vector $\hat{w}$ is perpendicular to the tangent plane at A0 and $\vec{V} \cdot \hat{w} = 0$. The apparent location $\vec{r}_n$ of the tracer on the ellipsoid as observed by satellite $n \neq 0$ is similarly marked.

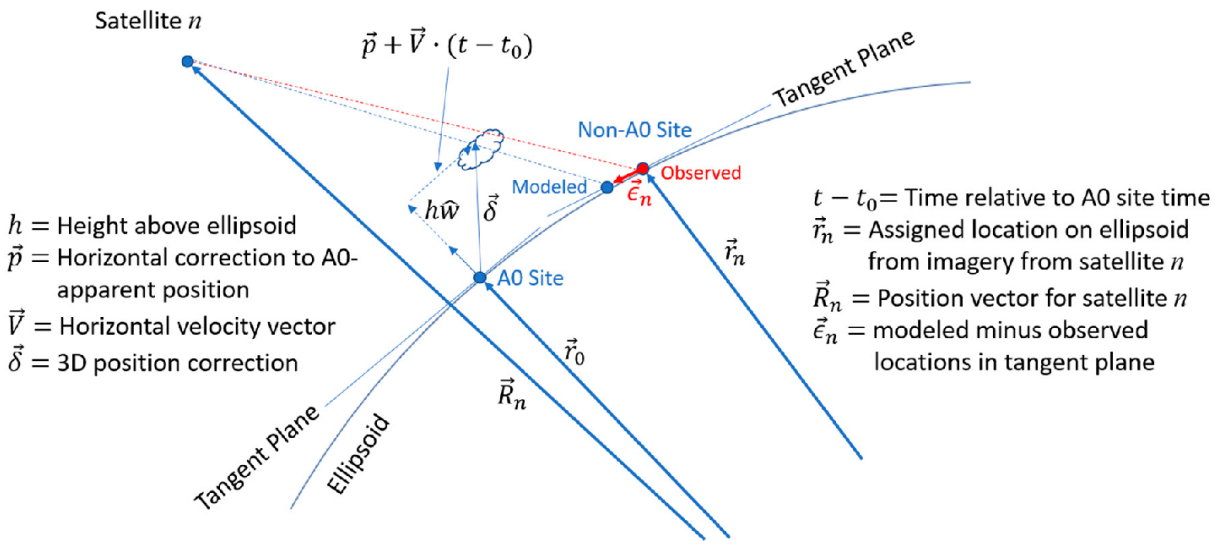


Figure 1. *Geometry for the Retrieval Algorithm*

The optimization problem seeks to minimize the sum of the weighted squared deviations between the modeled and observed apparent locations of the tracer across all scenes. This is expressed mathematically in Equation (1).

$$\chi^2 = \sum_{n=1}^{N} \vec{\epsilon}_n{}^T W_n \vec{\epsilon}_n \tag{1}$$

The weighting matrices W_n will be taken to be diagonal with the diagonal elements being inverse to the assumed errors in measurement ($= \frac{1}{\sigma^2}$). The residual displacements $\vec{\epsilon}_n$ are in the tangent plane at the site of each observation and represent the distance between the observed and modeled apparent sites. Two models are supported. The first is a three-parameter model $X = \left[h, \vec{V}\right]^T$ and the second is a five-parameter model $X = \left[\vec{p}, h, \vec{V}\right]^T$. In the first case, the vector $\vec{\delta}$ is constrained so that it points from the apparent site A0 to the A0 satellite (*i.e.*, along its line of sight). In the second case, the apparent position of A0 can be adjusted in the tangent plane supposing that there may have been a small error in the Image Navigation and Registration (INR) of the A0 satellite. Such an INR error will be absorbed into $\vec{p}$, otherwise it will find its way into the residuals.

The problem is mildly nonlinear in X, and solved iteratively where at each step a change ΔX is computed from a linearized version of the problem. The iteration is stopped when certain convergence criteria are met, or the maximum number of allowable loops have been attempted without converging (failure). The convergence can also fail in the pathological case where applying $\Delta\vec{p}$ for the next iteration would put the tracer over the horizon or too close to the limb from one of the satellites (rare occurrence). Below, we describe and derive each step in this process, which has been implemented in hrw_Retrieve3DWind.c.

The general solution to this kind of problem is as follows. Given a guess X, we imagine an updated guess $X + \Delta X$ and expand each $\vec{\epsilon}_n$ as a Taylor series to linear order in ΔX as in Equation (2).

$$\chi^2 \cong \sum_{n=1}^{N} (\vec{\epsilon}_n(X) + A_n \cdot \Delta X)^T W_n (\vec{\epsilon}_n(X) + A_n \cdot \Delta X) \tag{2}$$

The matrix A_n is the 2-by-3 (or 2-by-5) matrix of partial derivatives of $\vec{\epsilon}_n$ with respect to each component of X. Each update is calculated to minimize χ^2. We find this minimum by differentiating χ^2 with respect the ΔX and setting that to zero. The result is a linear system of equations that can be solved using any standard method of linear algebra as in Equation (3).

$$\left(\sum_{n=1}^{N} {A_n}^T W_n A_n\right) \cdot \Delta X + \sum_{n=1}^{N} {A_n}^T W_n \vec{\epsilon}_n(X) = 0 \tag{3}$$

A necessary condition for the coefficient matrix to be nonsingular and there is a unique solution is that the number of scalar measurements exceeds the number of parameters being solved. Each pairing A1-A0, A2-A0, B0-A0, etc. contributes two scalar measurements as $\vec{\epsilon}_n$ sits in a two-dimensional tangent plane; therefore, we need to have $2N > 3$ or $2N > 5$, counting zero as the reference scene. The loop is terminated when the norm of the position components of ΔX and the norm of the velocity components of ΔX are both less than specified tolerances.

It remains to describe the calculations of $\vec{\epsilon}_n$ and A_n. The first term on the right in Equation (4) is a vector to the tracer with a scale factor $\lambda > 1$ applied such that it extends towards the surface from the $n = 0$ satellite. The second term is a vector from satellite $n \neq 0$ to the observed apparent location of the tracer.

$$\vec{\epsilon}_n = \lambda\left(\vec{r}_0 + \vec{\delta} - \vec{R}_0\right) - \left(\vec{r}_n - \vec{R}_n\right) \tag{4}$$

Since $\vec{\epsilon}_n$ is to be in the tangent plane at $\vec{r}_n$, it must be perpendicular to the local vertical $\hat{w}_n$ there, *i.e.*, $\hat{w}_n \cdot \vec{\epsilon}_n = 0$, which is a condition that allows us to solve for λ in Equation (5).

$$\lambda = \frac{\hat{w}_n \cdot (\vec{r}_n - \vec{R}_n)}{\hat{w}_n \cdot \left(\vec{r}_0 + \vec{\delta} - \vec{R}_0\right)} \tag{5}$$

Therefore,

$$\vec{\epsilon}_n = \frac{\hat{w}_n \cdot (\vec{r}_n - \vec{R}_n)}{\hat{w}_n \cdot \left(\vec{r}_0 + \vec{\delta} - \vec{R}_0\right)} \left(\vec{r}_0 + \vec{\delta} - \vec{R}_0\right) - \left(\vec{r}_n - \vec{R}_n\right) \tag{6}$$

The vector $\vec{\delta}$ is parameterized by either five or three independent variables X:

$$\vec{\delta}(X) = \begin{cases} \vec{p} + h\hat{w}_0 + \vec{V} \cdot (t_n - t_0) & X = \left[\vec{p}, h, \vec{V}\right]^T \\ h \cdot \frac{\vec{R}_n - \vec{r}_0}{\hat{w}_0 \cdot (\vec{R}_n - \vec{r}_0)} + \vec{V} \cdot (t_n - t_0) & X = \left[h, \vec{V}\right]^T \end{cases} \tag{7}$$

We substitute these definitions directly in Equation (6) to calculate $\vec{\epsilon}_n(X)$ and to also find the matrix of partial derivatives A_n for the two cases:

$$A_n = \frac{\hat{w}_n \cdot (\vec{r}_n - \vec{R}_n)}{\hat{w}_n \cdot \left(\vec{r}_0 + \vec{\delta} - \vec{R}_0\right)} \left(I - \frac{\vec{r}_0 + \vec{\delta} - \vec{R}_0}{\hat{w}_n \cdot \left(\vec{r}_0 + \vec{\delta} - \vec{R}_0\right)} \, {\hat{w}_n}^T \right) \frac{\partial \vec{\delta}}{\partial X} \tag{8}$$

The position vector calculations are coded in a geographic frame where the xy-plane is the equator and the x-axis is at the Greenwich Meridian; however, we wish to represent the winds in a local coordinate system at $\vec{r}_0$ where the frame is defined by a triad of unit vectors that are respectively east-pointing (u, zonal), north-pointing (v, meridional), and vertical (w). We define a matrix $M_0 = [\hat{u}_0 \; \hat{v}_0 \; \hat{w}_0]$, with each column being a triad vector in the geographic frame, that transforms vector components from the local tangent frame into the geographic frame. The matrix ${M_0}^T$ does the inverse. In the two parameterizations (recall that $\vec{V} \cdot \hat{w} = 0$) in our model),

$$\frac{\partial \vec{\delta}}{\partial X} = \begin{cases} [\hat{u}_0 \; \hat{v}_0 \;\; \hat{w}_0 \; (t_n - t_0)\hat{u}_0 \; (t_n - t_0)\hat{v}_0] \\ \left[\frac{\vec{R}_n - \vec{r}_0}{\hat{w}_0 \cdot (\vec{R}_n - \vec{r}_0)} \; (t_n - t_0)\hat{u}_0 \; (t_n - t_0)\hat{v}_0 \right] \end{cases} \tag{9}$$

The linear system in Equation (3) expressed in the local tangent frame is, therefore,

$$\left(\sum_{n=1}^{N} {M_0}^T {A_n}^T W_n A_n M_0 \right) \cdot \Delta X = \sum_{n=1}^{N} {M_0}^T {A_n}^T W_n b_n$$

$$b_n = -\vec{\epsilon}_n(X) \tag{10}$$

$$\Delta X = \begin{cases} [p_u \; p_v \; h \; V_u \; V_v]^T \\ [h \; V_u \; V_v]^T \end{cases}$$

When the weights relate approximately to the uncertainty of the measurements, the coefficient matrix $\sum_{n=1}^{N} {A_n}^T W_n A_n$ can be useful to estimate the uncertainty for the retrieved variables in accordance with least-squares fitting theory (*e.g.*, Gibbs, 2011 [RD.19]). We can see this easily by assuming that we have a solution under perfect conditions and then we add noise so that each b_n is a pair of zero-mean random numbers with covariance $cov(b_n) = R_n$. Let's assume independence across n, and calculate expectation values ($E[\,\cdot\,]$) across an ensemble of trials using Equations (10).

First, calculate

$$E\left[\left(\sum_{n=1}^{N} {M_0}^T {A_n}^T W_n A_n M_0 \right) \cdot \Delta X \right] = \left(\sum_{n=1}^{N} {M_0}^T {A_n}^T W_n A_n M_0 \right) \cdot E[\Delta X]$$

$$= E\left[\sum_{n=1}^{N} {M_0}^T {A_n}^T W_n b_n \right] = \sum_{n=1}^{N} {M_0}^T {A_n}^T W_n E[b_n] = 0 \tag{11}$$

From which we conclude that $E[\Delta X] = 0$, so the distribution of retrieval errors is zero mean.

Now consider the second order statistic $E[\Delta X \cdot \Delta X^T]$. We take advantage of the symmetry of the matrices and the assumed independence of the measurements, so that $E\left[b_n {b_m}^T\right]$ is nonzero only when $n = m$, *i.e.*, $E\left[b_n {b_m}^T\right] = R_n$, and calculate

$$E[\Delta X \cdot \Delta X^T] = \left(\sum_{n=1}^{N} {M_0}^T {A_n}^T W_n A_n M_0\right)^{-1} \cdot E\left[\left(\sum_{n=1}^{N} {M_0}^T {A_n}^T W_n b_n\right) \cdot \left(\sum_{n=1}^{N} {M_0}^T {A_n}^T W_n b_n\right)^T\right] \cdot \left(\sum_{n=1}^{N} {M_0}^T {A_n}^T W_n A_n M_0\right)^{T-1} \quad (12)$$

$$= \left(\sum_{n=1}^{N} {M_0}^T {A_n}^T W_n A_n M_0\right)^{-1} \left(\sum_{n=1}^{N} {M_0}^T {A_n}^T W_n R_n W_n A_n M_0\right) \left(\sum_{n=1}^{N} {M_0}^T {A_n}^T W_n A_n M_0\right)^{-1}$$

Now, if we had selected $W_n = R_n^{-1}$ then Equation (12) reduce to the statement that the covariance of the retrieval uncertainty is the inverse of the coefficient matrix of Equation (10).

$$cov(X) = E[\Delta X \cdot \Delta X^T] = \left(\sum_{n=1}^{N} {M_0}^T {A_n}^T W_n A_n M_0\right)^{-1} \quad (13)$$

The uncertainties on each retrieved parameter individually would be the square-root of the diagonal elements of $cov(X)$.

We remarked earlier that it is necessary to have $2N > 3$ or $2N > 5$, in the three- or five-parameter model, where N is the number of scenes other than the reference one. The overdetermination is then either $2N - 3$ or $2N - 5$. Overdetermination is generally a good thing in fitting problems if random measurement errors were the only factor to consider. However, there is an implicit assumption in satellite winds that the tracer is only translating. This assumption is best respected when the time between observations is least but then that makes the translation smaller and harder to distinguish from noise. If we continue to add extra scenes for more overdetermination then the assumption becomes less well respected, so there is a tradeoff. There are several obvious configurations that can work. With the three-parameter model, we can have as few as three scenes ($N = 2$), *e.g.*, (A0, A1, B0) or (A0, B0, B1) that go back only one time stamp from A0. With the five-parameter model, we need at least four scenes *e.g.*, (A0, A1, B0, B1). Both cases are overdetermined by only one. In the three-parameter case, there is no loss in treating the A and B satellites equivalently, so (A0, A1, B0, B1) is a better choice. This configuration would be overdetermined by three. In the five-parameter case, it would seem that we would pay a penalty against the translation assumption for adding scenes; however, this need not be the case. Consider (A0, A1, A2, B0, B1, B2), which is overdetermined by five, where A0 is slot T, A1 is slot $T - \Delta T$, and A2 is slot $T + \Delta T$ and similarly for the B satellite with repeat period ΔT. Since all matches are against a tracer template from A0, they are never further than ΔT away. This is the usual configuration chosen for the NASA research code and the preoperational NOAA code. The penalty is that winds are produced one slot behind in a real-time system. Even with (A0, A1, A2) and (B0, B1, B2) ordered backwards in time, the benefit of overdetermination is an incentive for using six scenes. There is no reason that this configuration could also not apply to the three-parameter model.

In general, we prefer the five-parameter model because INR errors (the geographic assignments to the A0 tracers) are generally systematic. Such errors would find their way into the residuals, and we would like the residuals to be noise-like. Noise-like residuals can be used for testing whether the data being fit is likely conforming to the model (*i.e.*, the tracer translates as it moves in the wind and the parallax observed is related to the height). If the measurement errors were simply Gaussian then the mean-squared statistics of the residuals would be expected to be chi-squared with degrees of freedom equal to the overdetermination. The real world is more complicated, and we don't exactly know the underlying distribution; however, we can empirically make it from the ensemble of all wind retrievals. Some experimentation can determine what threshold to apply to the root-mean-squared residual to screen out cases that are possibly nonconforming with the model from erroneous matches or other reasons.

Table 2 provides a key to the variables in the hrw_Retrieve3DWind.c and their relationships with the symbols used in the mathematical description above.

Table 2. *Key to the C-Code Variables.*

Symbol in C Code	**Meaning**	**Symbol in Mathematical Description**
xsol	Solution vector	X
look, ref	Indexing of the satellite scenes with ref being the reference scene	ref is always zero in the description but can be nonzero in the code
site_lats, site_lons	Apparent tracer locations on the ellipsoid.	-
rs, zs	Site location and local vertical for each (lat, lon)	$\vec{r}_n$, $\hat{w}_n$
pr0, e0, n0, pz0	Reference site location and the triad of vectors defining the tangent plane frame	$\vec{r}_0$, $[\hat{u}_0\ \hat{v}_0\ \hat{w}_0]$
hdir0	Vector along line of sight that if multiplied by tracer height puts the tracer at the proper place along this line for that height	$\frac{\vec{R}_n - \vec{r}_0}{\hat{w}_0 \cdot (\vec{R}_n - \vec{r}_0)}$
Rs	Satellite position vector in the geographic frame	$\vec{R}_n$

matM0	Matrix to transform vector components from the local tangent frame into the geographic frame	M_0
site_times	Tracer acquisition times	t_n
sumATA, sumATb	Coefficient matrix and vector on the righthand side of the linear system to be solved	Equation (10)
lambda0	Multiplier to scale vector to put on surface of Earth	λ
sigs	Assumed measurement uncertainties	R_n has these squared for diagonal elements
cov	Covariance of X	$cov(X)$
resids	Residuals after convergence	$\vec{\epsilon}_n = A_n \Delta X - b_n$
conf	Configuration structure	-
order	Solution order (3 or 5)	-

The configuration structure includes the structure members in Table 3.

Table 3. *Configuration Structure Members.*

Member	**Meaning**	**Recommended Value**
conf.max_loops	Loop timeout	5
conf.rtol	Position convergence tolerance	1e-4 [km]
conf.vtol	Velocity convergence tolerance	1e-5 [km/s]
conf.cos_lim	Limit on closeness to limb (Earth central angle from either satellite). Algorithm fails if a step is taken beyond this limit.	cos(85°)

conf.do_cov	Controls if covariance is calculated (can avoid a matrix inversion)	1

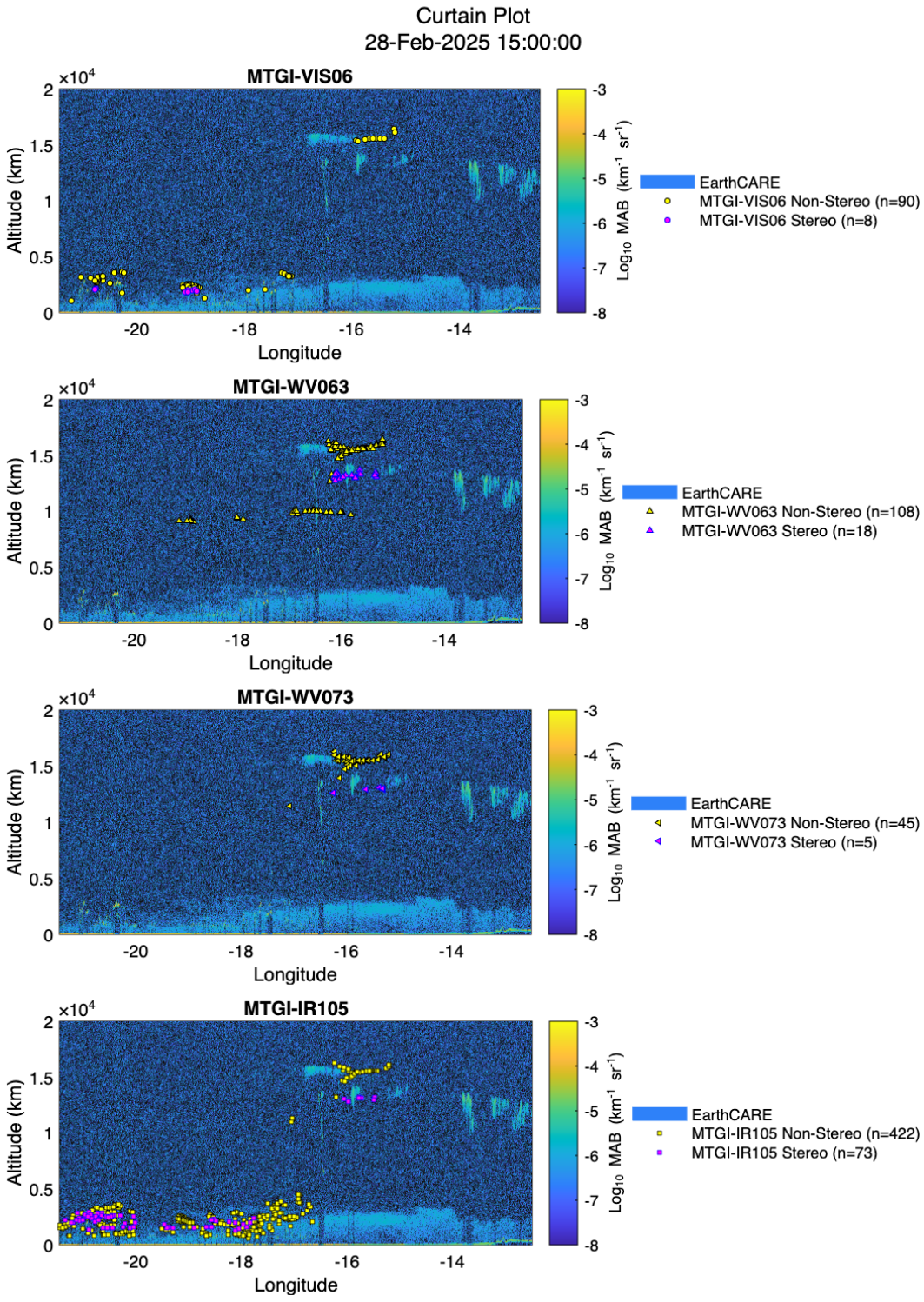
In practice, failure to converge with a loop timeout or stepping out of the Earth central angle limit are rare with the recommended configuration.

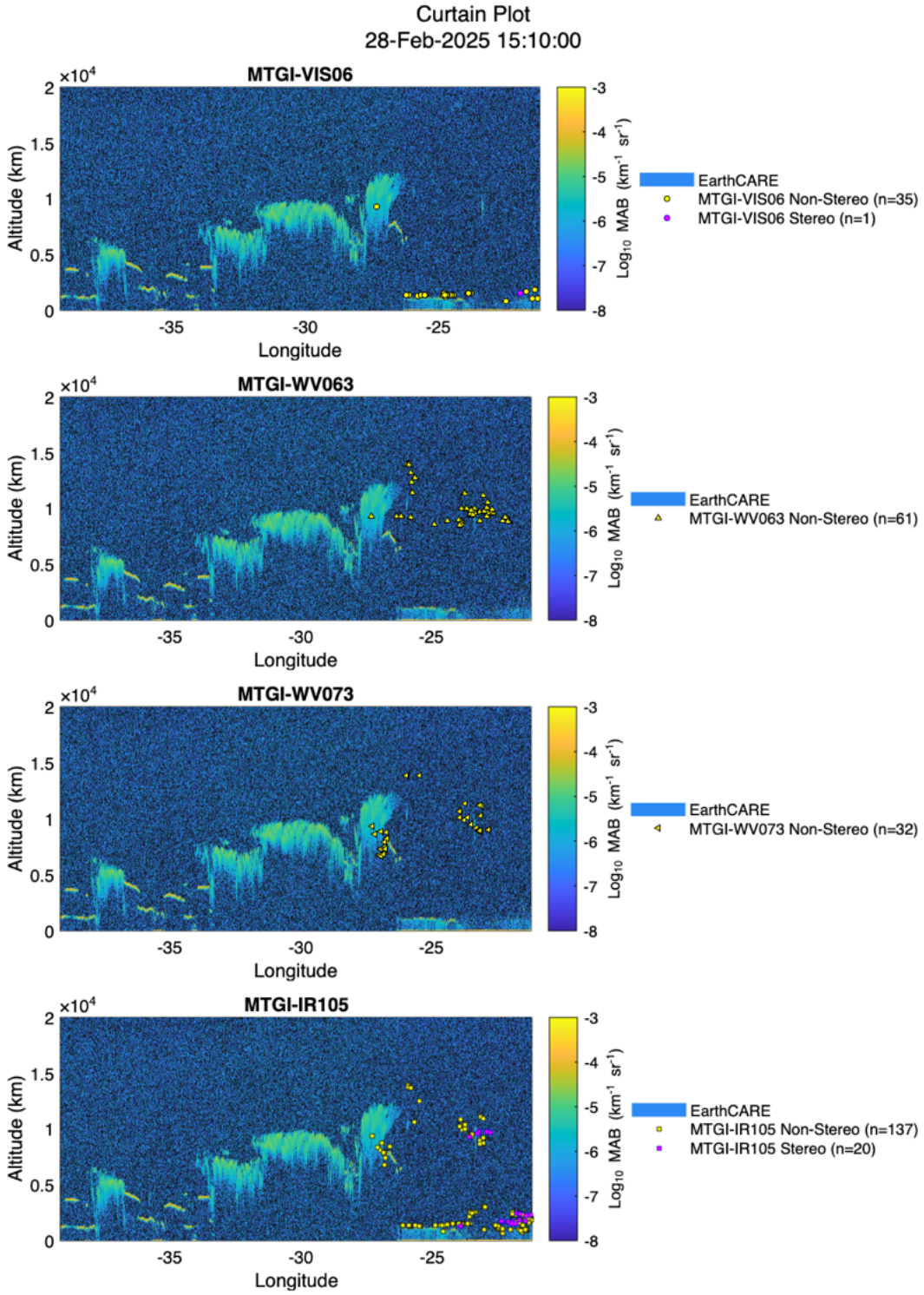
Additionally, we recommend filtering retrievals for quality by rejecting those with root-mean-squared residuals after convergence exceeding 0.25 resolution element (in km) for A0.

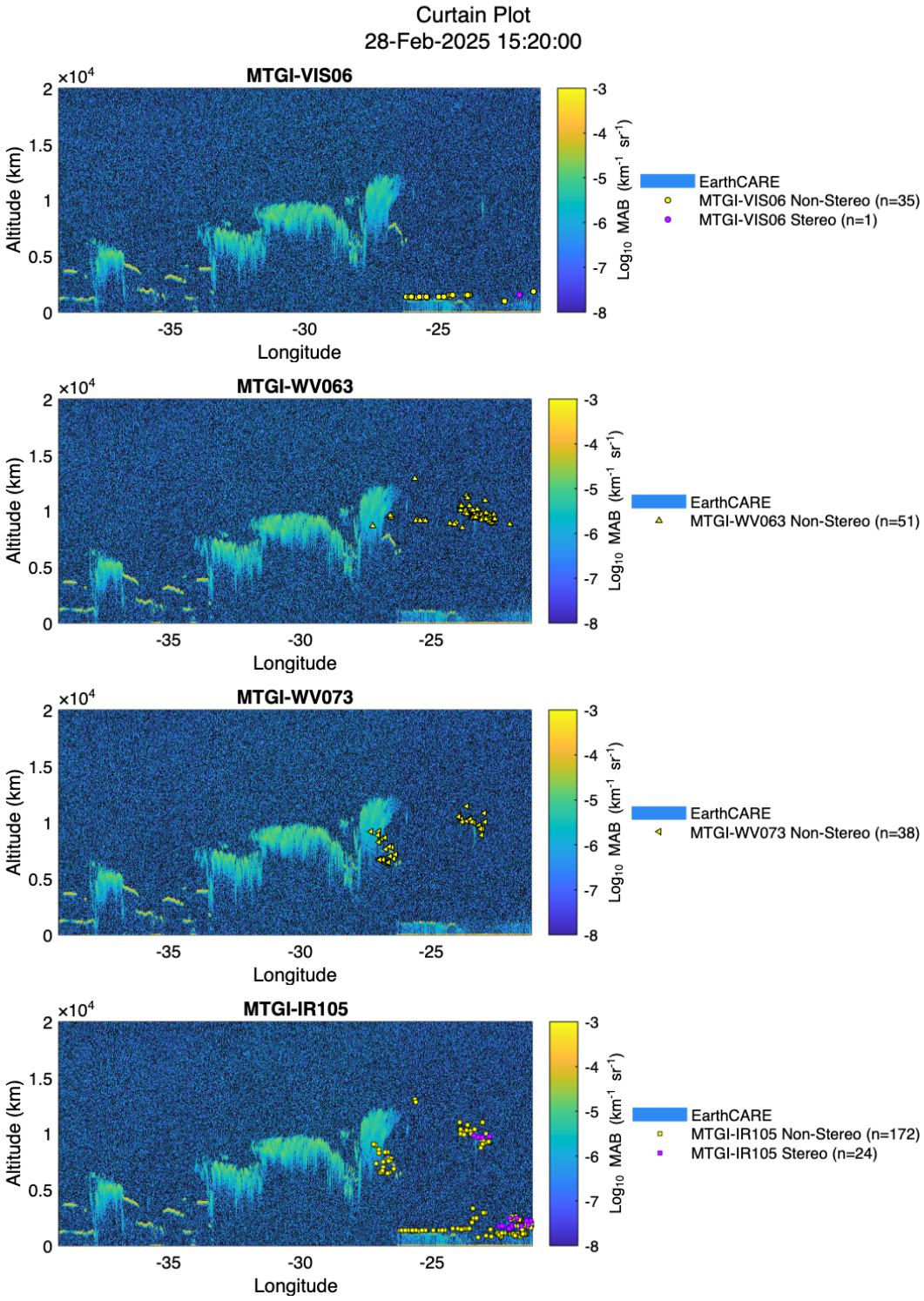
APPENDIX B – EARTHCARE CURTAIN PLOTS

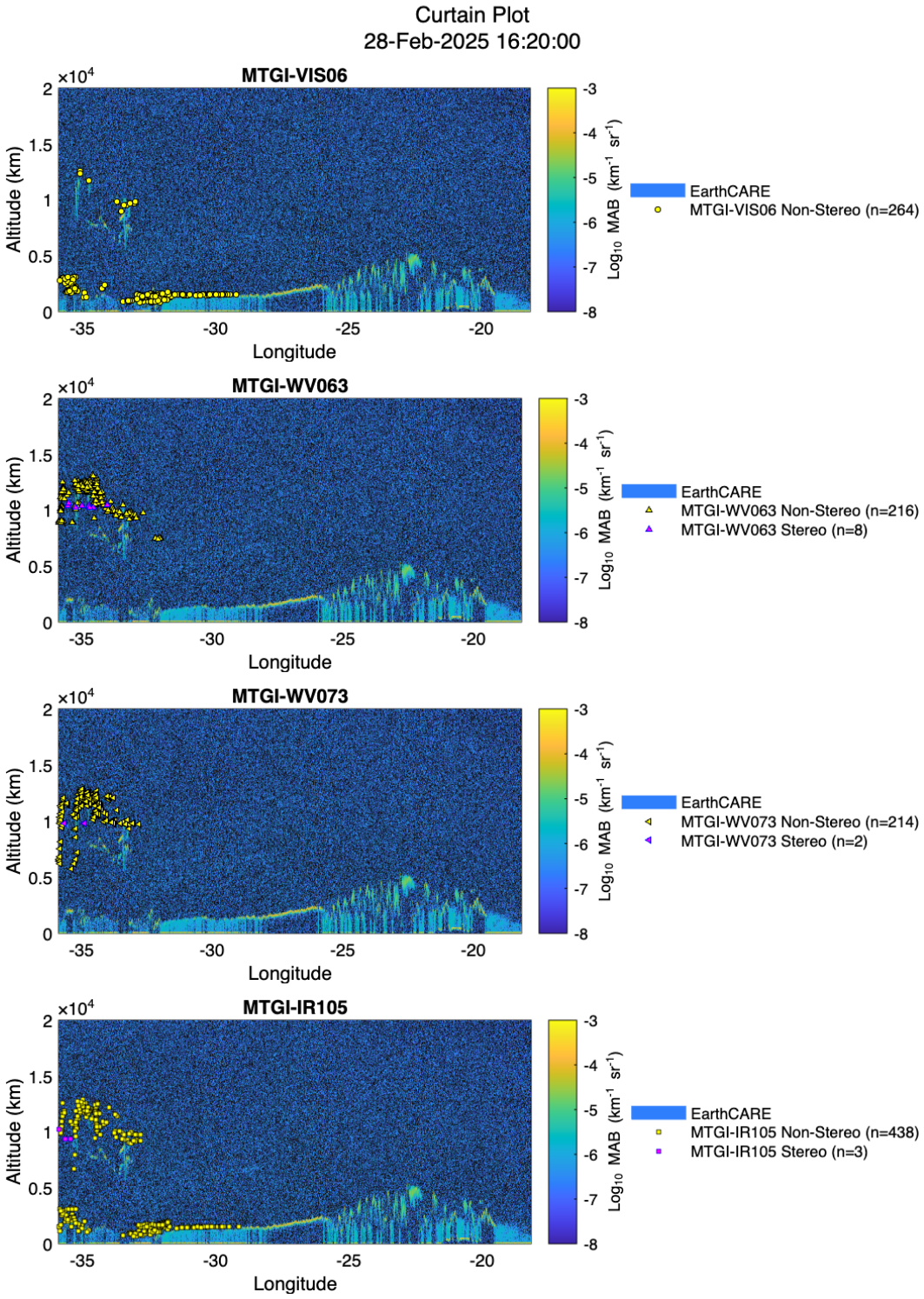
List of timestamps shown:

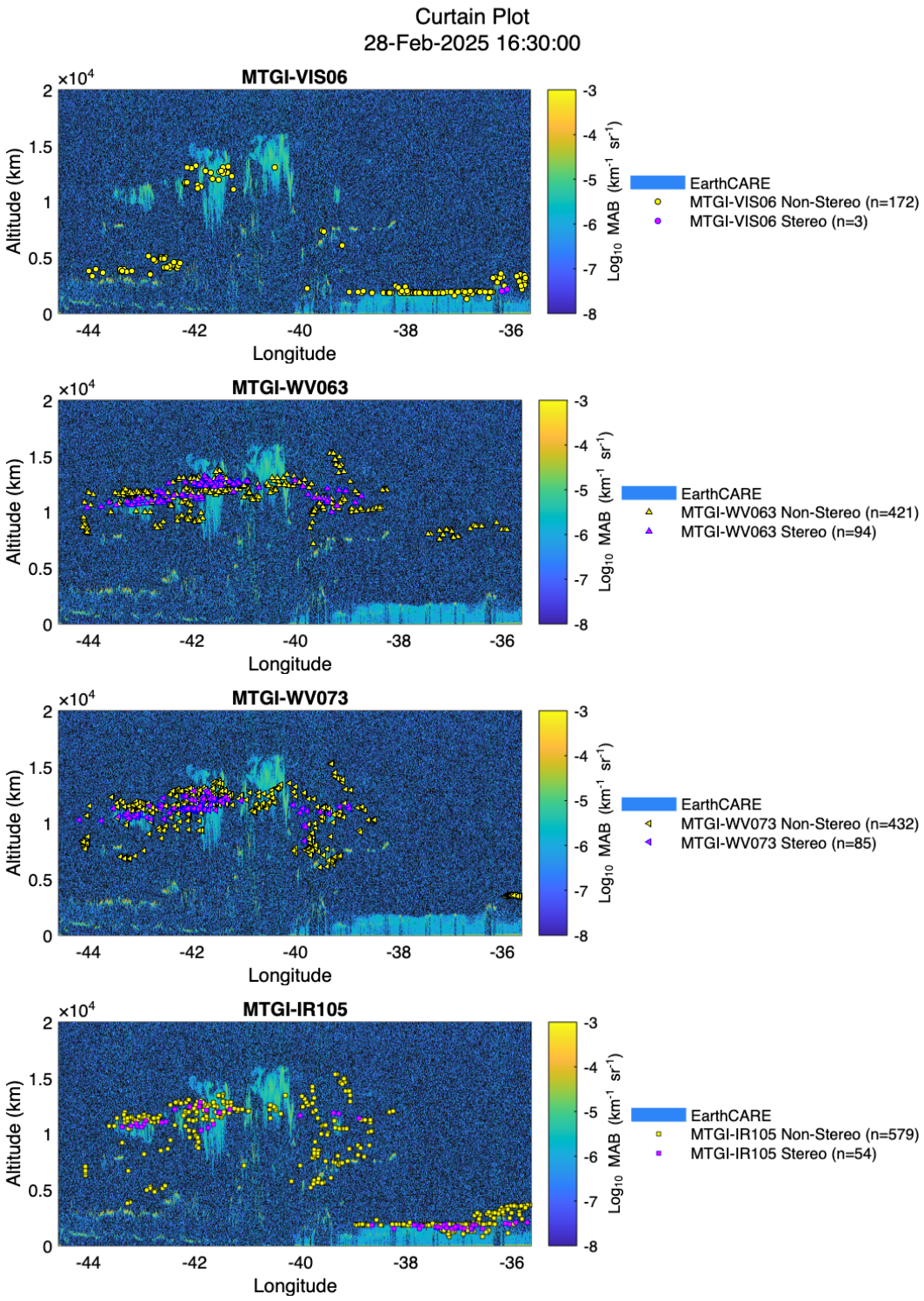
- 20250228T150000
- 20250228T151000
- 20250228T152000
- 20250228T162000
- 20250228T163000
- 20250228T164000
- 20250228T165000
- 20250314T151000
- 20250314T152000
- 20250314T153000
- 20250314T165000
- 20250314T170000
- 20250328T034000
- 20250328T035000
- 20250328T041000
- 20250328T051000
- 20250328T052000
- 20250328T053000
- 20250328T151000
- 20250328T152000
- 20250328T153000
- 20250328T154000
- 20250328T155000
- 20250328T164000
- 20250328T165000
- 20250328T170000
- 20250328T171000
- 20250328T172000

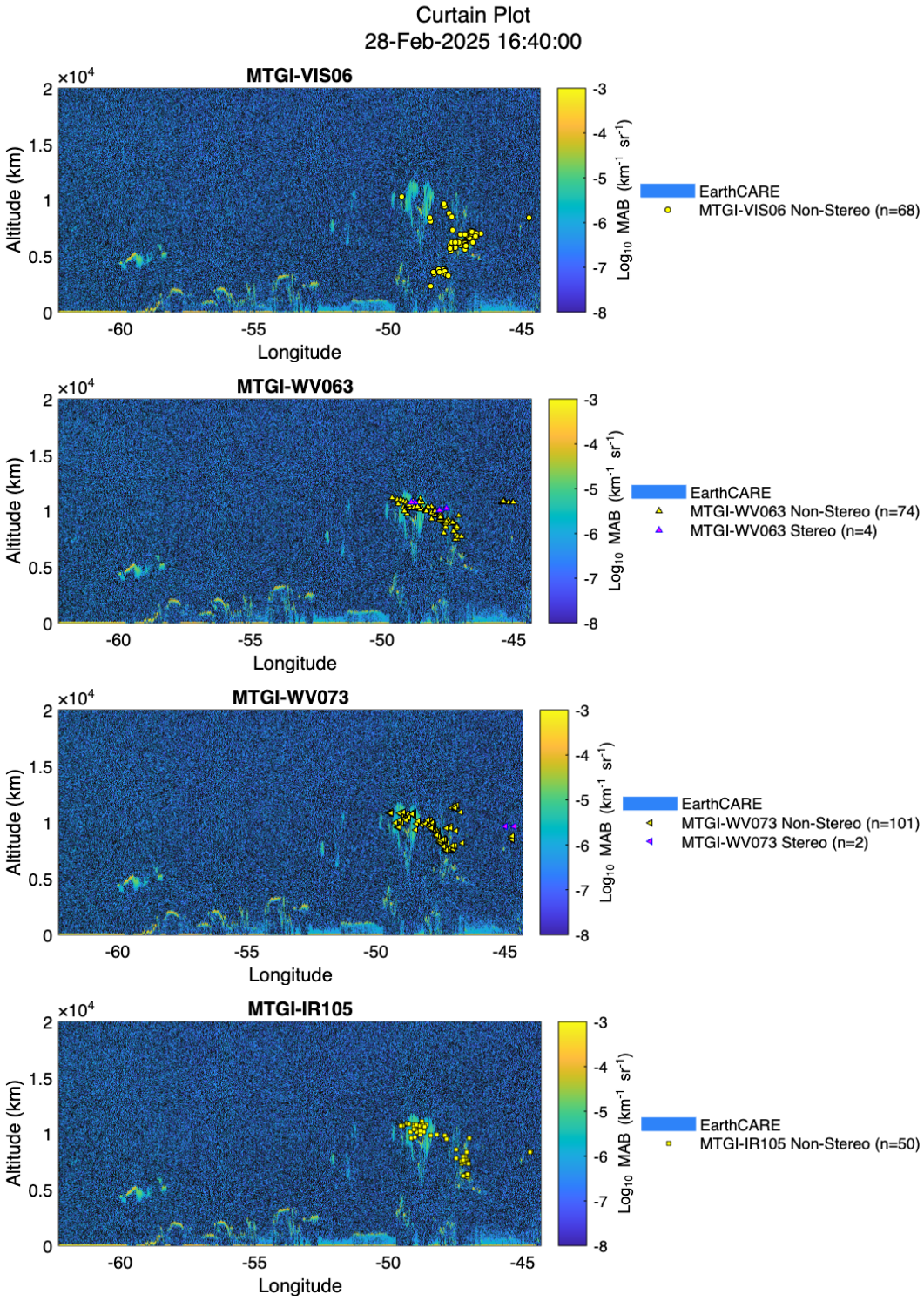

Curtain Plot
28-Feb-2025 15:00:00
MTGI-VIS06
MTGI-WV063
MTGI-WV073
MTGI-IR105
×10^4
Altitude (km)
Longitude
Log10 MAB (km-1 sr-1)
EarthCARE
MTGI-VIS06 Non-Stereo (n=90)
MTGI-VIS06 Stereo (n=8)
MTGI-WV063 Non-Stereo (n=108)
MTGI-WV063 Stereo (n=18)
MTGI-WV073 Non-Stereo (n=45)
MTGI-WV073 Stereo (n=5)
MTGI-IR105 Non-Stereo (n=422)
MTGI-IR105 Stereo (n=73)

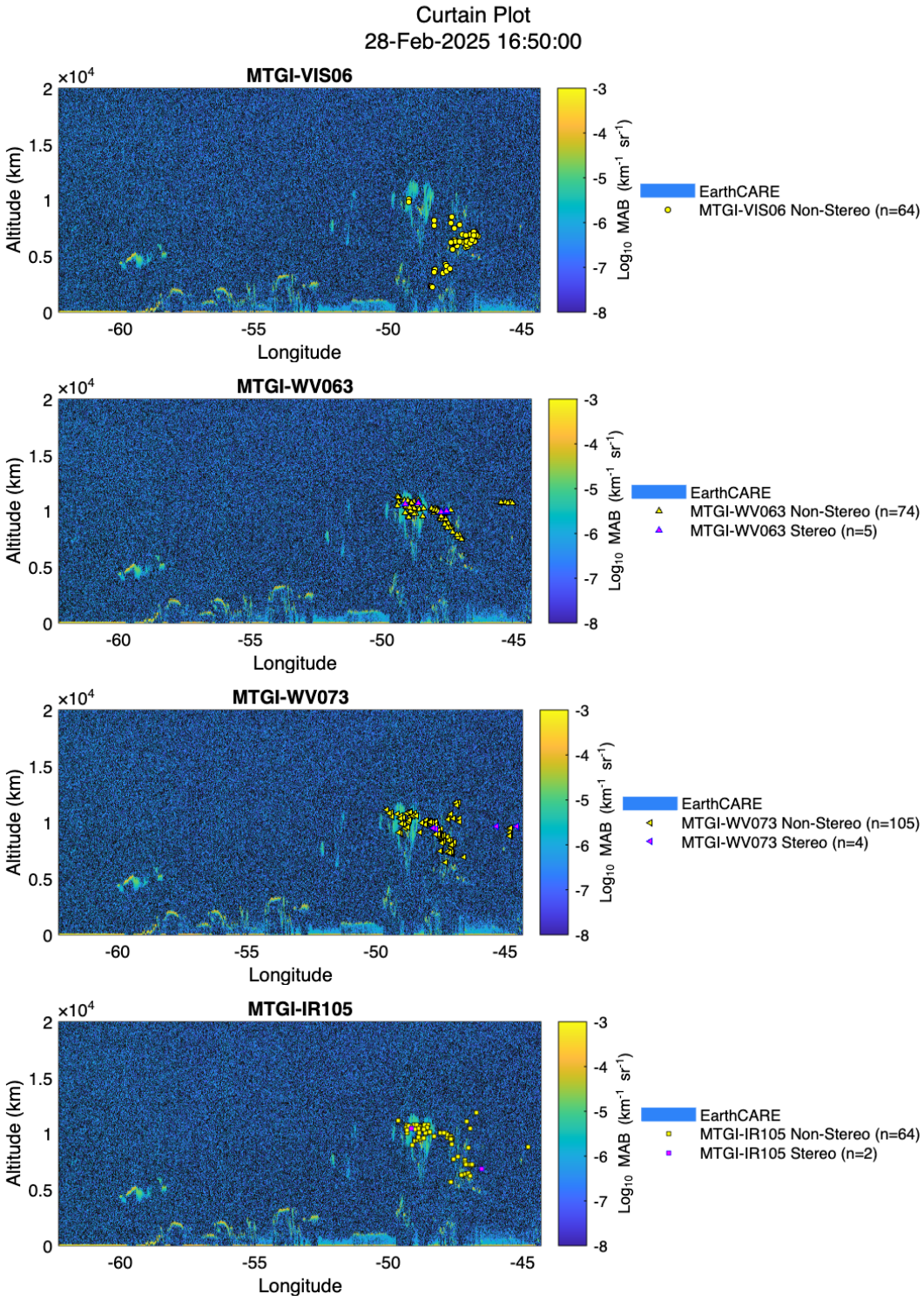

Curtain Plot
28-Feb-2025 15:10:00
MTGI-VIS06
MTGI-WV063
MTGI-WV073
MTGI-IR105
×10^4
Altitude (km)
Longitude
Log10 MAB (km-1 sr-1)
EarthCARE
MTGI-VIS06 Non-Stereo (n=35)
MTGI-VIS06 Stereo (n=1)
MTGI-WV063 Non-Stereo (n=61)
MTGI-WV073 Non-Stereo (n=32)
MTGI-IR105 Non-Stereo (n=137)
MTGI-IR105 Stereo (n=20)

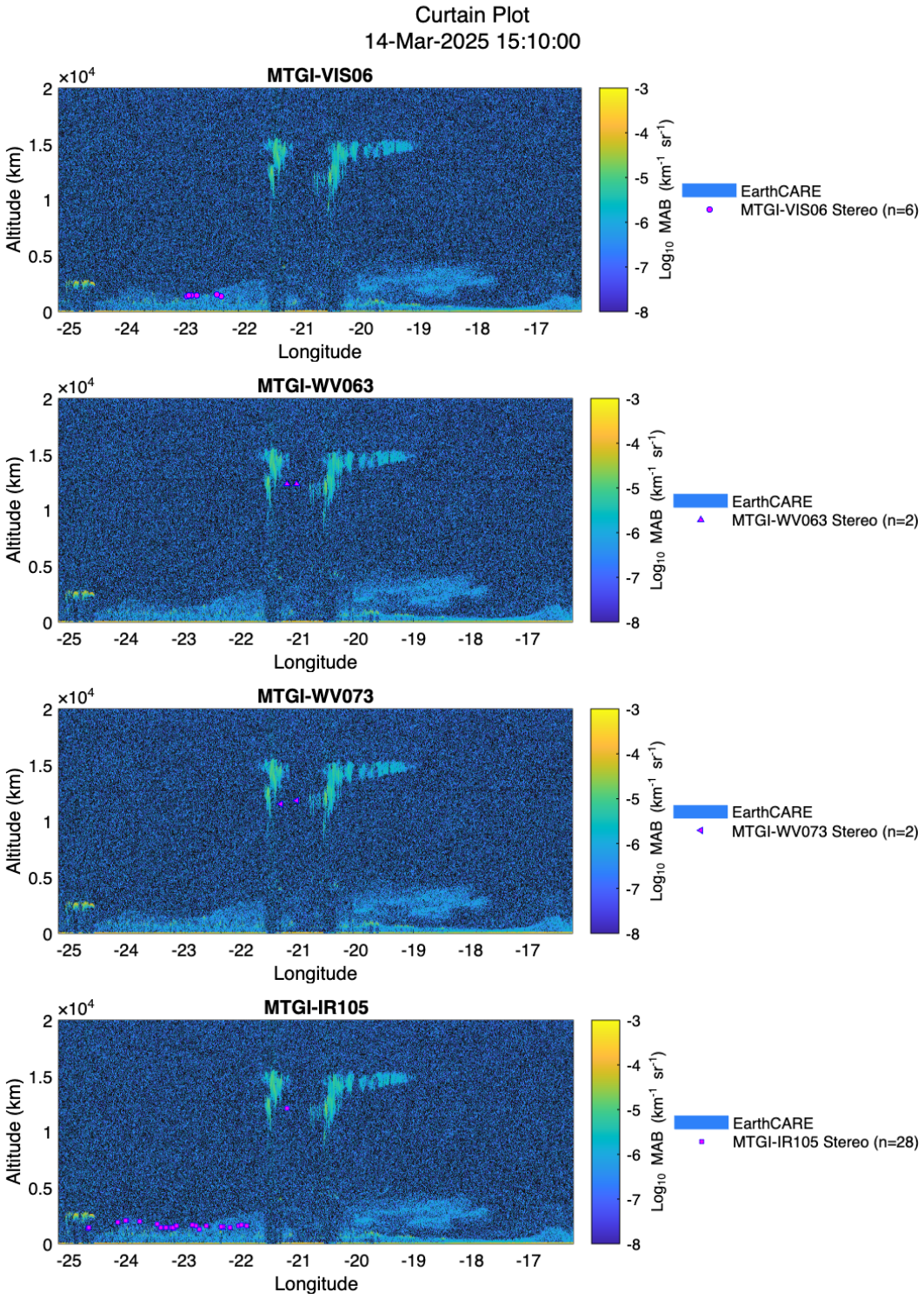

Curtain Plot
28-Feb-2025 15:20:00
MTGI-VIS06
MTGI-WV063
MTGI-WV073
MTGI-IR105
×10^4
Altitude (km)
Longitude
Log10 MAB (km-1 sr-1)
EarthCARE
MTGI-VIS06 Non-Stereo (n=35)
MTGI-VIS06 Stereo (n=1)
MTGI-WV063 Non-Stereo (n=51)
MTGI-WV073 Non-Stereo (n=38)
MTGI-IR105 Non-Stereo (n=172)
MTGI-IR105 Stereo (n=24)

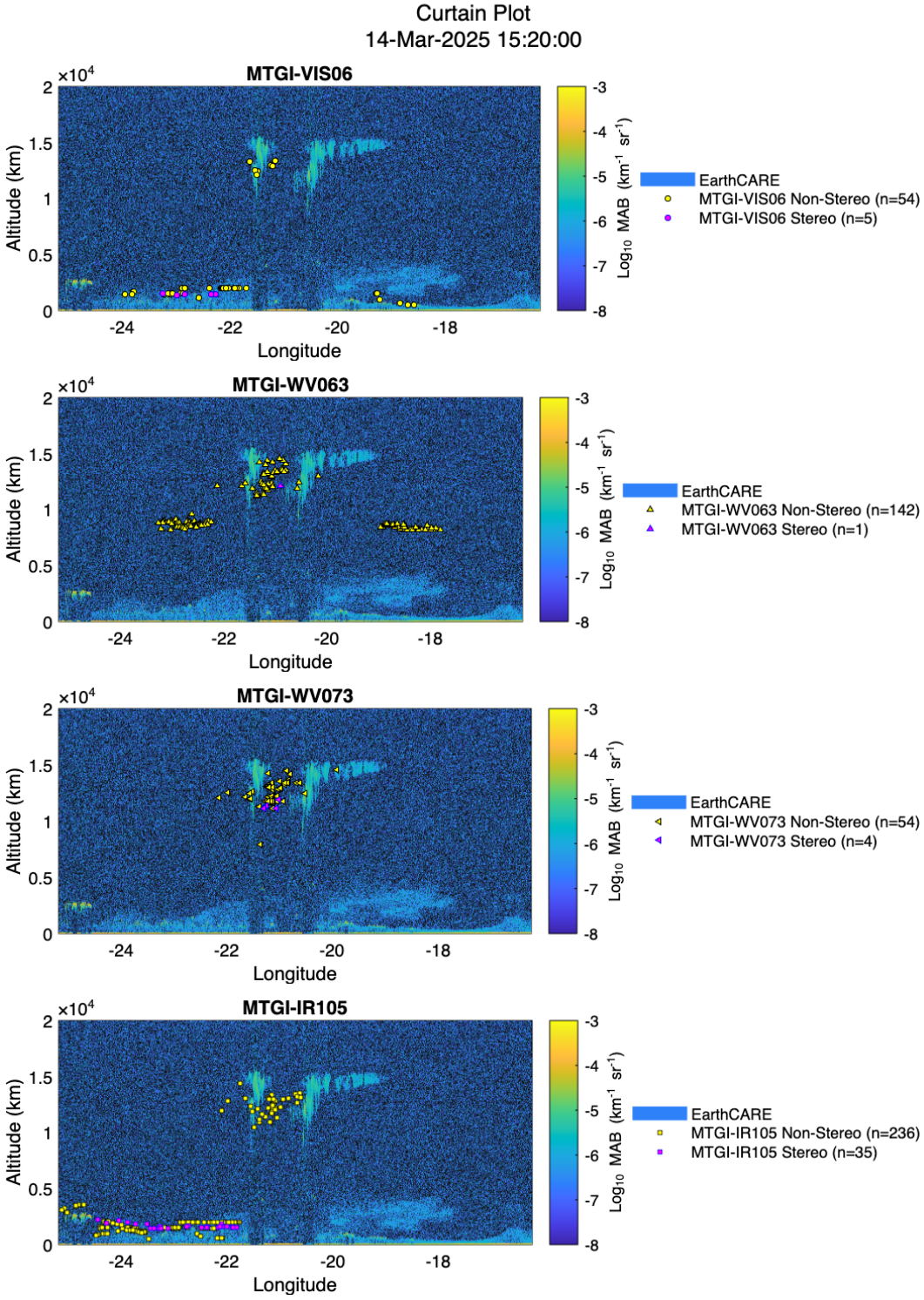

Curtain Plot
28-Feb-2025 16:20:00
MTGI-VIS06
MTGI-WV063
MTGI-WV073
MTGI-IR105
×10^4
Altitude (km)
Longitude
Log10 MAB (km-1 sr-1)
EarthCARE
MTGI-VIS06 Non-Stereo (n=264)
MTGI-WV063 Non-Stereo (n=216)
MTGI-WV063 Stereo (n=8)
MTGI-WV073 Non-Stereo (n=214)
MTGI-WV073 Stereo (n=2)
MTGI-IR105 Non-Stereo (n=438)
MTGI-IR105 Stereo (n=3)

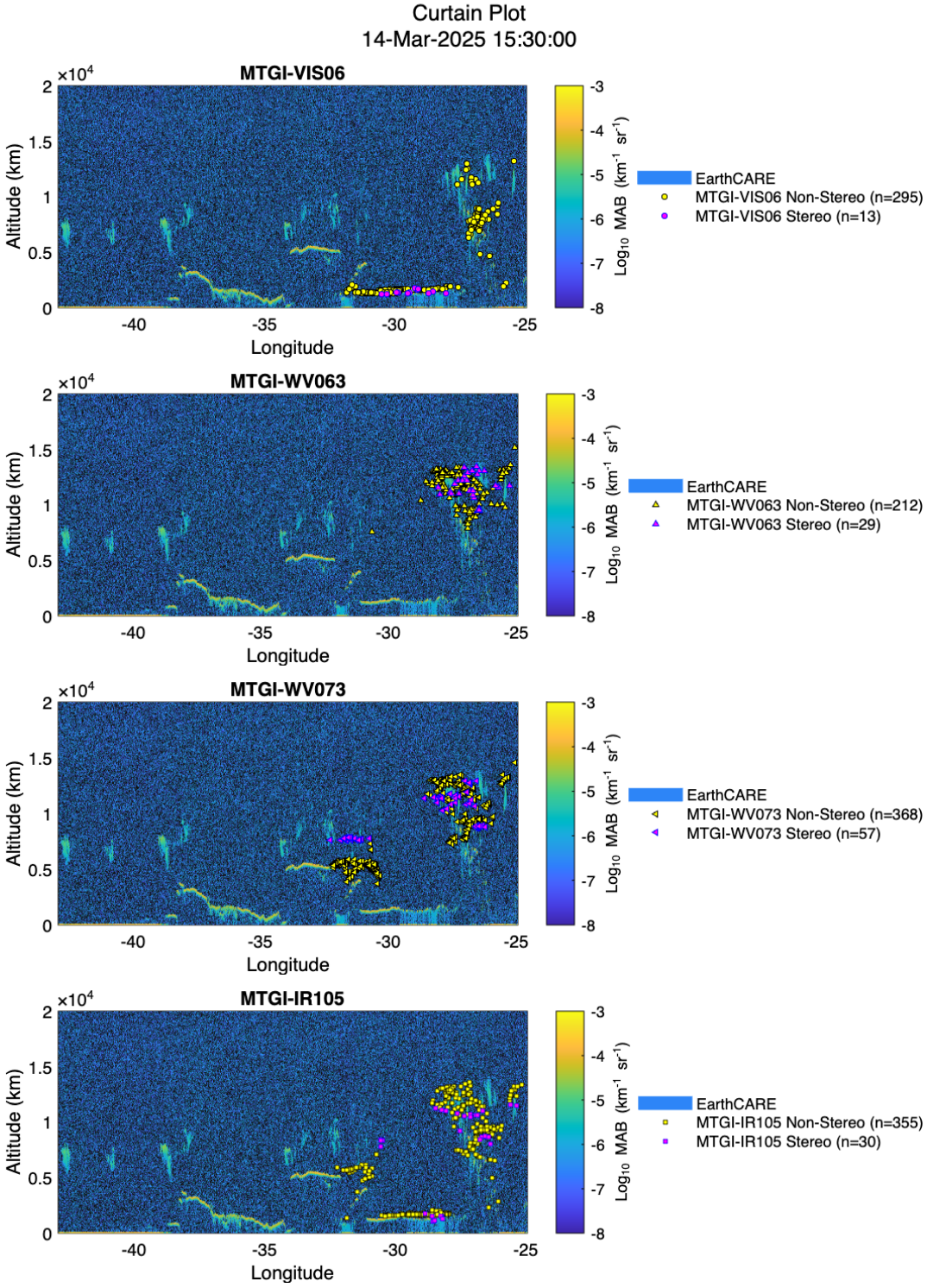

Curtain Plot
28-Feb-2025 16:30:00
MTGI-VIS06
MTGI-WV063
MTGI-WV073
MTGI-IR105
×10^4
Altitude (km)
Longitude
Log10 MAB (km-1 sr-1)
EarthCARE
MTGI-VIS06 Non-Stereo (n=172)
MTGI-VIS06 Stereo (n=3)
MTGI-WV063 Non-Stereo (n=421)
MTGI-WV063 Stereo (n=94)
MTGI-WV073 Non-Stereo (n=432)
MTGI-WV073 Stereo (n=85)
MTGI-IR105 Non-Stereo (n=579)
MTGI-IR105 Stereo (n=54)

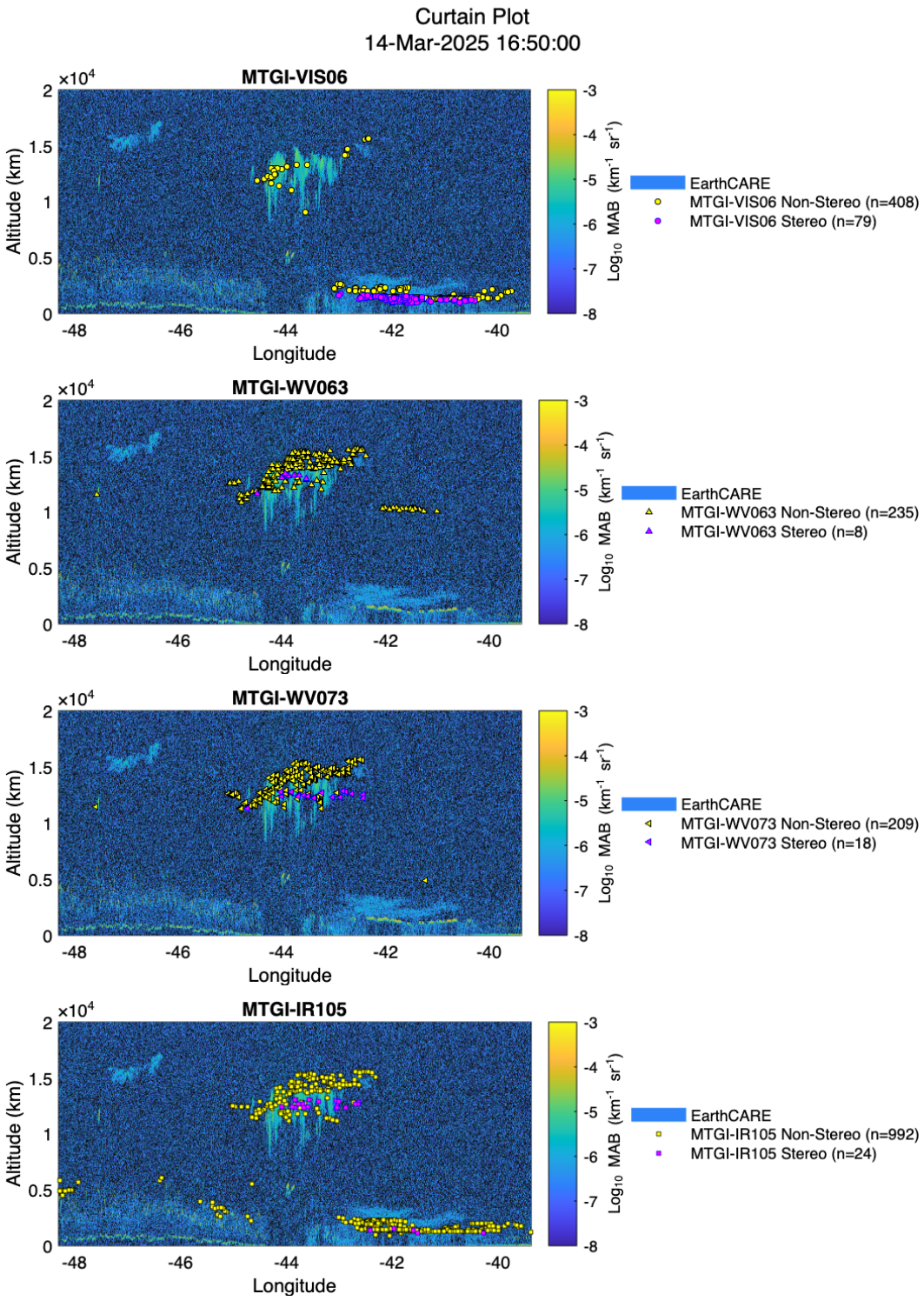

Curtain Plot
28-Feb-2025 16:40:00
MTGI-VIS06
MTGI-WV063
MTGI-WV073
MTGI-IR105
×10^4
Altitude (km)
Longitude
Log10 MAB (km-1 sr-1)
EarthCARE
MTGI-VIS06 Non-Stereo (n=68)
MTGI-WV063 Non-Stereo (n=74)
MTGI-WV063 Stereo (n=4)
MTGI-WV073 Non-Stereo (n=101)
MTGI-WV073 Stereo (n=2)
MTGI-IR105 Non-Stereo (n=50)

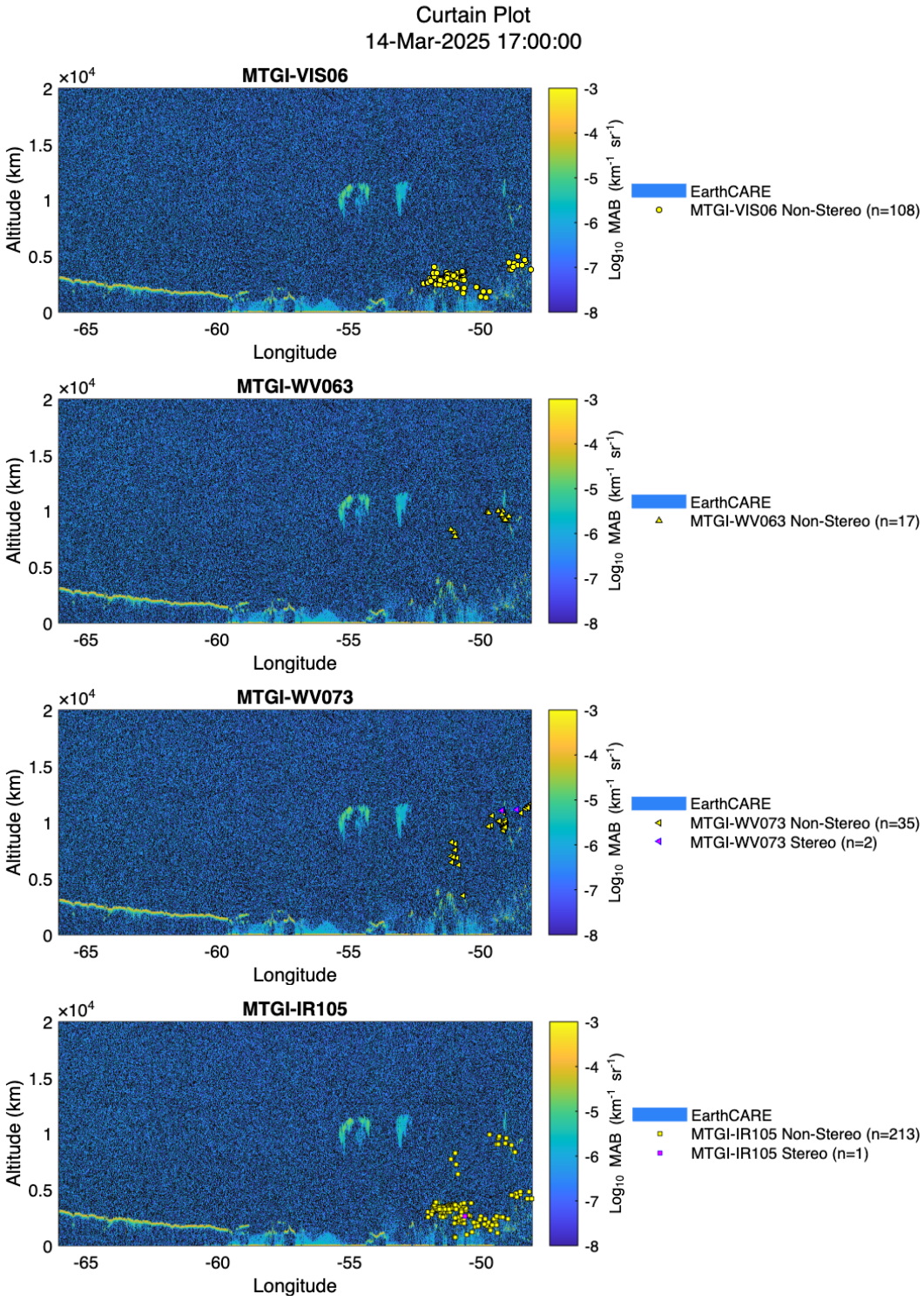

Curtain Plot
28-Feb-2025 16:50:00
MTGI-VIS06
MTGI-WV063
MTGI-WV073
MTGI-IR105
×10^4
Altitude (km)
Longitude
Log10 MAB (km-1 sr-1)
EarthCARE
MTGI-VIS06 Non-Stereo (n=64)
MTGI-WV063 Non-Stereo (n=74)
MTGI-WV063 Stereo (n=5)
MTGI-WV073 Non-Stereo (n=105)
MTGI-WV073 Stereo (n=4)
MTGI-IR105 Non-Stereo (n=64)
MTGI-IR105 Stereo (n=2)

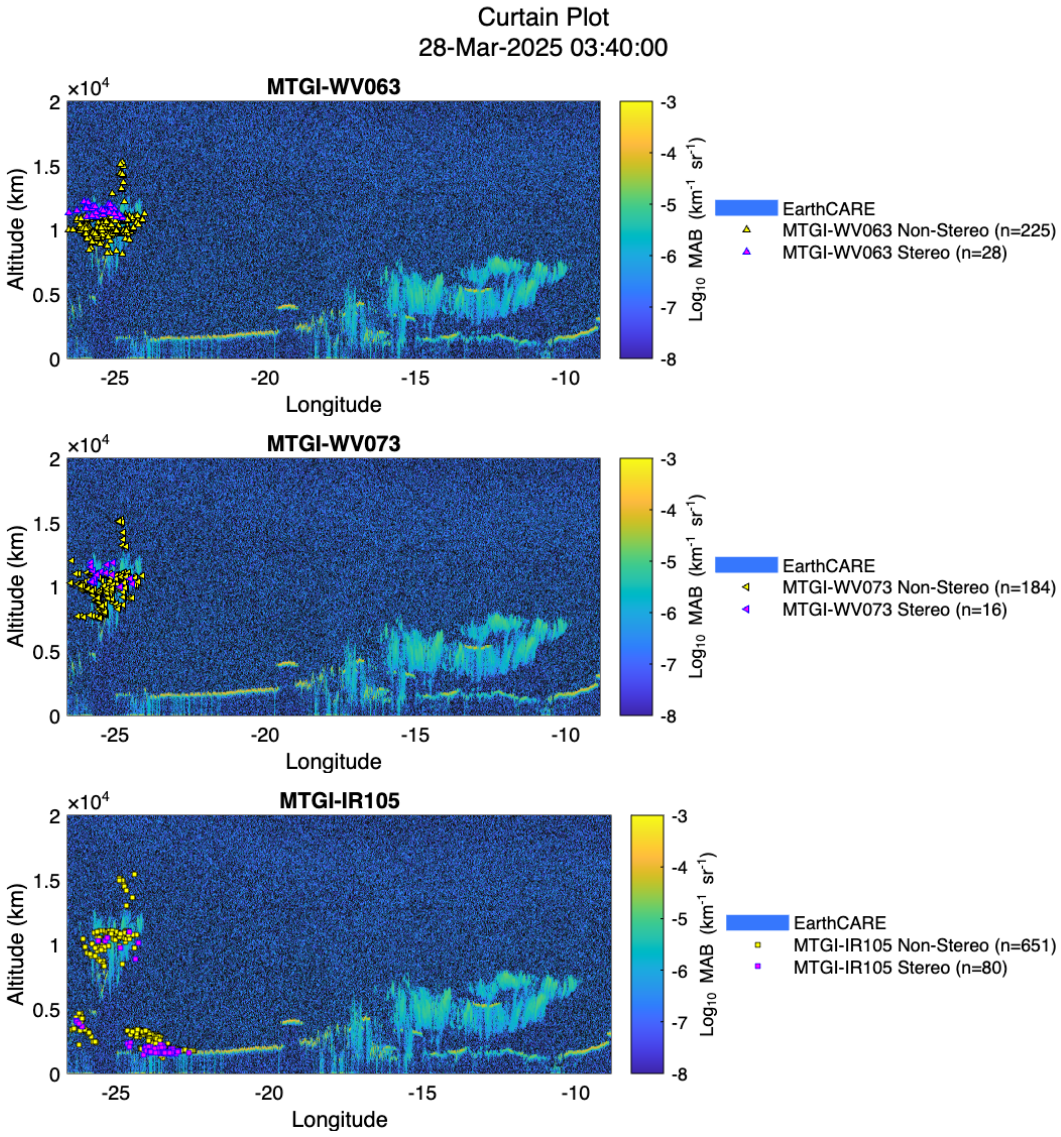

Curtain Plot
14-Mar-2025 15:10:00
MTGI-VIS06
MTGI-WV063
MTGI-WV073
MTGI-IR105
×10^4
Altitude (km)
Longitude
Log10 MAB (km-1 sr-1)
EarthCARE
MTGI-VIS06 Stereo (n=6)
MTGI-WV063 Stereo (n=2)
MTGI-WV073 Stereo (n=2)
MTGI-IR105 Stereo (n=28)

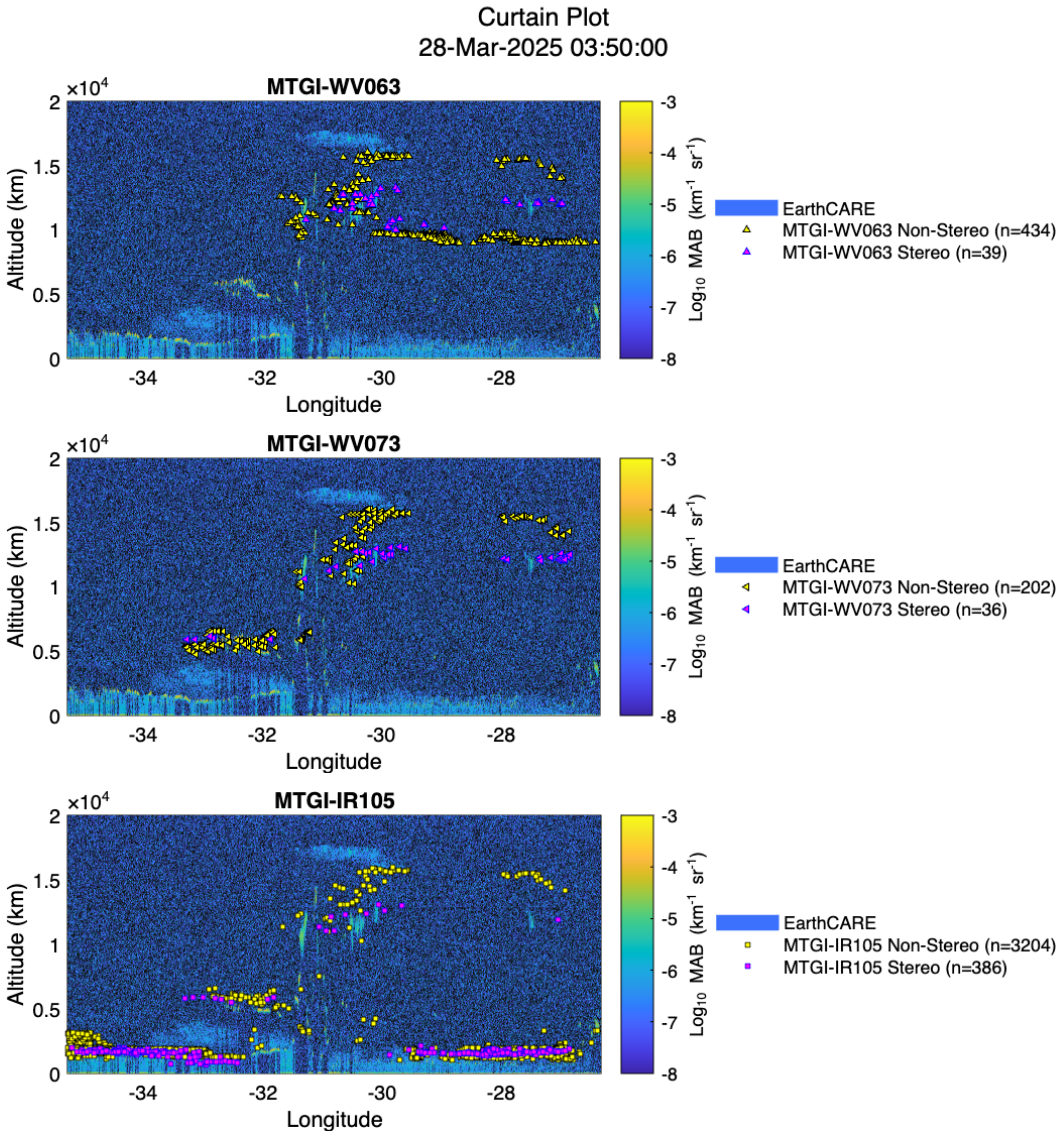

Curtain Plot
14-Mar-2025 15:20:00
MTGI-VIS06
MTGI-WV063
MTGI-WV073
MTGI-IR105
Altitude (km)
Longitude
Log10 MAB (km-1 sr-1)
EarthCARE
MTGI-VIS06 Non-Stereo (n=54)
MTGI-VIS06 Stereo (n=5)
MTGI-WV063 Non-Stereo (n=142)
MTGI-WV063 Stereo (n=1)
MTGI-WV073 Non-Stereo (n=54)
MTGI-WV073 Stereo (n=4)
MTGI-IR105 Non-Stereo (n=236)
MTGI-IR105 Stereo (n=35)

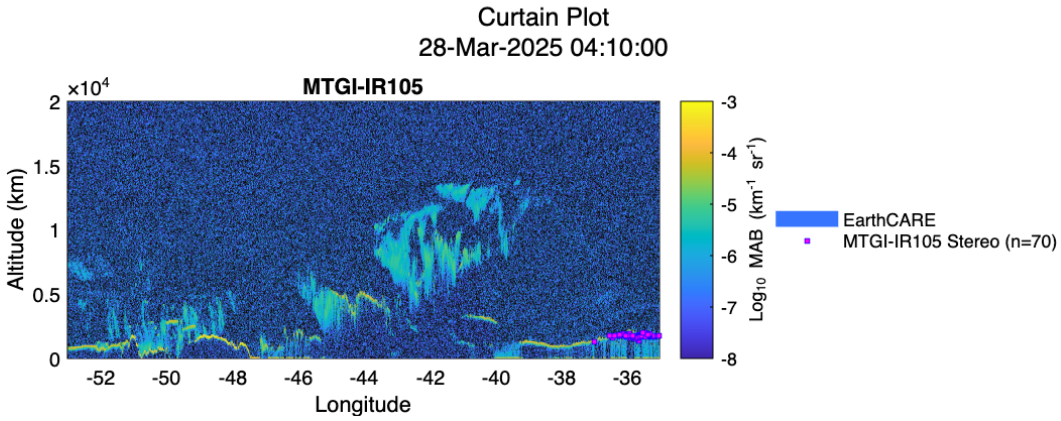

Curtain Plot
14-Mar-2025 15:30:00
MTGI-VIS06
MTGI-WV063
MTGI-WV073
MTGI-IR105
×10^4
Altitude (km)
Longitude
Log10 MAB (km-1 sr-1)
EarthCARE
MTGI-VIS06 Non-Stereo (n=295)
MTGI-VIS06 Stereo (n=13)
MTGI-WV063 Non-Stereo (n=212)
MTGI-WV063 Stereo (n=29)
MTGI-WV073 Non-Stereo (n=368)
MTGI-WV073 Stereo (n=57)
MTGI-IR105 Non-Stereo (n=355)
MTGI-IR105 Stereo (n=30)

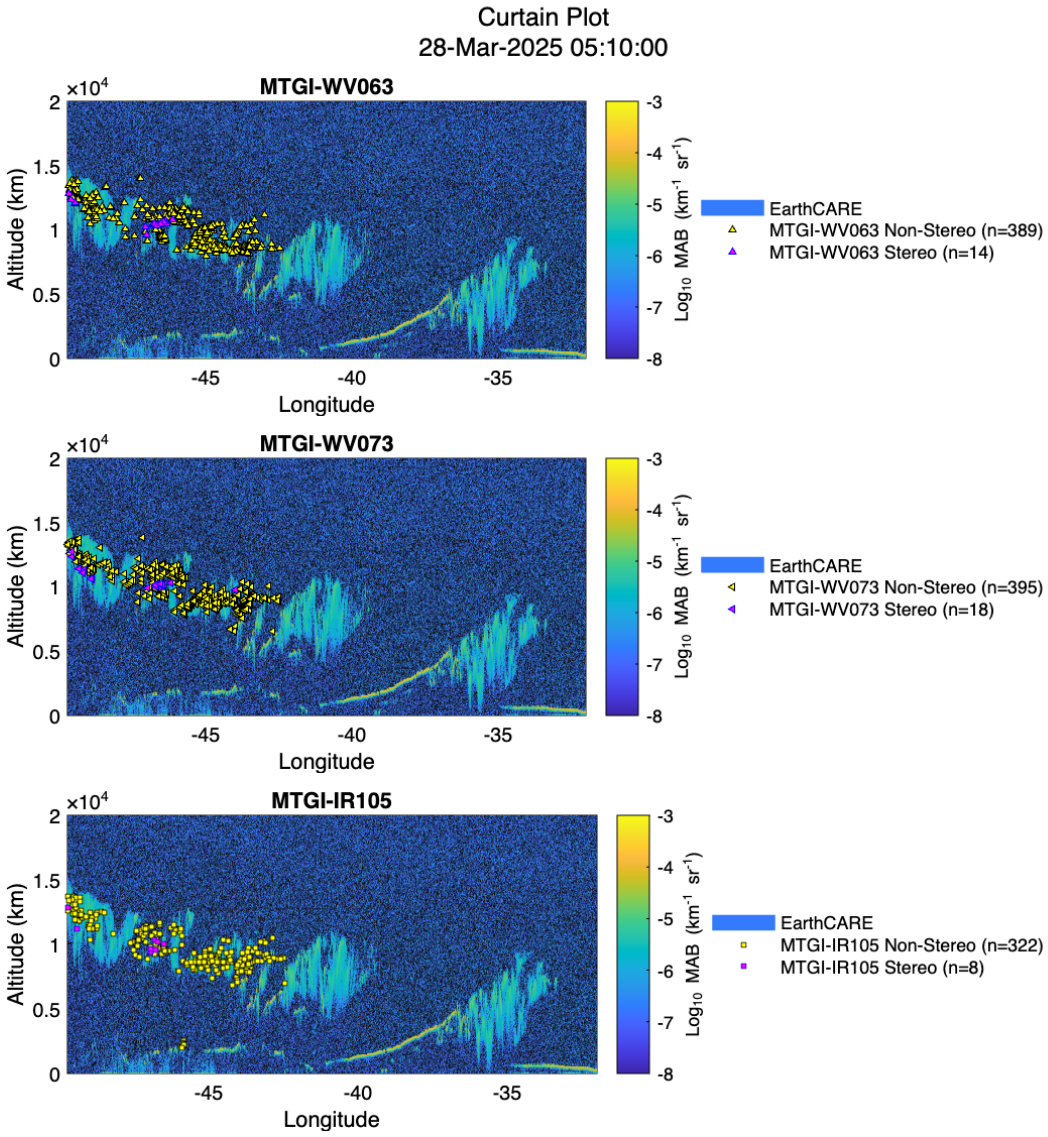

Curtain Plot
14-Mar-2025 16:50:00
MTGI-VIS06
MTGI-WV063
MTGI-WV073
MTGI-IR105
Altitude (km)
Longitude
Log10 MAB (km-1 sr-1)
EarthCARE
MTGI-VIS06 Non-Stereo (n=408)
MTGI-VIS06 Stereo (n=79)
MTGI-WV063 Non-Stereo (n=235)
MTGI-WV063 Stereo (n=8)
MTGI-WV073 Non-Stereo (n=209)
MTGI-WV073 Stereo (n=18)
MTGI-IR105 Non-Stereo (n=992)
MTGI-IR105 Stereo (n=24)

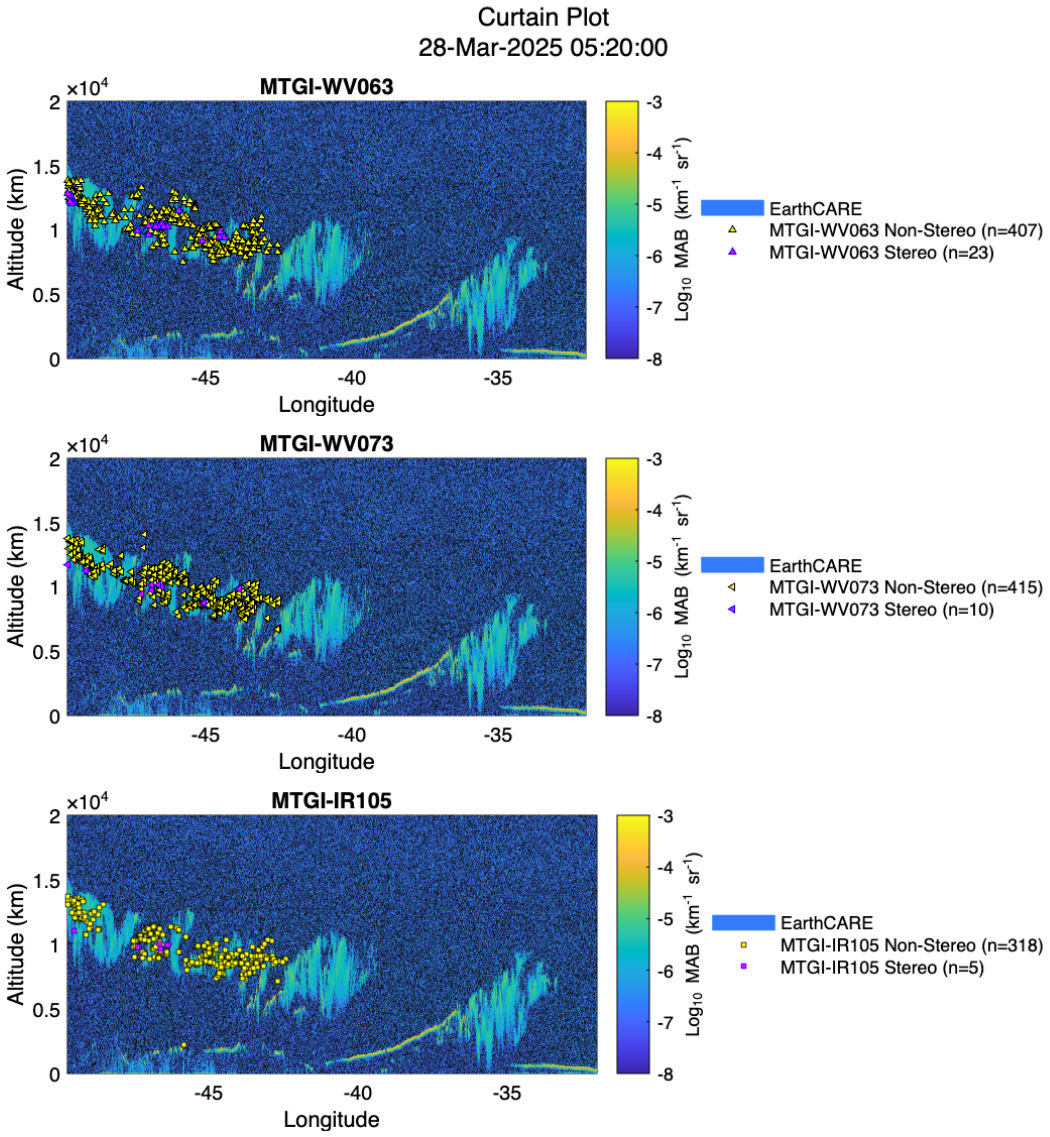

Curtain Plot
14-Mar-2025 17:00:00
MTGI-VIS06
MTGI-WV063
MTGI-WV073
MTGI-IR105
×10^4
Altitude (km)
Longitude
Log10 MAB (km-1 sr-1)
EarthCARE
MTGI-VIS06 Non-Stereo (n=108)
MTGI-WV063 Non-Stereo (n=17)
MTGI-WV073 Non-Stereo (n=35)
MTGI-WV073 Stereo (n=2)
MTGI-IR105 Non-Stereo (n=213)
MTGI-IR105 Stereo (n=1)

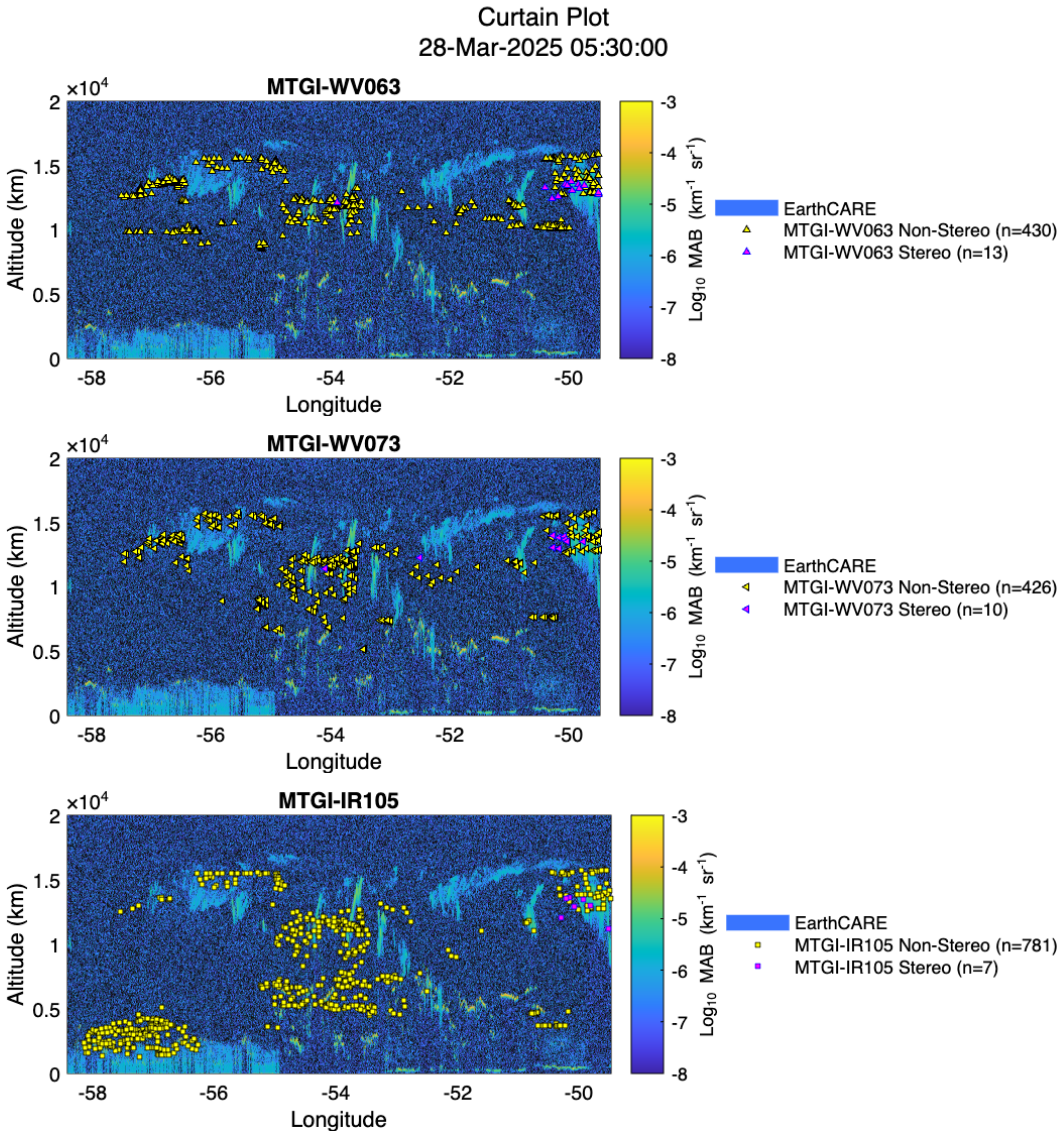

Curtain Plot
28-Mar-2025 03:40:00
MTGI-WV063
MTGI-WV073
MTGI-IR105
×10^4
Altitude (km)
Longitude
Log10 MAB (km-1 sr-1)
EarthCARE
MTGI-WV063 Non-Stereo (n=225)
MTGI-WV063 Stereo (n=28)
MTGI-WV073 Non-Stereo (n=184)
MTGI-WV073 Stereo (n=16)
MTGI-IR105 Non-Stereo (n=651)
MTGI-IR105 Stereo (n=80)

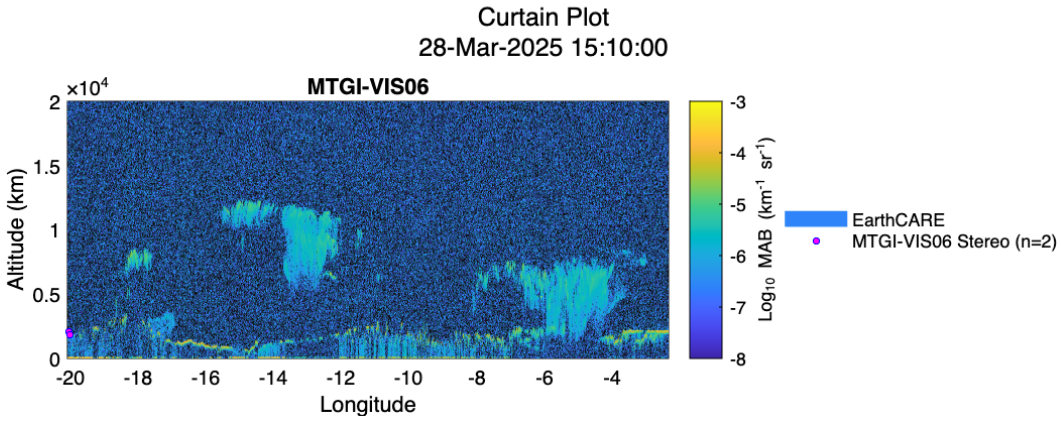

Curtain Plot
28-Mar-2025 03:50:00
MTGI-WV063
MTGI-WV073
MTGI-IR105
Altitude (km)
×10^4
Longitude
-34
-32
-30
-28
Log10 MAB (km-1 sr-1)
EarthCARE
MTGI-WV063 Non-Stereo (n=434)
MTGI-WV063 Stereo (n=39)
MTGI-WV073 Non-Stereo (n=202)
MTGI-WV073 Stereo (n=36)
MTGI-IR105 Non-Stereo (n=3204)
MTGI-IR105 Stereo (n=386)

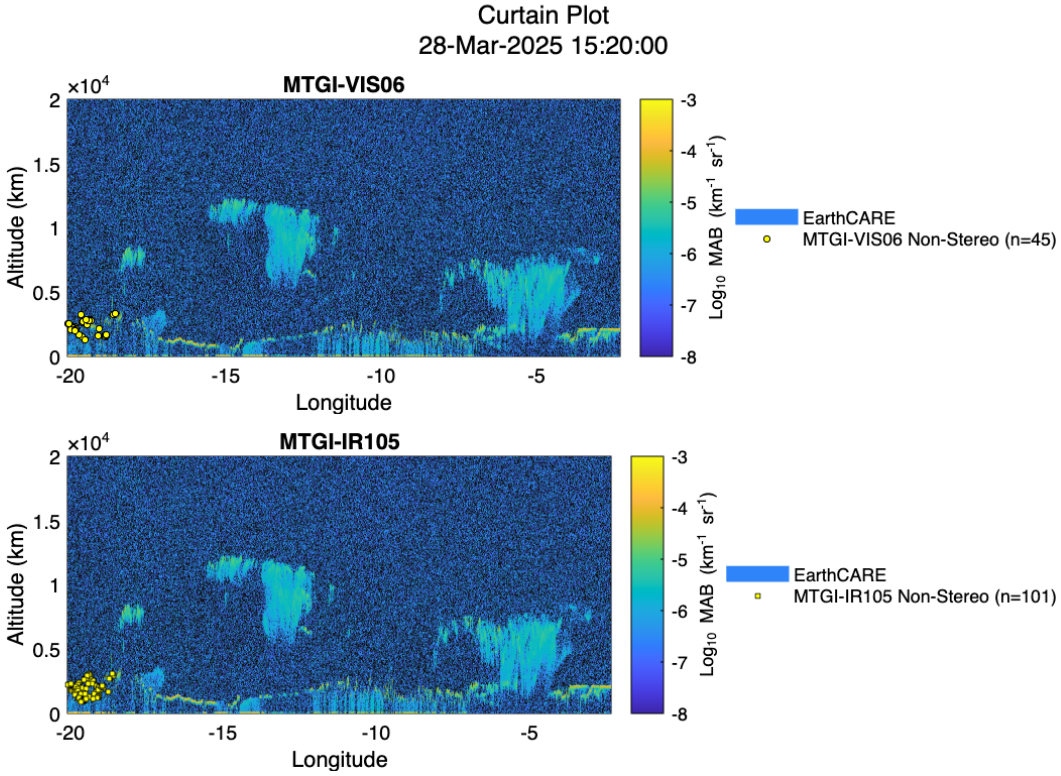

Curtain Plot
28-Mar-2025 04:10:00
MTGI-IR105
×10^4
2
1.5
1
0.5
0
Altitude (km)
-52
-50
-48
-46
-44
-42
-40
-38
-36
Longitude
-3
-4
-5
-6
-7
-8
Log10 MAB (km-1 sr-1)
EarthCARE
MTGI-IR105 Stereo (n=70)

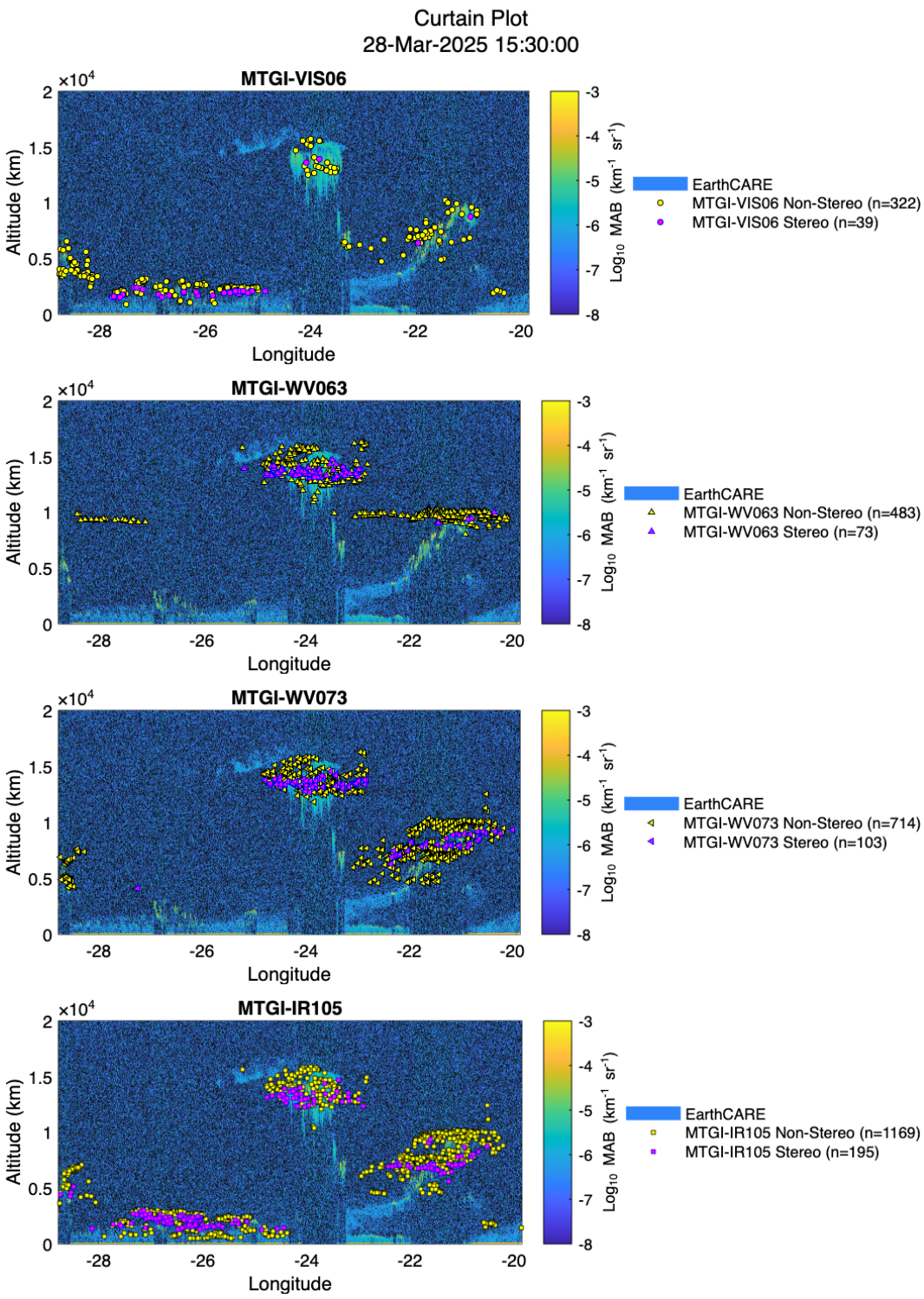

Curtain Plot
28-Mar-2025 05:10:00
MTGI-WV063
MTGI-WV073
MTGI-IR105
Altitude (km)
Longitude
Log10 MAB (km-1 sr-1)
EarthCARE
MTGI-WV063 Non-Stereo (n=389)
MTGI-WV063 Stereo (n=14)
MTGI-WV073 Non-Stereo (n=395)
MTGI-WV073 Stereo (n=18)
MTGI-IR105 Non-Stereo (n=322)
MTGI-IR105 Stereo (n=8)

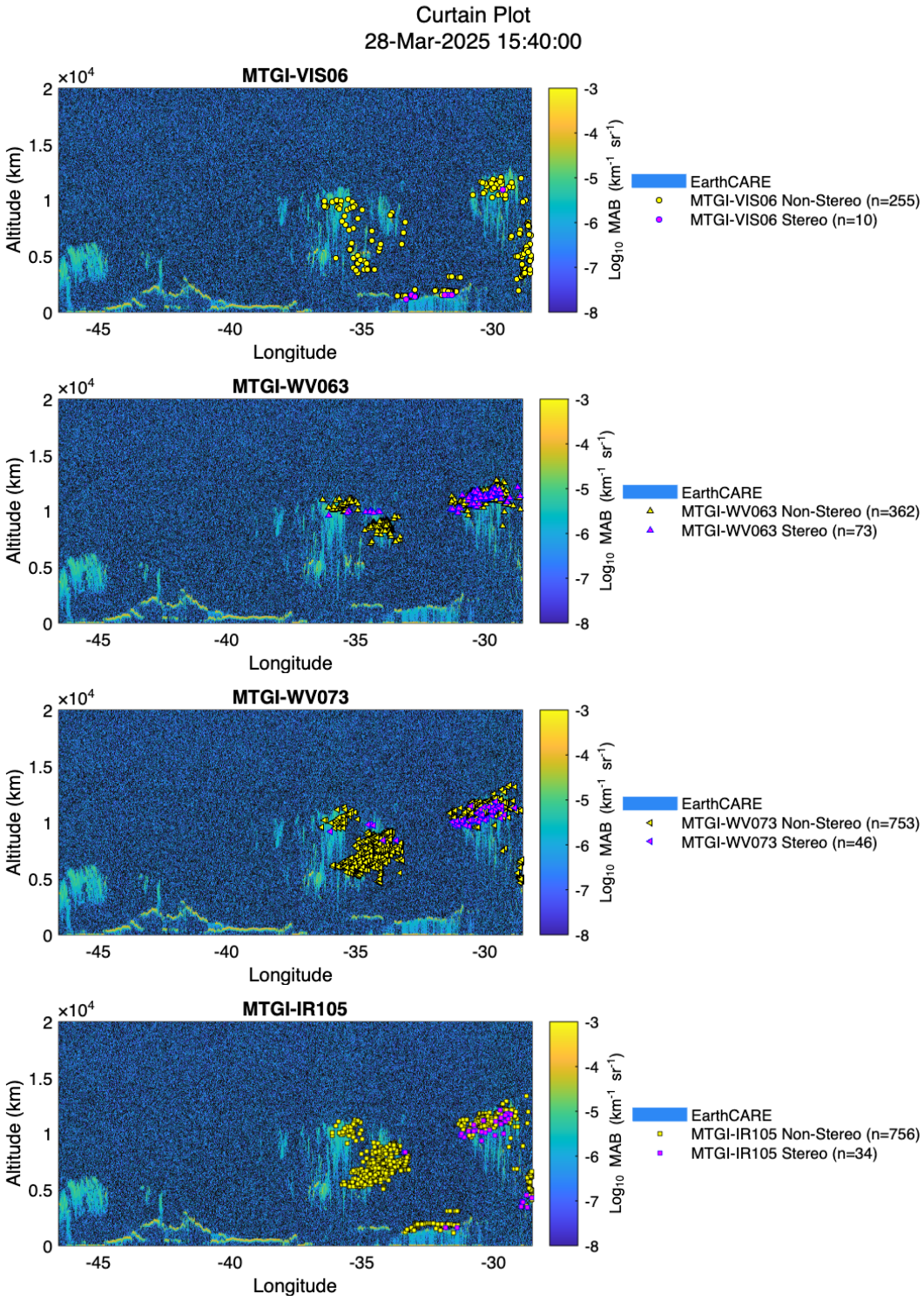

Curtain Plot
28-Mar-2025 05:20:00
MTGI-WV063
MTGI-WV073
MTGI-IR105
Altitude (km)
Longitude
Log10 MAB (km-1 sr-1)
EarthCARE
MTGI-WV063 Non-Stereo (n=407)
MTGI-WV063 Stereo (n=23)
MTGI-WV073 Non-Stereo (n=415)
MTGI-WV073 Stereo (n=10)
MTGI-IR105 Non-Stereo (n=318)
MTGI-IR105 Stereo (n=5)

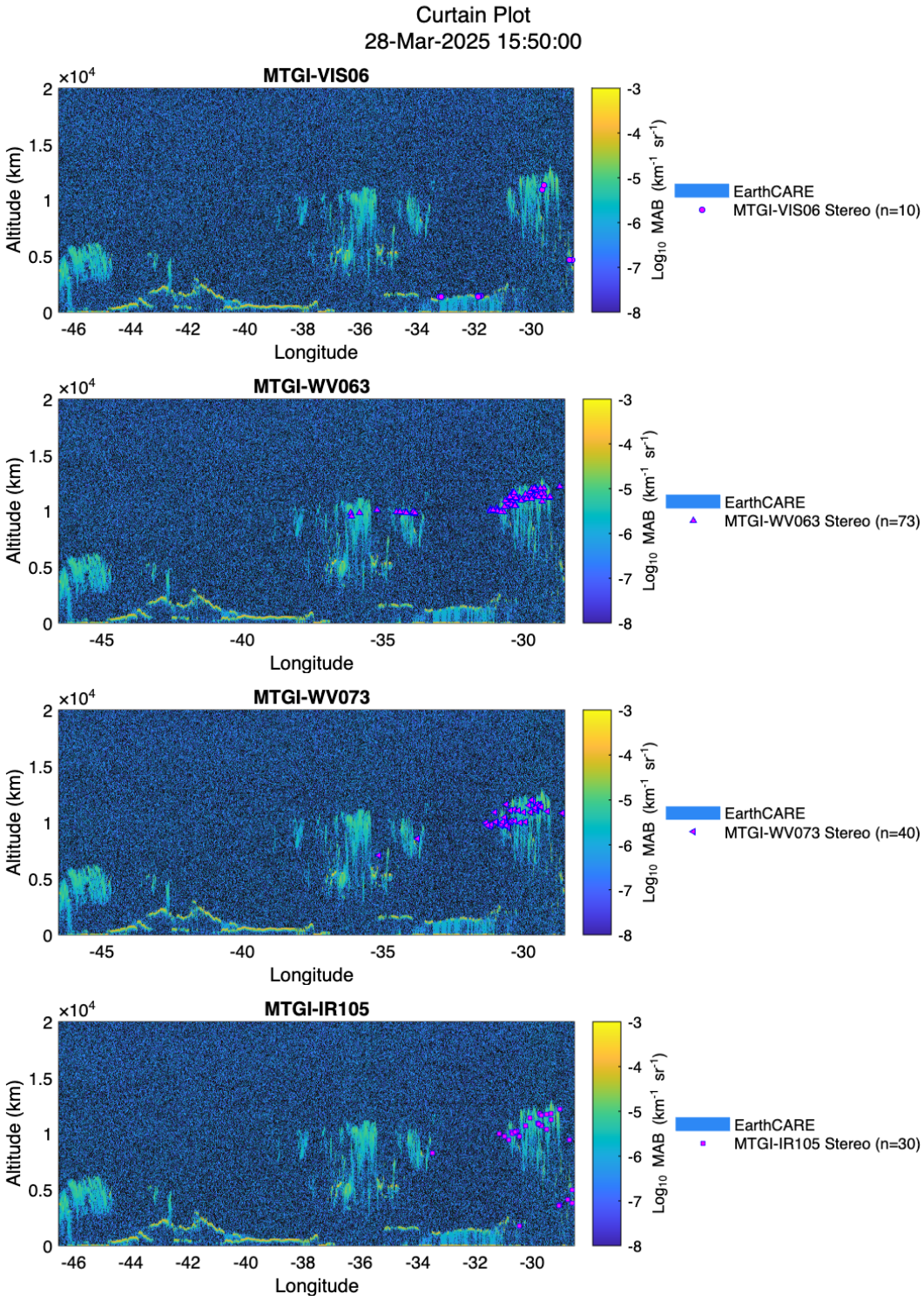

Curtain Plot
28-Mar-2025 05:30:00
MTGI-WV063
MTGI-WV073
MTGI-IR105
Altitude (km)
Longitude
Log10 MAB (km-1 sr-1)
EarthCARE
MTGI-WV063 Non-Stereo (n=430)
MTGI-WV063 Stereo (n=13)
MTGI-WV073 Non-Stereo (n=426)
MTGI-WV073 Stereo (n=10)
MTGI-IR105 Non-Stereo (n=781)
MTGI-IR105 Stereo (n=7)

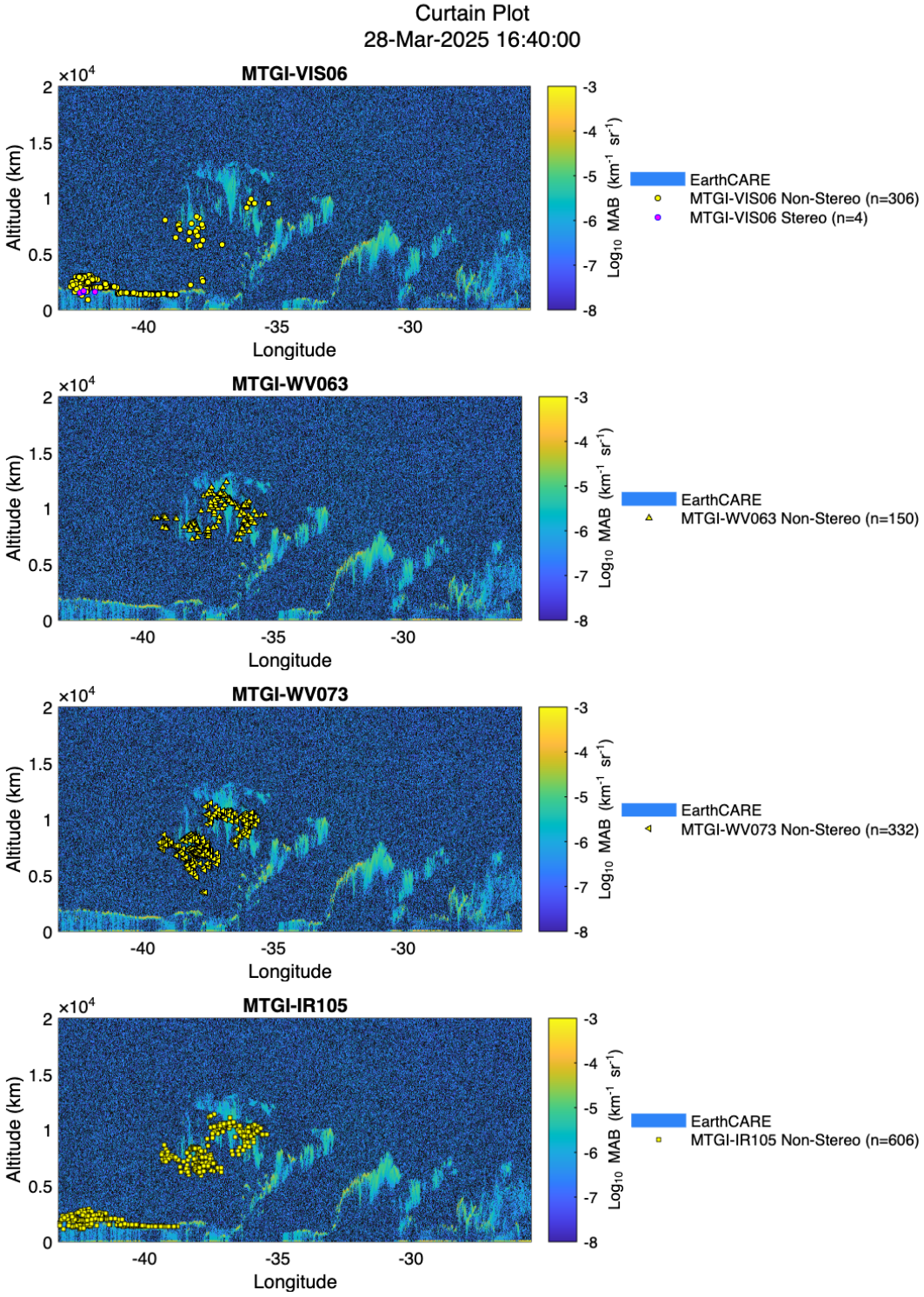

Curtain Plot
28-Mar-2025 15:10:00
MTGI-VIS06
×10^4
2
1.5
1
0.5
0
Altitude (km)
-20
-18
-16
-14
-12
-10
-8
-6
-4
Longitude
-3
-4
-5
-6
-7
-8
Log10 MAB (km-1 sr-1)
EarthCARE
MTGI-VIS06 Stereo (n=2)

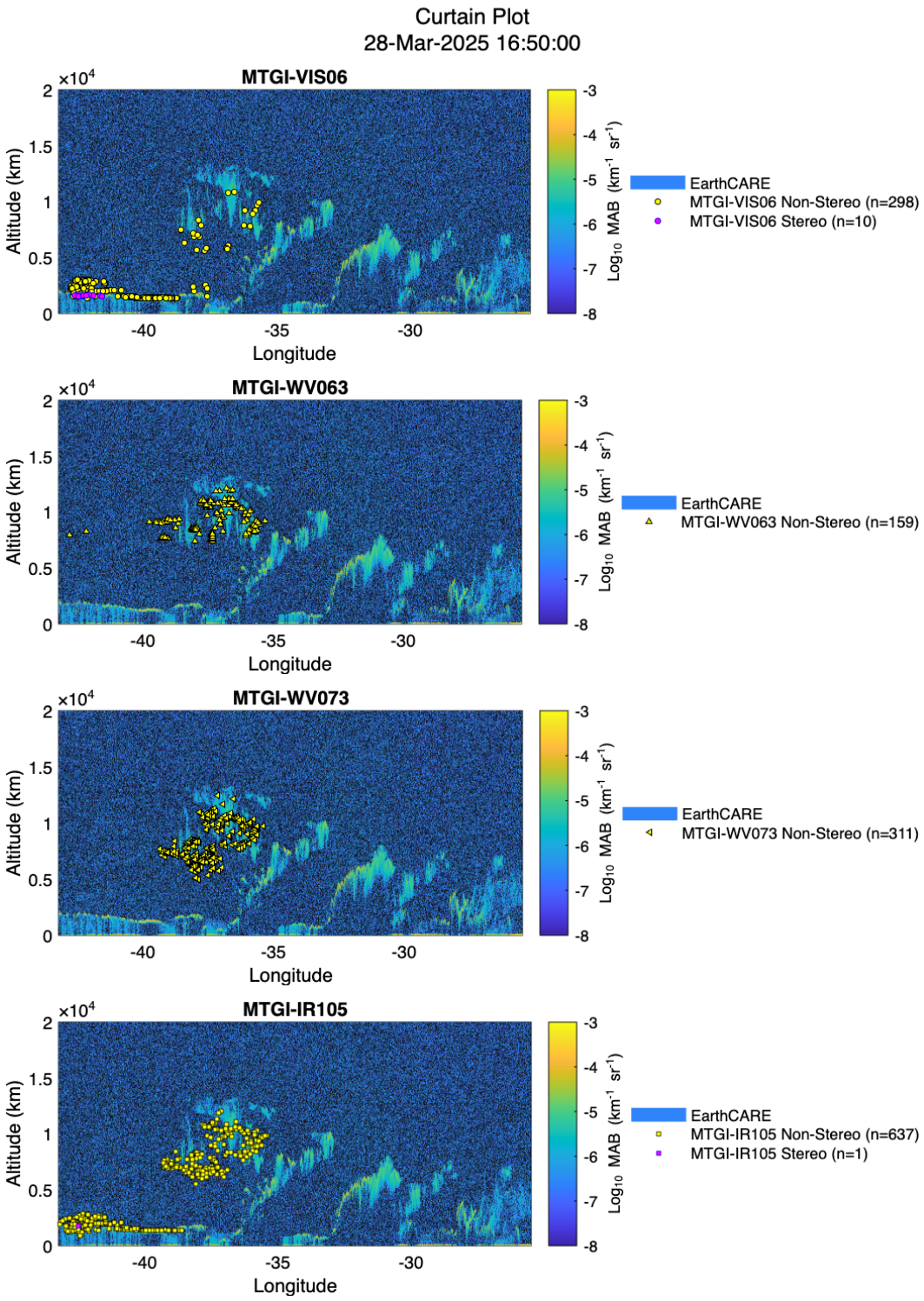

Curtain Plot
28-Mar-2025 15:20:00
MTGI-VIS06
×10^4
Altitude (km)
Longitude
Log10 MAB (km-1 sr-1)
EarthCARE
MTGI-VIS06 Non-Stereo (n=45)
MTGI-IR105
×10^4
Altitude (km)
Longitude
Log10 MAB (km-1 sr-1)
EarthCARE
MTGI-IR105 Non-Stereo (n=101)

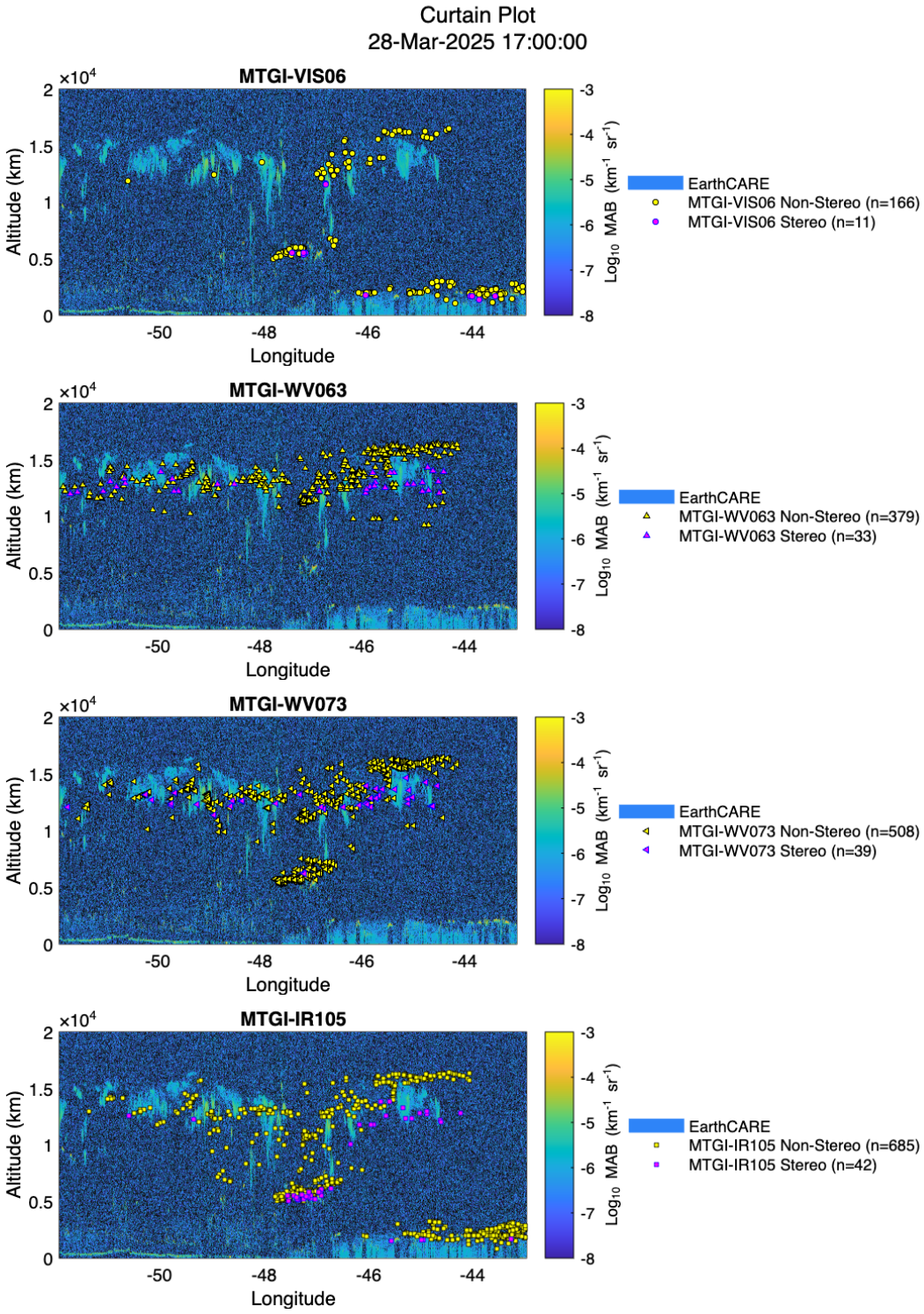

Curtain Plot
28-Mar-2025 15:30:00
MTGI-VIS06
MTGI-WV063
MTGI-WV073
MTGI-IR105
×10^4
Altitude (km)
Longitude
Log10 MAB (km-1 sr-1)
EarthCARE
MTGI-VIS06 Non-Stereo (n=322)
MTGI-VIS06 Stereo (n=39)
MTGI-WV063 Non-Stereo (n=483)
MTGI-WV063 Stereo (n=73)
MTGI-WV073 Non-Stereo (n=714)
MTGI-WV073 Stereo (n=103)
MTGI-IR105 Non-Stereo (n=1169)
MTGI-IR105 Stereo (n=195)

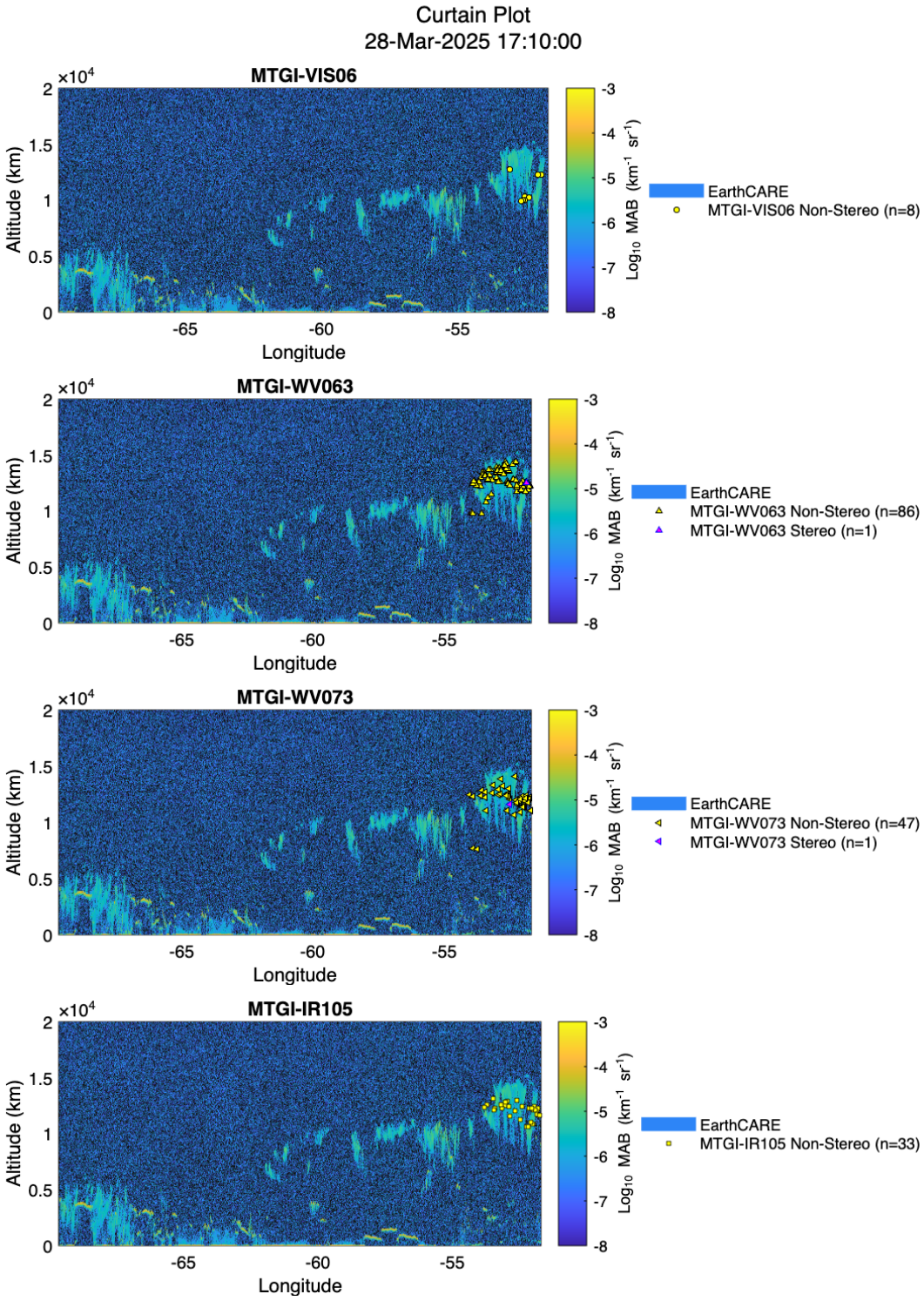

Curtain Plot
28-Mar-2025 15:40:00
MTGI-VIS06
MTGI-WV063
MTGI-WV073
MTGI-IR105
Altitude (km)
Longitude
Log10 MAB (km-1 sr-1)
EarthCARE
MTGI-VIS06 Non-Stereo (n=255)
MTGI-VIS06 Stereo (n=10)
MTGI-WV063 Non-Stereo (n=362)
MTGI-WV063 Stereo (n=73)
MTGI-WV073 Non-Stereo (n=753)
MTGI-WV073 Stereo (n=46)
MTGI-IR105 Non-Stereo (n=756)
MTGI-IR105 Stereo (n=34)

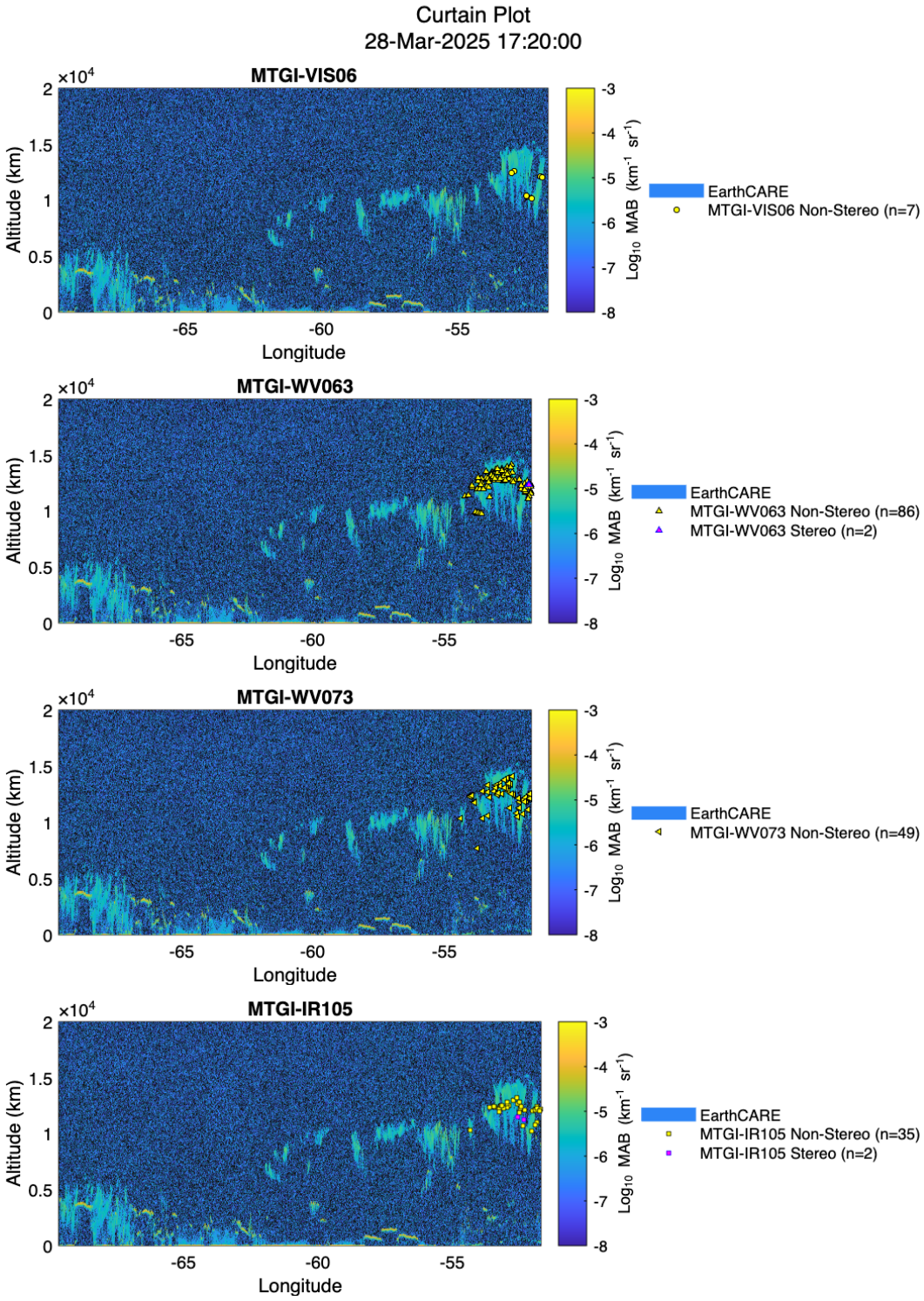

Curtain Plot
28-Mar-2025 15:50:00
MTGI-VIS06
MTGI-WV063
MTGI-WV073
MTGI-IR105
×10^4
Altitude (km)
Longitude
Log10 MAB (km-1 sr-1)
EarthCARE
MTGI-VIS06 Stereo (n=10)
MTGI-WV063 Stereo (n=73)
MTGI-WV073 Stereo (n=40)
MTGI-IR105 Stereo (n=30)


Curtain Plot
28-Mar-2025 16:40:00
MTGI-VIS06
MTGI-WV063
MTGI-WV073
MTGI-IR105
×10^4
Altitude (km)
Longitude
Log10 MAB (km-1 sr-1)
EarthCARE
MTGI-VIS06 Non-Stereo (n=306)
MTGI-VIS06 Stereo (n=4)
MTGI-WV063 Non-Stereo (n=150)
MTGI-WV073 Non-Stereo (n=332)
MTGI-IR105 Non-Stereo (n=606)


Curtain Plot
28-Mar-2025 16:50:00
MTGI-VIS06
MTGI-WV063
MTGI-WV073
MTGI-IR105
×10^4
Altitude (km)
Longitude
Log10 MAB (km-1 sr-1)
EarthCARE
MTGI-VIS06 Non-Stereo (n=298)
MTGI-VIS06 Stereo (n=10)
MTGI-WV063 Non-Stereo (n=159)
MTGI-WV073 Non-Stereo (n=311)
MTGI-IR105 Non-Stereo (n=637)
MTGI-IR105 Stereo (n=1)


Curtain Plot
28-Mar-2025 17:00:00
MTGI-VIS06
MTGI-WV063
MTGI-WV073
MTGI-IR105
×10^4
Altitude (km)
Longitude
Log10 MAB (km-1 sr-1)
EarthCARE
MTGI-VIS06 Non-Stereo (n=166)
MTGI-VIS06 Stereo (n=11)
MTGI-WV063 Non-Stereo (n=379)
MTGI-WV063 Stereo (n=33)
MTGI-WV073 Non-Stereo (n=508)
MTGI-WV073 Stereo (n=39)
MTGI-IR105 Non-Stereo (n=685)
MTGI-IR105 Stereo (n=42)


Curtain Plot
28-Mar-2025 17:10:00
MTGI-VIS06
MTGI-WV063
MTGI-WV073
MTGI-IR105
×10^4
Altitude (km)
Longitude
Log10 MAB (km-1 sr-1)
EarthCARE
MTGI-VIS06 Non-Stereo (n=8)
MTGI-WV063 Non-Stereo (n=86)
MTGI-WV063 Stereo (n=1)
MTGI-WV073 Non-Stereo (n=47)
MTGI-WV073 Stereo (n=1)
MTGI-IR105 Non-Stereo (n=33)


Curtain Plot
28-Mar-2025 17:20:00
MTGI-VIS06
MTGI-WV063
MTGI-WV073
MTGI-IR105
×10^4
Altitude (km)
Longitude
Log10 MAB (km-1 sr-1)
EarthCARE
MTGI-VIS06 Non-Stereo (n=7)
MTGI-WV063 Non-Stereo (n=86)
MTGI-WV063 Stereo (n=2)
MTGI-WV073 Non-Stereo (n=49)
MTGI-IR105 Non-Stereo (n=35)
MTGI-IR105 Stereo (n=2)

APPENDIX C – ERA5 OBSERVATIONS VERSUS ANALYSIS

Validation of HRW winds using ERA5 was performed for the following seven days selected two weeks apart from Winter-Spring 2025:
January 01, 17 and 31, February 14 and 28, and March 14 and 28.

The process used for comparing the HRW winds to those of ERA5 is described in this section.

1. Time-matching (simultaneity check)

For each of the seven dates selected for comparison, we examined the available HRW winds and ERA5 winds over a nominal 24-hour period.
For each hour, we determined whether the HRW observation time and the ERA5 time differed by no more than 10 minutes.
Hours exceeding this tolerance were flagged as non-compliant and excluded from all subsequent analysis.

2. Spatial colocation mask between stereo and non-stereo winds

In our preliminary analyses, we observed that the non-stereo retrievals produced substantially more wind vectors than the stereo method, and a large fraction of these non-stereo vectors had no nearby stereo counterpart. To enable a more rigorous and spatially consistent comparison between the two methods, we restricted the non-stereo dataset to only those vectors that are located within a 4-km radius of the stereo samples. This was achieved by generating a spatial colocation mask for every hour that satisfied the simultaneity requirement described earlier.

- For each stereo wind vector, we searched for non-stereo wind samples located within a 4-km radius. Only non-stereo samples meeting this spatial criterion were retained; all others were excluded.
- The colocation mask was generated independently for every valid hour for all seven validation dates.
- The resulting masks ensure that the non-stereo dataset is more spatially aligned with the stereo dataset, enabling less biased comparisons against the ERA5 winds.

3. Comparison Method between HRW and ERA5 winds

To compare the HRW stereo and non-stereo winds with ERA5 we interpolate the ERA5 profile to the location and pressure level of each observed wind vector. Only hours that have a simultaneous HRW dataset are processed. The same method is applied for stereo and non-stereo wind vectors.

Wind vectors from the visible band VIS06 and the IR band IR105 are processed independently. In addition, the following filters were applied before performing the comparison:

- Only sites where the Earth Central Angle (ECA) with respect to both satellites is less than 60 degrees are used.
- Still winds where the velocity of the wind components is less than 2 m/s are excluded.
- Three height intervals are defined, and each interval is processed independently:
    - Low level winds where the height is less than 2 km
    - Mid-level winds where the height is between 2 and 6 km
    - High level winds where the height is larger than 6 km
- For each hour of each of the selected seven validation dates we apply the filtering described above, and then we compute:
    - The mean bias in the U and V wind components between HRW and ERA5
    - The standard deviation (STDV) of the bias
    - The number of samples contributing to the computed statistics

These metrics were aggregated across all validation dates to evaluate differences in performance between the stereo and non-stereo wind retrieval methods.

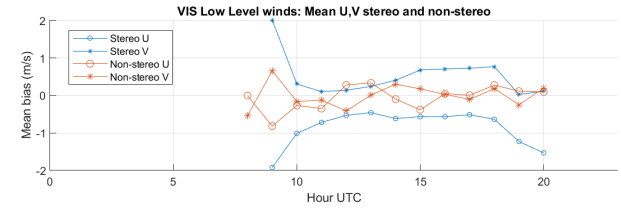
4. Validation Results

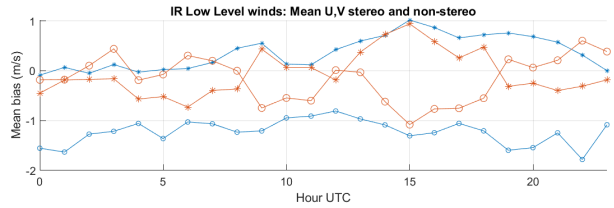
The results of the comparison between HRW and ERA5 wind vectors are summarized in the plots shown in Sections C1 to C3 of this appendix. Each figure shows the comparison for both VIS and IR for a single date. There are three sets of seven figures to reflect the selected height intervals.

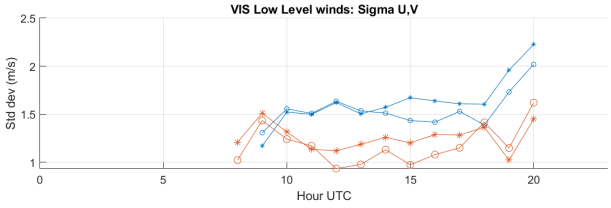
We observed that stereo winds generally match ERA5 winds at high levels and non-stereo winds show a better match with ERA5 at mid- and low-level winds.

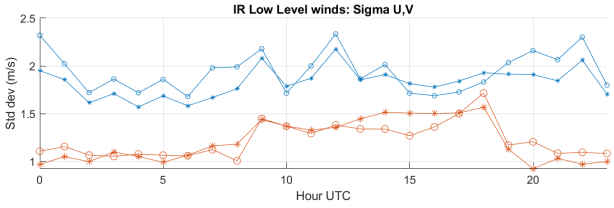
C.1 Results for Low Level Winds (height < 2km)

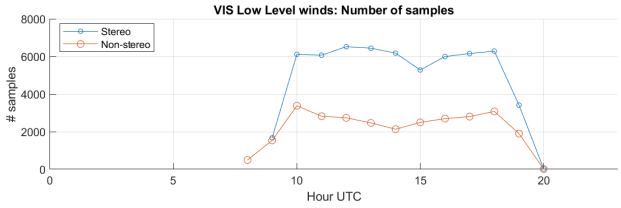
Day summary for Low Level Winds: VIS (left) vs IR (right), 20250103

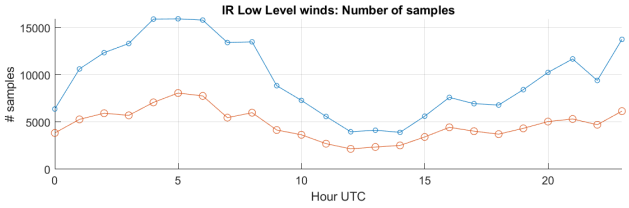




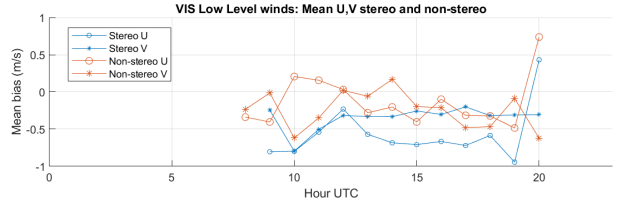


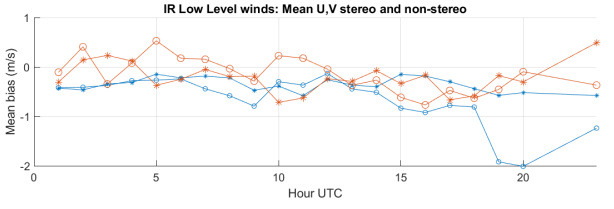


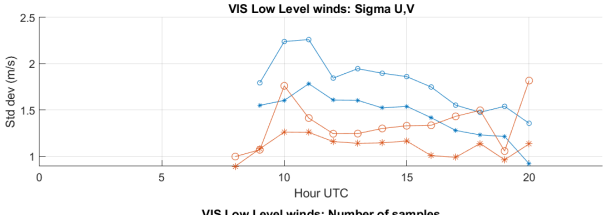


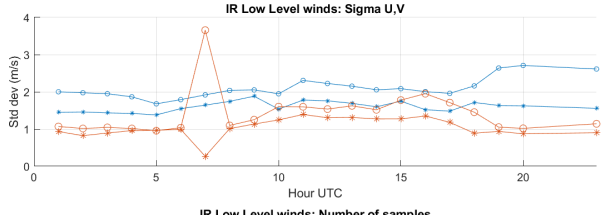


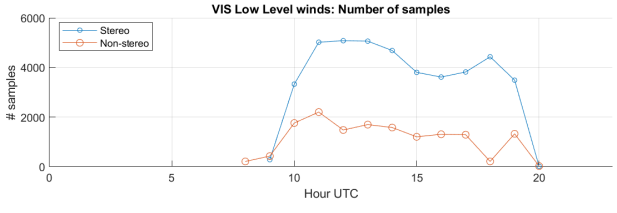
Day summary for Low Level Winds: VIS (left) vs IR (right), 20250117

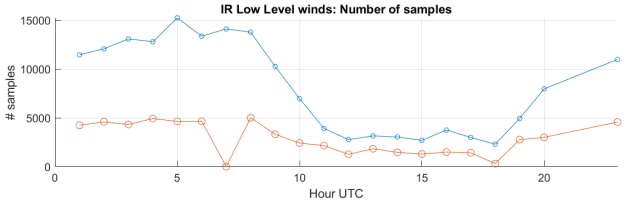




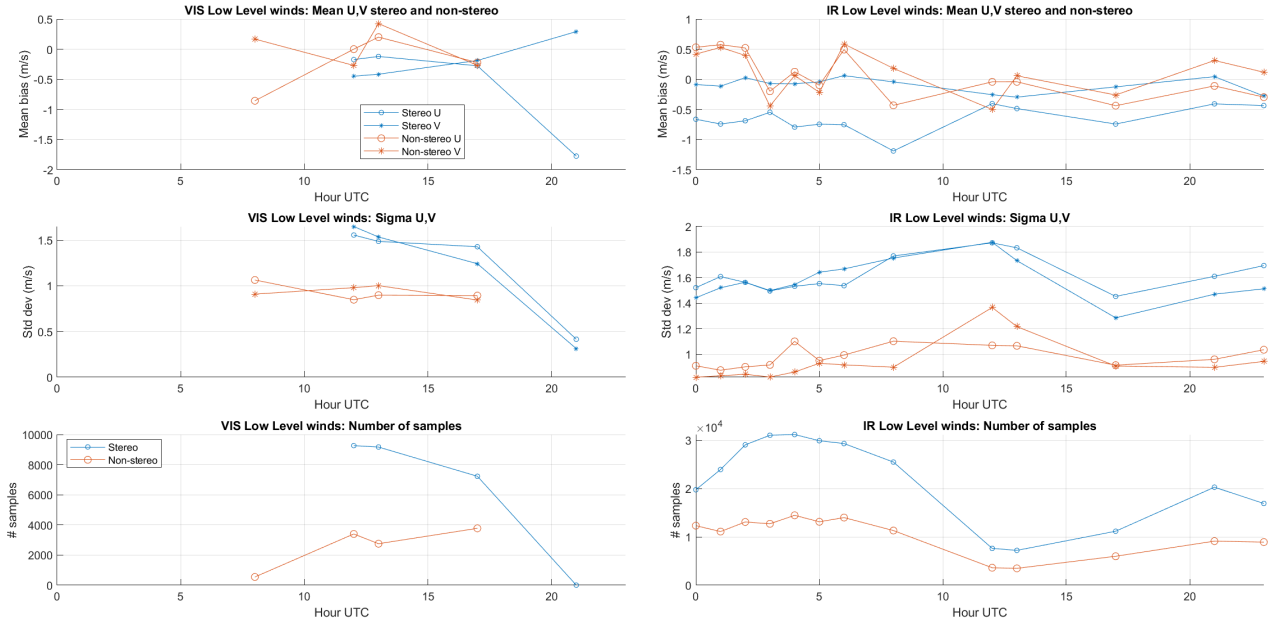




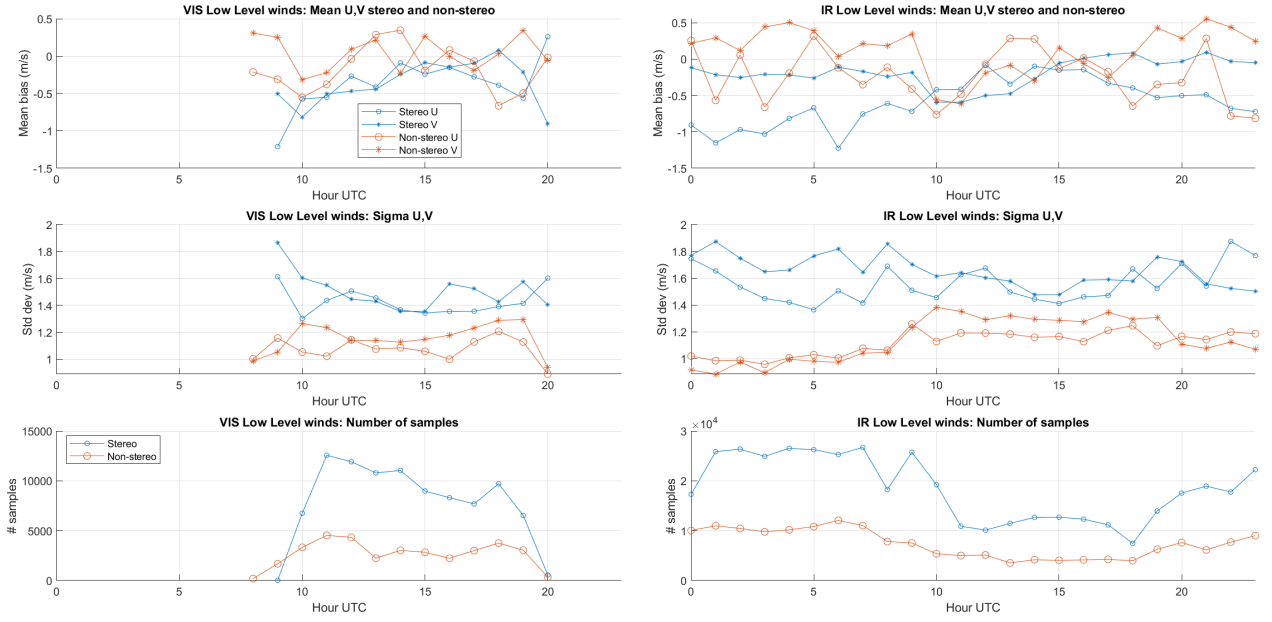




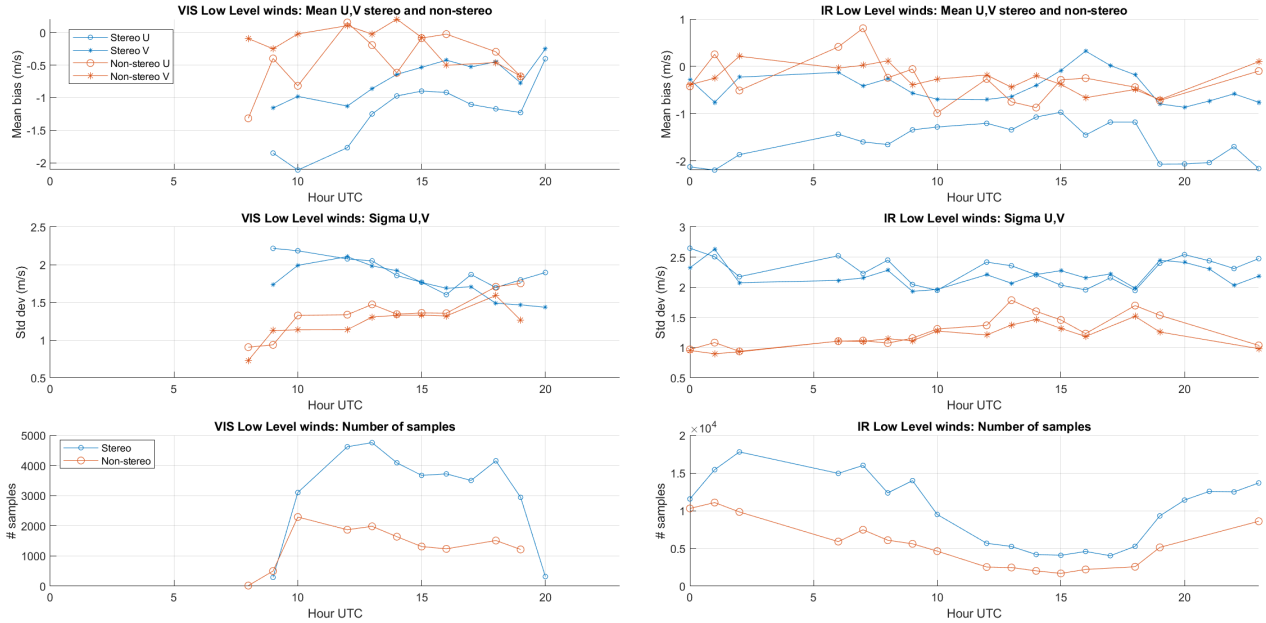
Day summary for Low Level Winds: VIS (left) vs IR (right), 20250131



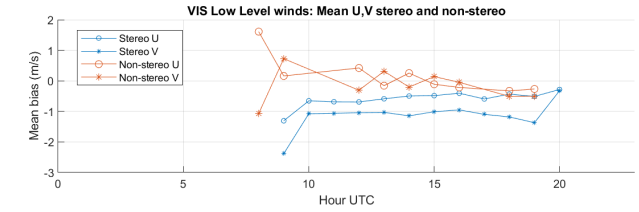
Day summary for Low Level Winds: VIS (left) vs IR (right), 20250214

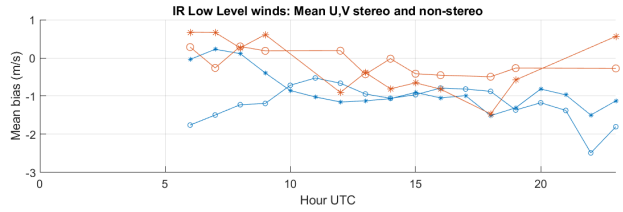


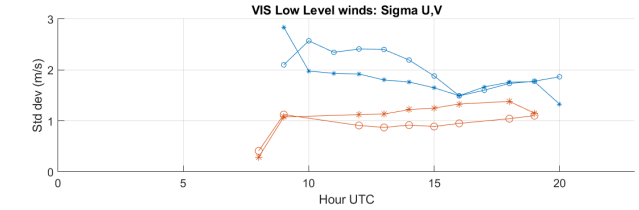
Day summary for Low Level Winds: VIS (left) vs IR (right), 20250228

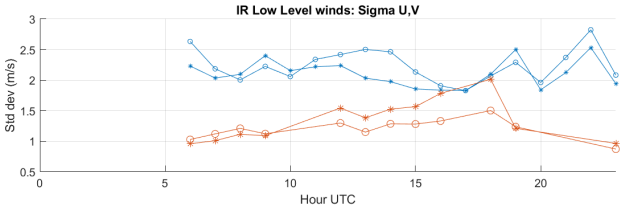


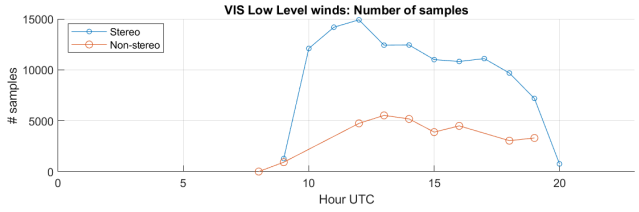
Day summary for Low Level Winds: VIS (left) vs IR (right), 20250314

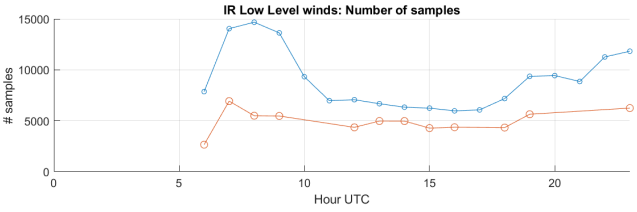




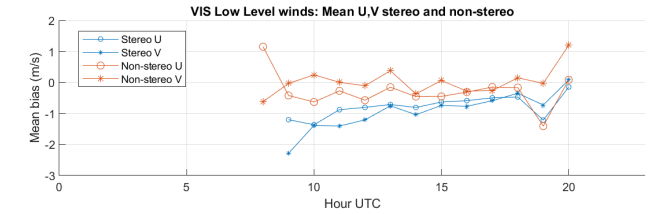


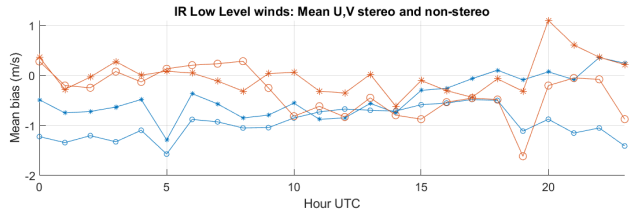


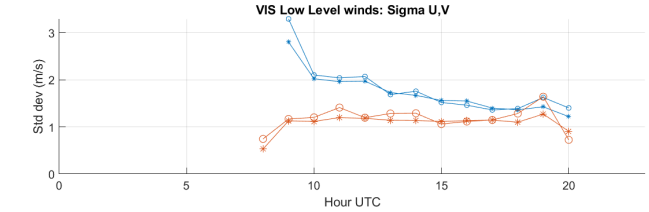


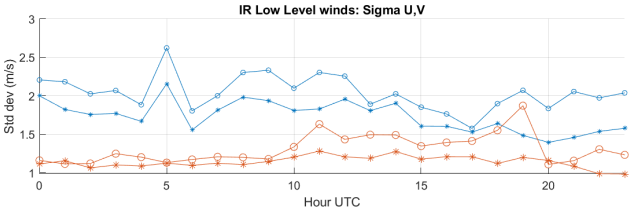


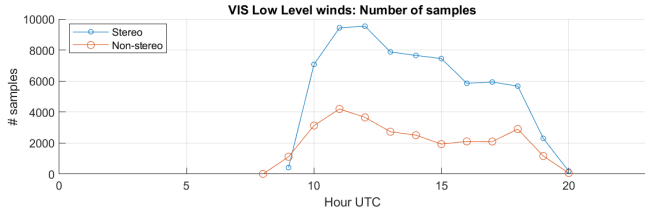
Day summary for Low Level Winds: VIS (left) vs IR (right), 20250328

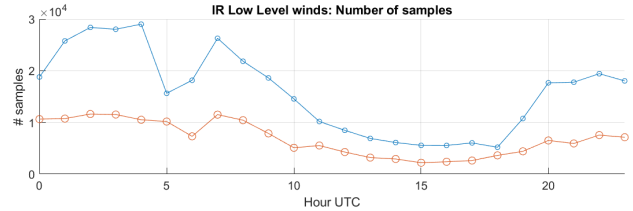




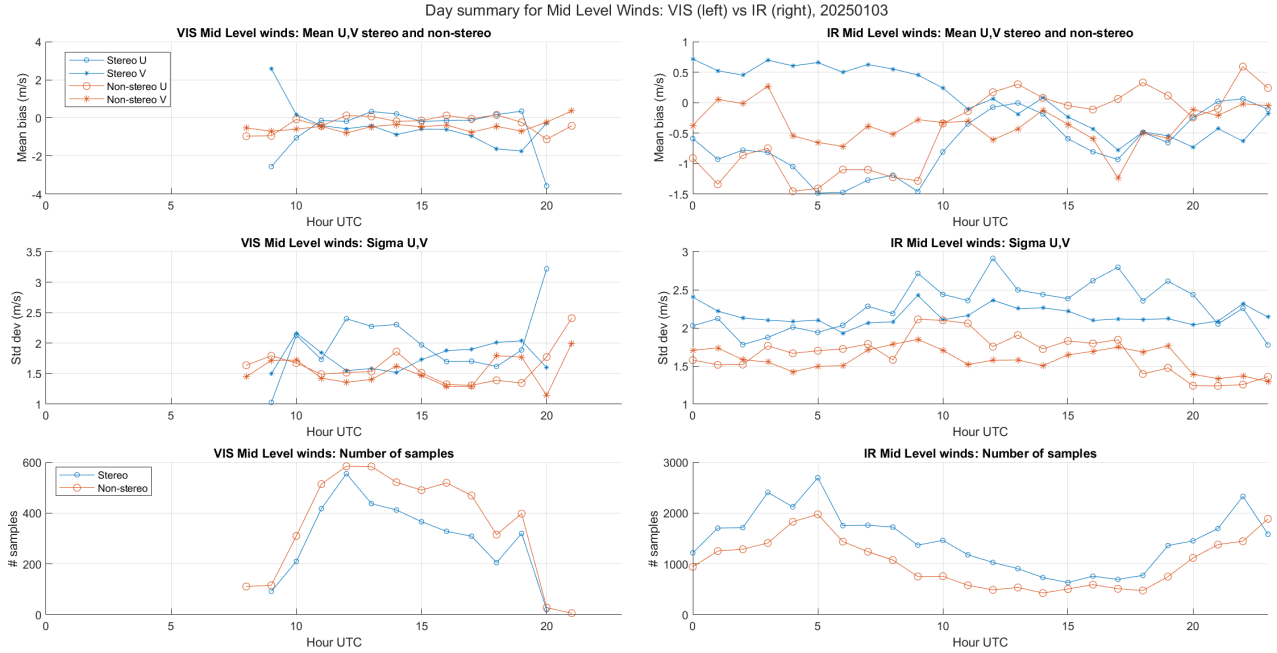


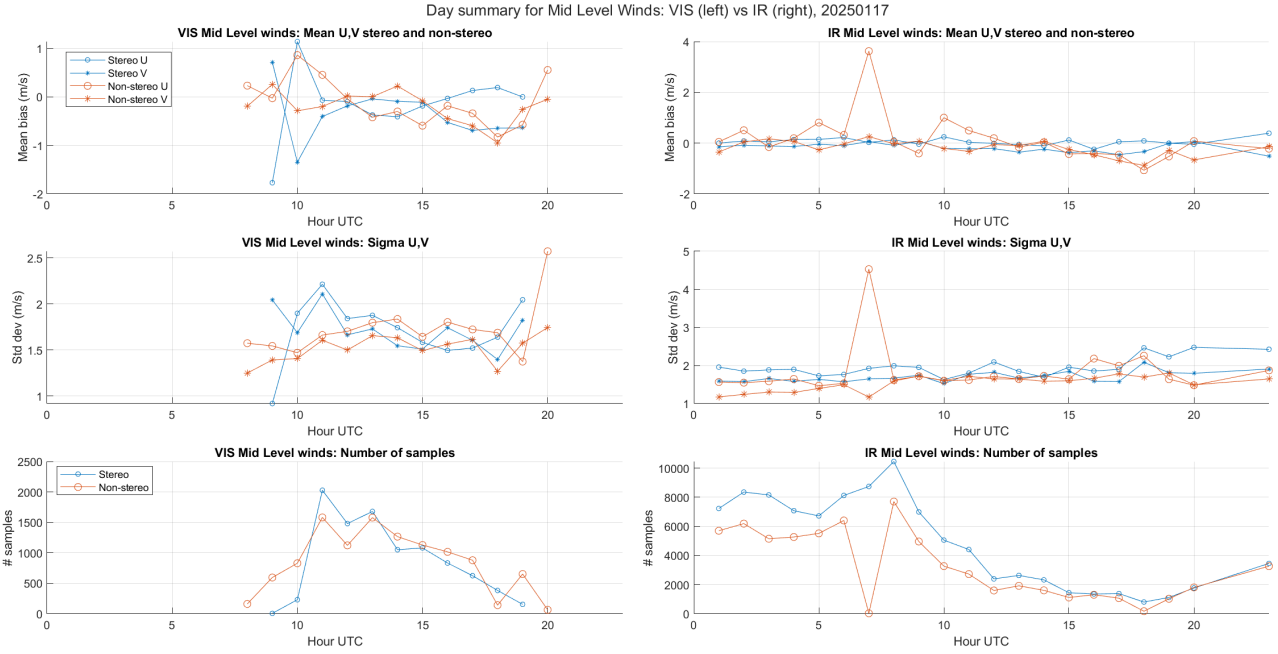




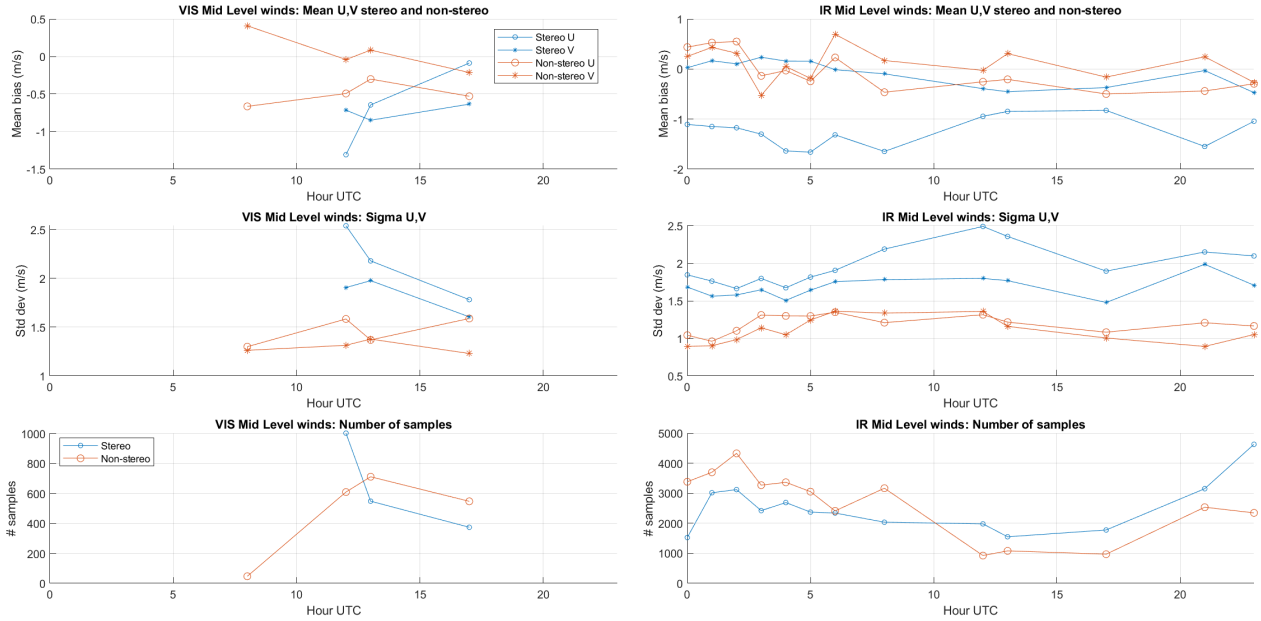


C.2 Results for Mid Level Winds (height 2-6km)

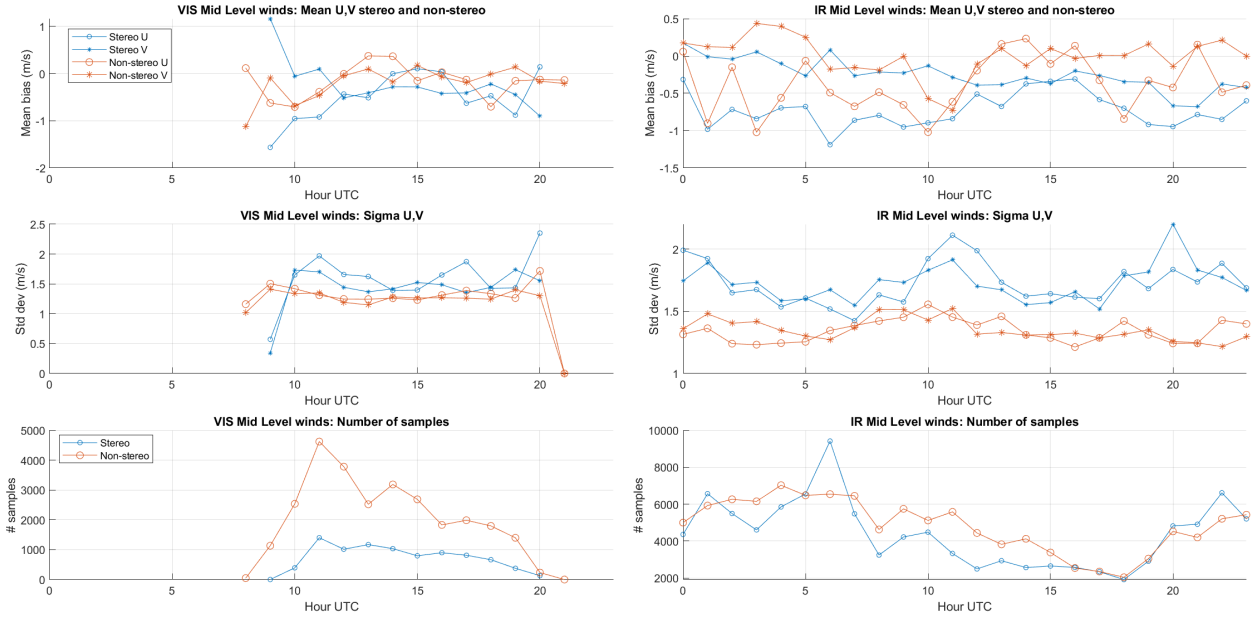




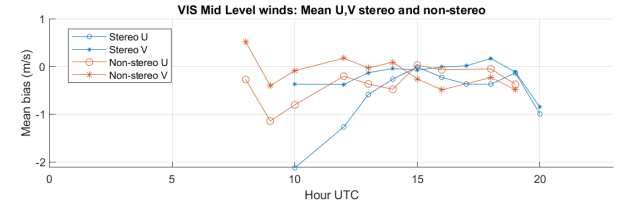
Day summary for Mid Level Winds: VIS (left) vs IR (right), 20250131

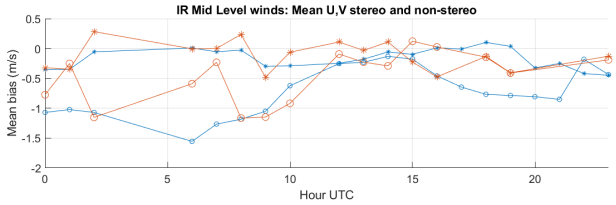


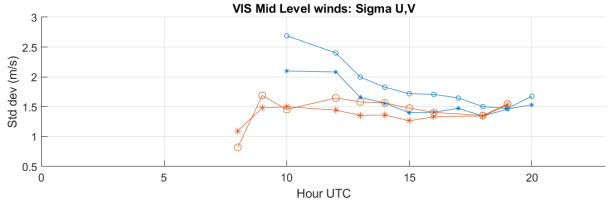
Day summary for Mid Level Winds: VIS (left) vs IR (right), 20250214

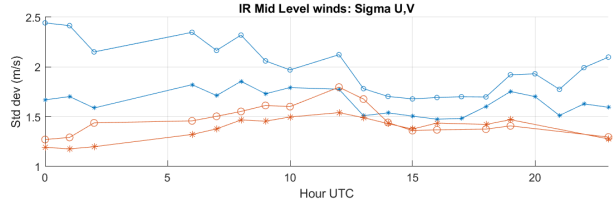


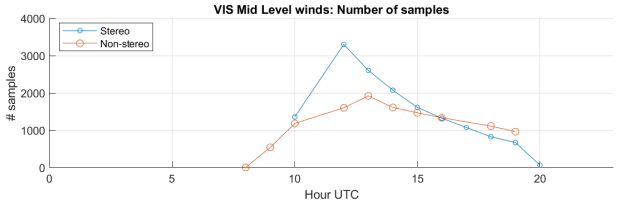
Day summary for Mid Level Winds: VIS (left) vs IR (right), 20250228

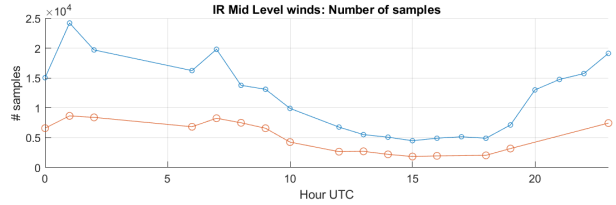




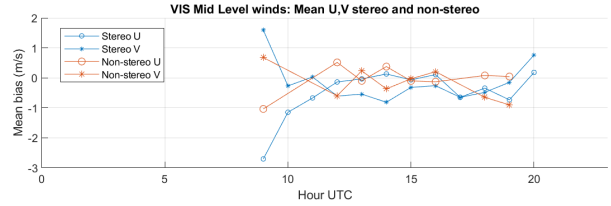


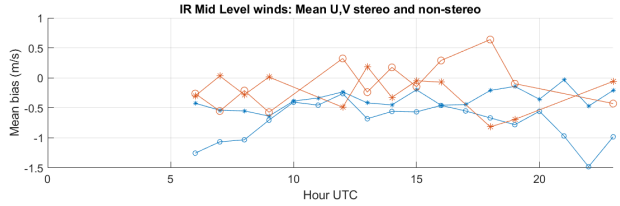


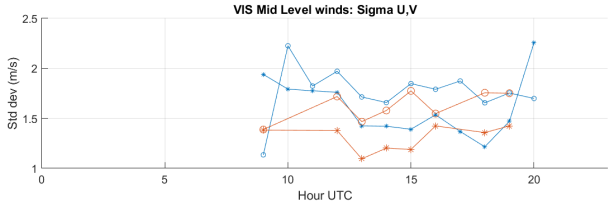


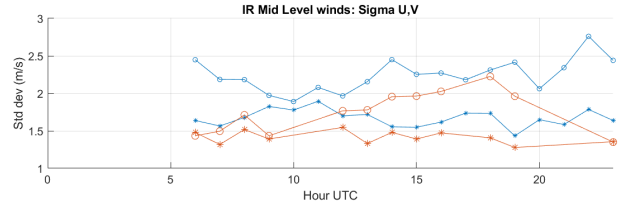


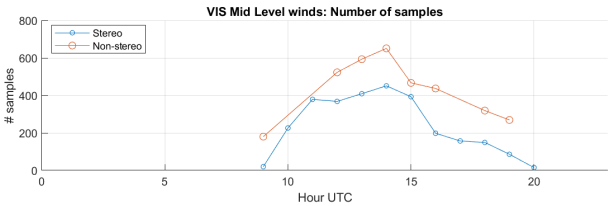
Day summary for Mid Level Winds: VIS (left) vs IR (right), 20250314

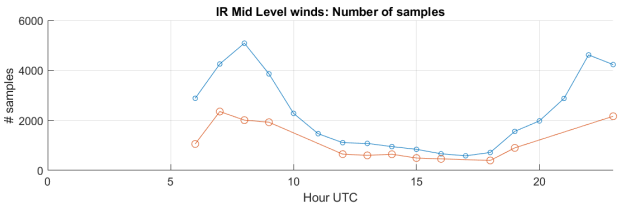




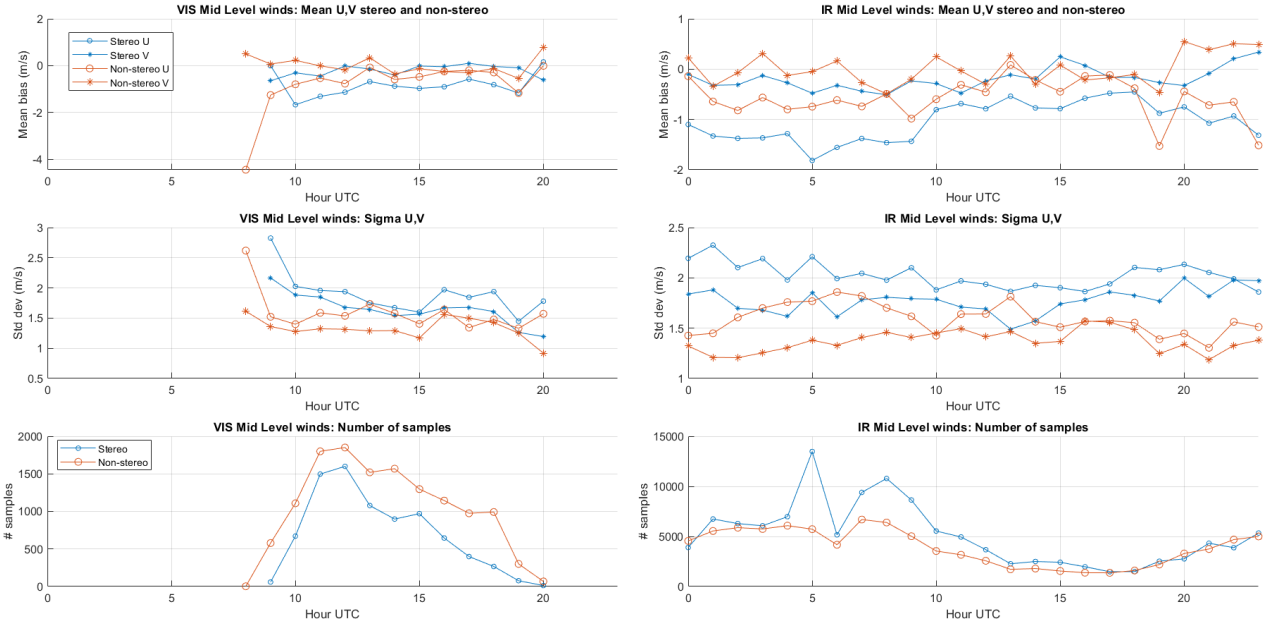






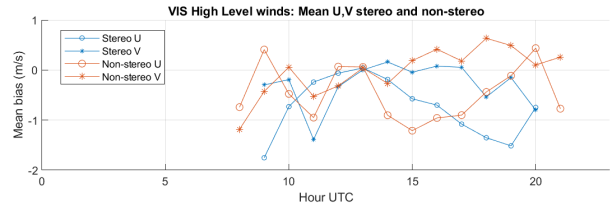


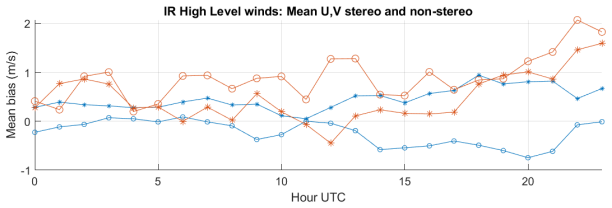
Day summary for Mid Level Winds: VIS (left) vs IR (right), 20250328

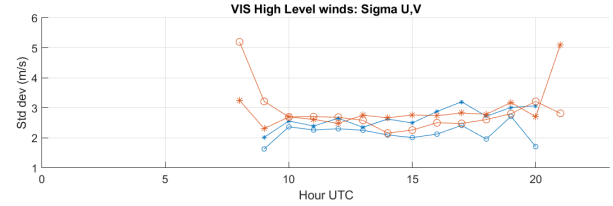


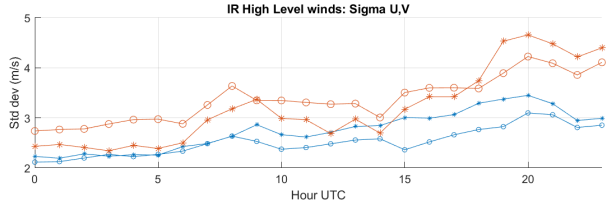
C.3 Results for High Level Winds (height > 6km)

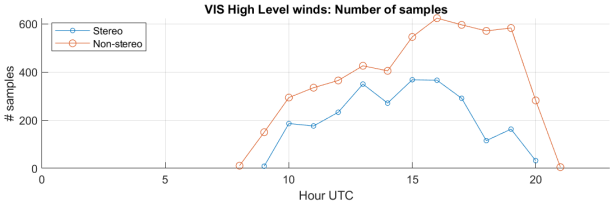
Day summary for High Level Winds: VIS (left) vs IR (right), 20250103

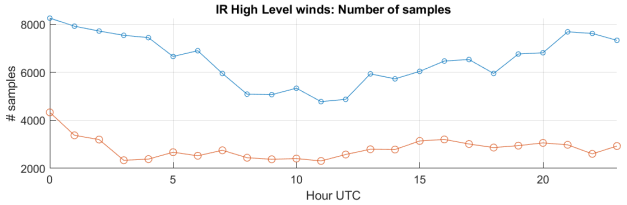




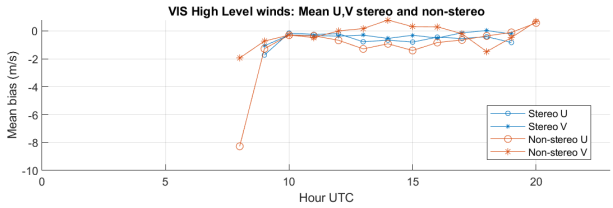


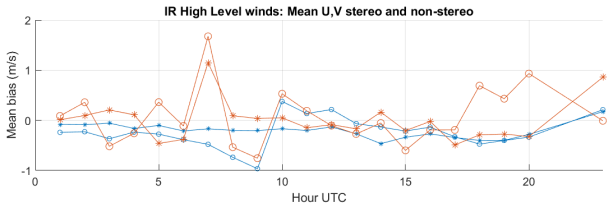


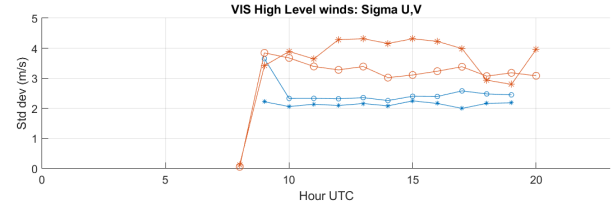


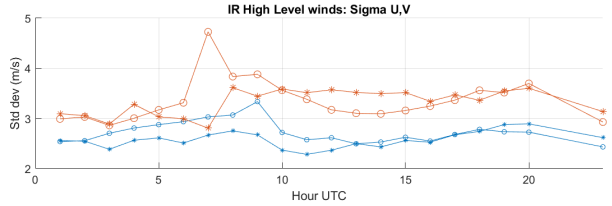


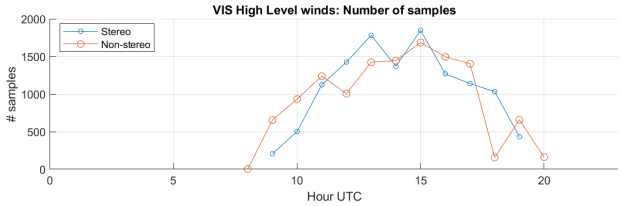
Day summary for High Level Winds: VIS (left) vs IR (right), 20250117

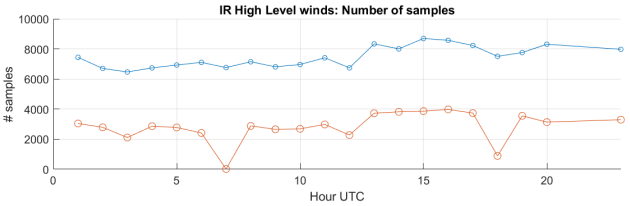




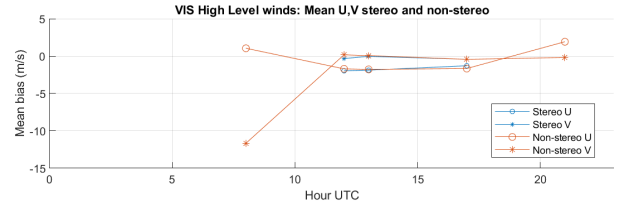


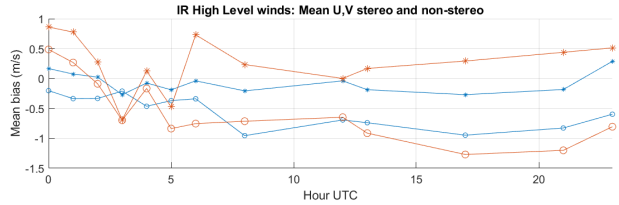


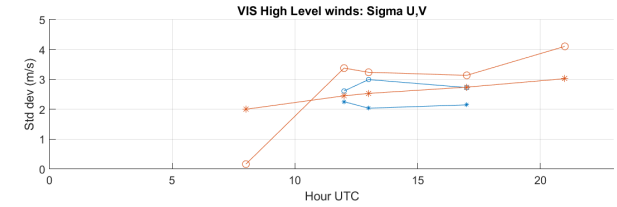


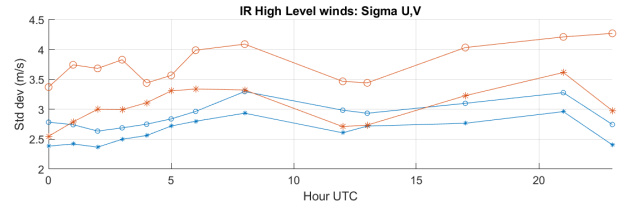


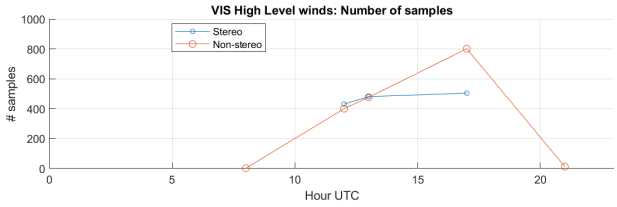
Day summary for High Level Winds: VIS (left) vs IR (right), 20250131

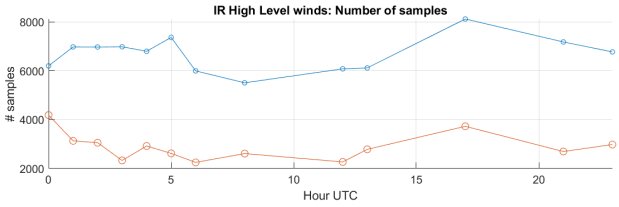




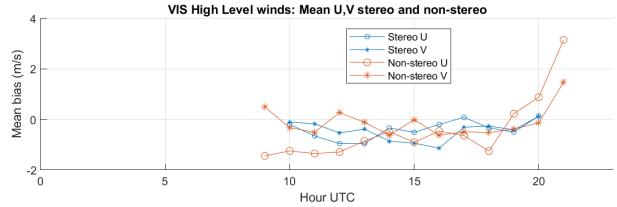


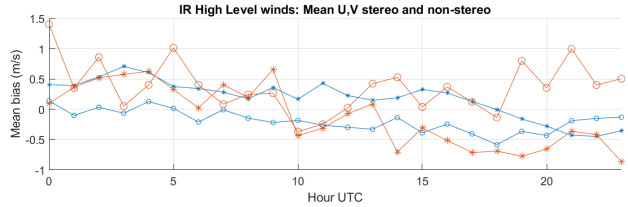


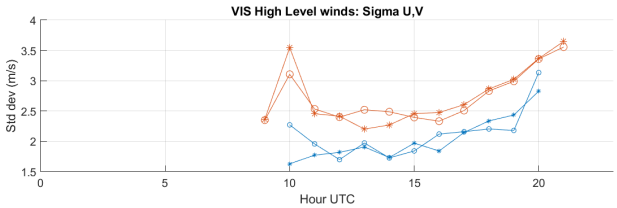


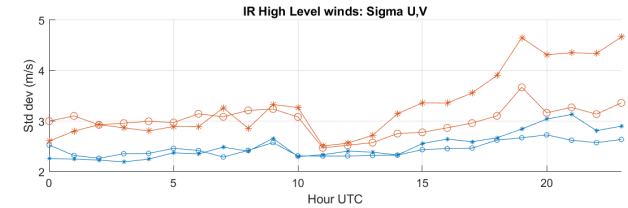


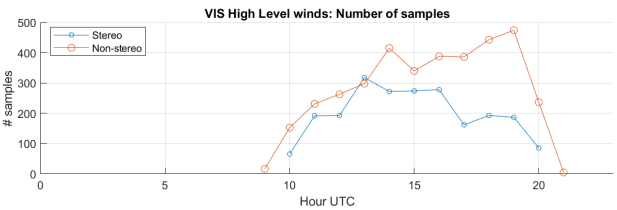
Day summary for High Level Winds: VIS (left) vs IR (right), 20250214

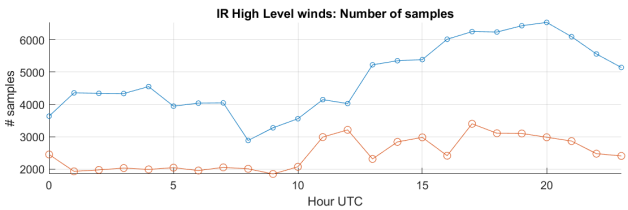




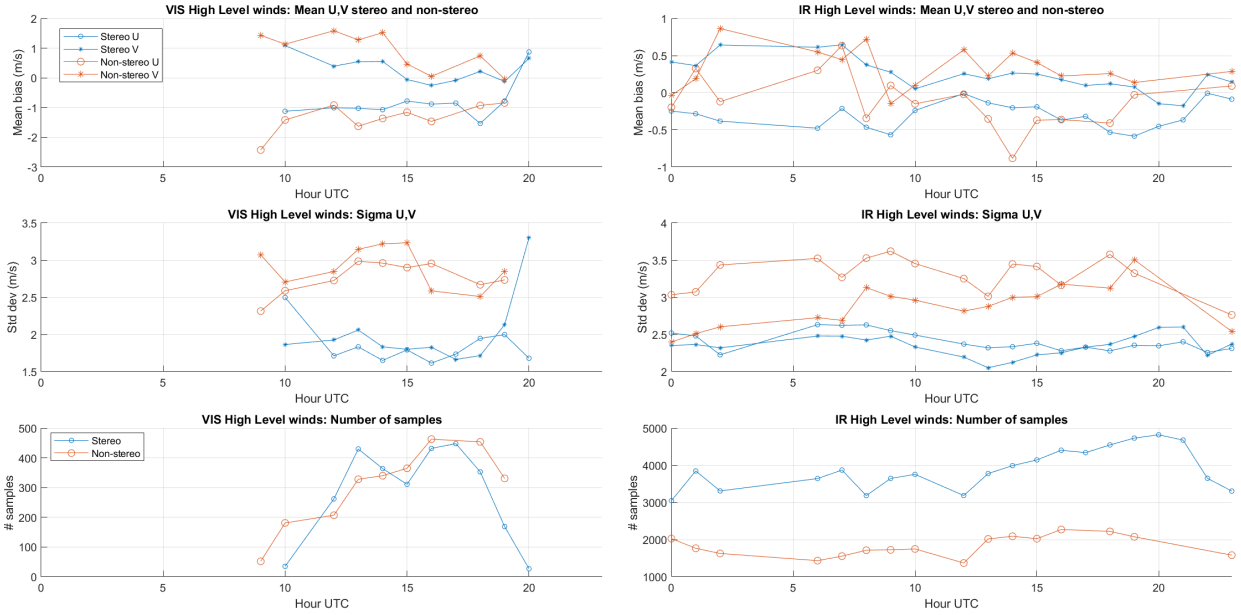




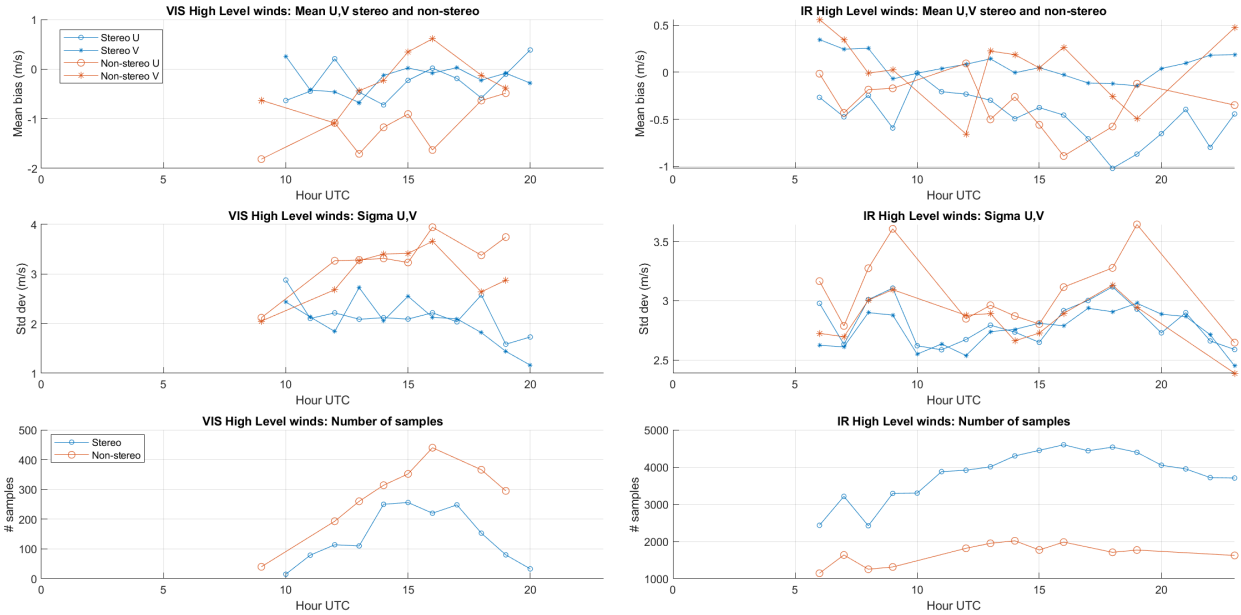




Day summary for High Level Winds: VIS (left) vs IR (right), 20250228



Day summary for High Level Winds: VIS (left) vs IR (right), 20250314



Day summary for High Level Winds: VIS (left) vs IR (right), 20250328

